

Large-eddy simulations of oceanic convective shear flow

Dissertation
zur Erlangung des Doktorgrades
der Naturwissenschaften im Fachbereich
Geowissenschaften
der Universität Hamburg

vorgelegt von
Stefan Heitmann
aus Ratzeburg

Hamburg
2003

Als Dissertation angenommen vom Fachbereich Geowissenschaften der
Universität Hamburg

auf Grund der Gutachten von Prof. Dr. Jan O. Backhaus

und Dr. Jochen Fröhlich

Hamburg, den _____

Professor/Professorin Dr. _____
(Sprecher/Sprecherin des Fachbereichs Geowissenschaften)

Abstract

The structure of the instantaneous flow fields and turbulence statistics in oceanic convection affected by wind-induced shear are analysed using a large-eddy simulation (LES) data set. LES is a method in which the large energy-containing eddies are represented on the numerical grid while the smaller more universal eddies have to be modeled by a subgrid-scale (SGS) model.

Three distinct convective flows driven by surface cooling are generated. One is the convectively mixed layer with negligible surface shear corresponding to calm wind conditions. The other two are convectively mixed layers affected by enlarged wind-generated shear stresses. The heat flux was held constant in order to provide equal thermal forcing. Instantaneous flow fields reveal the ability of the mean shear to order temperature fluctuations into convective roll-like structures rather than the well-known cells from Rayleigh-Bénard convection.

A modified SGS model has been developed in order to overcome known deficiencies of the Smagorinsky SGS model in near-wall flows. The SGS model has been formulated as a second-order moment approach. In the present formulation this corresponds to a non-linear SGS eddy viscosity formulation. It is shown that some of recently proposed modifications of Smagorinsky SGS modeling can be recovered from the present approach as special cases.

A new formulation of atmosphere-ocean boundary conditions is proposed which avoids the restrictive assumptions inherent in Monin-Obukhov similarity theory.

In free convection the well-known non-local effects due to turbulent and pressure transport of turbulent kinetic energy from the surface to the bulk of the convectively mixed layer are confirmed. The sheared convective flows under consideration show hybrid characteristics. In the near-surface region, they exhibit typical shear flow characteristics, since shear is by far the dominant mechanism. In the bulk of the mixed layer the flows exhibit typical bouyant flow characteristics.

The unstable stratification significantly lowers the Ekman volume transport compared to near-neutral stratified flows. In comparison to neutral steady-state conditions, the Ekman volume transport is lowered by one order of magnitude. Accordingly, the Ekman volume transport is no longer perpendicular to the surface stress but decreases to about one half of its near-neutral value.

Mixed layer bulk modeling was used to set up the numerical grid. The analytical solution for the mixed layer growing into a quiescent stably stratified layer beneath derived by Zilitinkevich is shown to be a good estimation. Extensions to more complex situations are considered.

Contents

1	Introduction	3
2	Geophysical boundary layers	10
2.1	Ekman layer theory	10
2.1.1	The stratified Ekman layer	11
2.2	Numerical and observational studies	13
2.3	Difference between atmospheric and oceanic boundary layers . . .	15
3	Large Eddy Simulation	17
3.1	The filter operation	18
3.2	Introduction to SGS modeling	20
3.2.1	The Smagorinsky model and its shortcomings	20
3.2.2	Modified Smagorinsky SGS models	22
3.3	Second-order algebraic SGS model	25
3.3.1	Second-order closure in SGS modeling	25
3.3.2	The Third-Order Moments	27
3.3.3	Near-'wall' turbulence	30
3.3.4	Algebraisation of the second-order moment equations . . .	34
3.3.5	Recovering of simpler SGS models	36
3.4	The model equations	38
4	Implementation	39
4.1	Initial Conditions	39
4.2	Boundary Conditions	40
4.3	Numerical Algorithms	43
4.4	The SGS model algorithm	47
4.4.1	Storage procedure	47
4.4.2	Iterative computation	49
4.4.3	Numerical considerations of the SGS model	51
5	Bulk modeling of penetrative convection	54
5.1	Introduction	54
5.2	The zero order jump model	55

5.3	The entrainment law	57
5.4	Recovering of the empirical entrainment law	59
5.5	Analytical Solutions for Free Convection	60
6	The LES experiments	61
7	Results	64
7.1	Mean flow profiles	64
7.2	Instantaneous flow structures	70
7.3	Mean variances and fluxes	82
7.4	Velocity Scales	93
7.5	Turbulent kinetic energy	97
7.6	SGS contributions	100
7.6.1	Comparison with the original formulation	100
7.6.2	Numerical and physical diffusion	106
8	Summary and Outlook	112
A	Rotational effect on dissipation	116
B	Second-order moments in Cartesian form	117
C	TVD Advection Schemes	119
D	List of symbols	121
E	Bibliography	125

Chapter 1

Introduction

The interest in the process of oceanic convection has raised in the last decades due to its role in deep water formation in the world ocean. Deep water formation has been identified as significant part of the global oceanic thermohaline circulation (Broecker 1991, Rudels and Quadfasel 1991). As commonly a strong pycnocline separates the upper water masses from the deep ocean deep-reaching convection is regarded as important mechanism for the exchange of near-surface and deeper water masses. Deep water masses form by two distinct mechanisms. One is the descending of dense water along a continental slope which occurs in the shelf seas of the Arctic and the Antarctic. The second process is convection in the open ocean. Deep open ocean convection occasionally takes place in the Weddell Sea, the western Mediterranean, the Labrador and the Greenland Seas.

Vertical overturning of the water column in the convection regions is caused by strong buoyancy loss associated with the prevailing meteorological conditions in wintertime. In his conceptual model, Killworth (1976) describes three phases of convection: preconditioning, violent mixing and restratification. Preconditioning describes the doming of isopycnal surfaces by cyclonic circulation and moderate surface cooling. The violent mixing phase starts with the formation of small-scale convective plumes that can extend throughout the whole water column. The restratification phase starts after some days when baroclinic instabilities grow due to the horizontal gradient between the dense water in the interior and the less dense water in the surroundings. This results in a final spreading of the dense water and a gradual restratification of the convective region.

The volume of newly formed deep water depends crucially on the physical properties of the convective plumes. Conservation of mass requires that weak upward motion compensates the intense downward flow.

Regarding convecting layers which extend over most of the water column, the effect of Earth's rotation cannot be neglected and has been investigated in a number of field (Mertens 2000), laboratory (Maxworthy and Narimousa 1992) and numerical experiments (Mironov et al. 2000).

Rotational effects are not important for atmospheric convection, and for the ma-

jority of convective processes in the ocean as well since the associated timescale of these flows is short enough for rotational effects to be ignored. Such convection may therefore be called *shallow* convection in contrast to the *deep* convection that ventilates the deep ocean.

The Greenland Sea is typically covered by a cold and fresh surface layer (Aagaard and Carmack 1989). For deep convection to occur, the low-density surface layer has to be eroded locally. In the classical view of describing the preconditioning phase of deep convection it is assumed that a cyclonic gyre circulation creates an inclining of the isopycnals towards the surface (*doming*)(Marshall and Schott 1999) thus causing near-neutral stratification. There are however further mechanisms which may act as Preconditioning for subsequent deep convection to occur. Firstly, the ESOP-2 (*European Sub Polar Ocean Programme*) Project provided growing evidence that pre-existing mesoscale eddy fields rather than basin-wide gyre circulation may act as preconditioner (Jansen and Opheim 1999). A possible mechanism for the creation of mesoscale eddies in the Greenland Sea basin has been identified by Backhaus and Kämpf (1999). The author propose that parts of the East Greenland Current is deflected by the topography of the Jan Mayen Ridge and injected towards the central Greenland Sea. The fresh-water wedge on the top of the East Greenland Current will finally become dynamically unstable and decay into a number of mesoscale eddies or freshwater lenses. Additionally, it has been suggested that occasional removal of sea ice by prevailing winds is necessary for efficient erosion of the surface layer (Schott et al. 1993). The role of sea ice has been investigated in a number of numerical simulations coupling a convection model with a sea ice model (Kämpf and Backhaus 1998, Kämpf and Backhaus 1999).

The convective regions of the World Ocean are thought to be of extra importance in determing the air-sea exchange of carbon dioxide due to the extended vertical ventilation. The exchange is driven by both wind field and partial pressure difference between air and water. Little is known about the carbon fluxes in the surface layer of the Polar Ocean and its variability (Jansen and Opheim 1999). The submesoscale variability of carbon uptake for the area of the Greenland Sea gyre has been simulated by Wehde and Backhaus (1999). The authors coupled a simplified version of the present numerical model with a carbon-fluxes and a sea ice model. They report occasional outgasing of CO_2 even in winter.

Deardorff (1972) found that for shallow convective flows with negligible shear (*free* convection) the velocity and length scales of plumes are entirely determined by the surface buoyancy flux B_0 and the mixed layer depth D . From these scales the relevant velocity scale w_* can be found on dimensional arguments to be

$$w_* = (-B_0 \cdot D)^{1/3}. \quad (1.0.1)$$

Neglecting evaporation effects, the buoyancy flux is related to the dynamic heat flux \mathcal{H}_0 by

$$B_0 = -\frac{g\alpha}{c_P\varrho_0}\mathcal{H}_0, \quad (1.0.2)$$

where g is the Earth's gravity, α is the thermal expansion coefficient, c_P is the specific heat of water at constant pressure and ϱ_0 is a reference density.

Since the thermal expansion coefficient α strongly depends on water temperature and salinity its value in the Greenland Sea differs considerably from that in the Labrador Sea. Marshall and Schott (1999) take $\alpha_{GS} \approx 3 \cdot 10^{-5} K^{-1}$ as an average near-surface value in the Greenland Sea while $\alpha_{LS} \approx 9 \cdot 10^{-5} K^{-1}$ in the Labrador Sea. Consequently, at given heat flux the buoyancy flux in the Greenland Sea is weaker than in the Labrador Sea by a factor of three. This results in a velocity scale (1.0.1) which is smaller by a factor of $3^{1/3} \approx 1.4$. The relevance of w_* is that it expresses the intensity of plume-caused downward motion. It has been confirmed by field measurements that events of downward motion are of larger downward velocity in the Labrador Sea than in the Greenland Sea (Mertens 2000).

Rudels (1990) describes the formation of an unstable surface layer in the polar regions due to local freezing and/or brine rejection which penetrates into the water column when the instability becomes critical. However, as only molecular diffusion processes are taken into account he estimated the unstable layer depth to be on the order of 5 m.

It has been remarked by Backhaus (1995) that molecular processes are unlikely to dominate the convection process in the surface layer. Under unstable conditions, it is the interplay of winter cooling and wind mixing that operate to deepen the mixed layer¹ on the shelves of the marginal seas of the Arctic Ocean (Clarke et al. 1990). Locally confined shallow thermo-haline convection takes place mainly in *polynyas*, oceanic areas which remain at least partially ice free and are bordered by ice covered water. So-called latent-heat polynyas are created when the locally formed ice is continually removed by episodic cold wind events or currents. They form either in the vicinity of an ice edge or in the lee of islands (Smith et al. 1990). A sudden cold air outbreak will create enormous heat losses up to $1000 W m^{-2}$ (Backhaus, private communication) and may act as a trigger for convection. Polynyas contribute most to the production of dense shelf bottom water. During a cold air outbreak it is reasonable to assume that the ocean surface is in Ekman balance and any convective activity will be accompanied by the presence of wind-driven currents. The flow can be expected to be fully turbulent outside the viscous sublayer. For wall-bounded channel flow, the extension of the viscous sublayer is given by $z^+ \approx 40$ (Bradshaw 1976) where $z^+ = u_* z' / \nu_{mol}$ is the distance from the surface z' non-dimensionalized by the oceanic friction

¹Here and in the following 'mixed layer' always refers to the 'upper mixed layer'. Additionally, there exists the perennial thermocline in greater depths.

velocity u_* and the molecular viscosity ν_{mol} . Inserting moderate wind conditions ($u_* \sim 1\text{cm/s}$) this criterion corresponds to a distance $z' \sim \mathcal{O}(1\text{cm})$ at which the oceanic flow is fully turbulent. Hence, it is inappropriate to assume a laminar unstable layer of 5m extension. The presence of surface waves will even tend to increase turbulence intensity.

Instead of Rudels' laminar result Backhaus (1995) suggested to regard the Ekman layer as the appropriate (turbulent) length scale for the convectively unstable surface layer. The well-known Ekman layer results from the balance of Coriolis force and turbulent friction in neutrally stratified flows. Its extension D_{ek} scales with u_*/f_z . It is the upper bound for the influence of surface momentum flux on the flow field and the only relevant length scale in the neutrally stratified boundary layer.

The consequence of the Backhaus (1995) hypothesis is that convection in the marginal seas of the Arctic Ocean is influenced by wind mixing, i.e. the flow is in a state of *sheared* (or *forced*) convection rather than in a state of *free* convection. Due to its relatively weak buoyancy forcing this result may hold for shallow convection in the Greenland Sea as well (Backhaus, private commun.).

Free convective flows are characterised by the formation of hexagonale convective cells. In sheared convection the shear tends to organize the plumes in the mean shear direction. The main flow structure are roll-like vortices (Etling and Brown 1993) instead of cells.

The most important effect of mean shear is the modification of the heat transfer but there is considerably disagreement about its role. For example, Monin and Yaglom (1979) report that in a number of atmospheric field measurements the heat flux increases for increasing shear. This finding has been confirmed by numerical simulations (Hathaway and Sommerville 1986). In contrast, experiments by Ingersoll (1966) revealed lower heat flux with larger shear. Numerical simulations by Domaradzki and Metcalfe (1988) indicate that shear decreases the level of organization of the convective structures therefore decreasing the heat transfer.

The complex interaction between buoyancy-driven and shear effects has not yet been studied in detail in an oceanographic context. It is commonly argued that wind-induced shear only affects the upper $100 - 200\text{m}$ of the ocean whereas the interest of polar oceanographers has focussed on deep reaching convection (Marshall and Schott 1999).

In contrast, in the atmospheric boundary layer the interaction of buoyancy and wind manifests itself in cloud streets. These structures have been investigated in detail by theoretical (e.g. Asai 1970, Kuettner 1971, Brown 1972, Clever and Busse 1992), observational (e.g. LeMone 1973, Wilczak and Tillman 1980, Lenschow and Stephens 1986) and numerical studies. Numerical studies of the atmospheric boundary layer using large eddy simulation (LES) have been pioneered by Lilly (1967) and Deardorff (1970, 1972, 1974). LES is now an established technique for the investigation of turbulent flows. The physical basis for LES is the

separation of the flow into resolved and unresolved motion by applying a spatial filter. Whereas the large energy-containing eddies are represented on the computational grid, the smaller eddies are parameterised through a subgrid-scale (SGS) model which is commonly based on inertial subrange theory. LES studies of the convective atmospheric boundary layer in the presence of mean shear have been performed by e.g. Deardorff (1972), Sykes and Henn (1989), Moeng and Sullivan (1994) and Khanna and Brasseur (1998). However, simply adopting scaling laws from atmospheric convection to the ocean leads to unrealistic predictions as will be outlined in Chapter 2.

It is the aim of the present study to investigate the interaction of an unstable buoyancy flux with wind-driven shear in the oceanic boundary layer. It is exactly the situation met in high-latitude shelf seas subject to intense surface water cooling due to a cold-air outbreak. The outbreak is occasionally accompanied by intense freezing but the process of ice-formation is not considered in the present study. The analogy to atmospheric convective flows suggests that the large eddy formation in the form of roll vortices might be able to transfer momentum, heat, salinity and suspended matter deep into the water column. It might therefore be expected that the influence of wind reaches substantially deeper into the ocean than the Ekman layer. It is however not clear whether the transfer of properties depends on buoyant plumes attaining the form of convective rolls (in shear flow) or convective cells (in free flow).

In geophysical flows, the mixed layer growing commonly occurs within the background of stable stratification: the pycnocline in the ocean, the thermocline in lakes and the capping nocturnal inversion layer in the atmosphere. The mixed layer growing is thus limited since a considerable amount of the turbulent kinetic energy is converted into potential energy during the penetration of turbulent flow into the adjacent stable layers. The entrainment of sinking plumes is therefore called penetrative convection. The appropriate dimensionless number characterising the interaction of convective flow and stable stratification is a Froude number, $Fr = (\tau_* \cdot N)^{-1}$. It is based on the inverse of the Brunt-Väisälä frequency N ,

$$N^2 = g \frac{\partial \rho}{\partial z}$$

which forms the appropriate time scale for mixing in stable stratified flows and the time scale of the convective flow τ_* . The convective time scale is given by the ratio of mixed layer depth and Deardorff velocity, $\tau_* = D/w_*$ and is therefore also called *large eddy-turnover time*.

Although the entrainment process is common to nearly all turbulent geophysical flows, it is generally not well understood since detailed measurements are extremely difficult. From a practical perspective, the parameterisation of entrainment is important but usually inadequate in most mixed layer models. Numerous laboratory studies have attempted to model an idealized entrainment process via convective tank experiments (e.g. Deardorff et al. 1980). The results, obtained

at low Reynolds number, have to be extrapolated to geophysical applications using scaling laws. Obviously, laboratory experiments cannot address sheared convective flows and their penetration because of the limited size of the domain. To study the detailed structure of the entrainment process is behind the scope of the present work. However, since the SGS model is extended to capture stratification effects, it might be enlightening to compare the numerical results to one-dimensional bulk modelling and to consider the connection of shear and entrainment efficiency. Recent attempts to capture the entrainment process in one-dimensional bulk approaches are presented in Chapter 4.

In the present work, the method of large-eddy simulation (LES) is applied which is capable to simulate the detailed plume dynamics of high Reynolds and Rayleigh numbers typical for oceanic convective flows.

Previous, simpler versions of the numerical model used here have been successfully applied in the simulation of near-surface oceanic convection. It has been coupled with a sea-ice model to investigate the interaction of oceanic convection with sea ice (Kämpf and Backhaus 1998, Backhaus and Kämpf 1999), with a biological production model to study the effect of oceanic convection on primary production (Backhaus et al. 1999, Wehde and Backhaus 2000, Wehde et al. 2001) and with a carbon dioxide flux model to simulate the atmosphere-ocean exchange of CO_2 (Wehde and Backhaus 1999) in unstable conditions.

Using the LES data set, mean and turbulent quantities in three different convective flows affected by different levels of wind-driven shear are analysed. One scenario is the reference case of negligible shear resulting in a free convective boundary layer. The other two are sheared convective boundary layers affected by a steady wind forcing of 7 and 14 ms^{-1} , respectively. The model domain is chosen sufficiently shallow so that rotational influences on the plume dynamics (Maxworthy and Narimousa 1992, Mironov et al. 2000, Mertens 2000) are negligible.

The wind effect on convection might in principle be masked by surface-wave effects as will be discussed in Chapter 2. However, in polar oceans surface waves are often damped by ice formation (Martin and Kauffman 1981). For this reason, surface-wave effects are explicitly excluded in this work. The unresolved motions have to be parameterised by the SGS turbulence model. The studies by Deardorff (1970), Mason and Thomson (1992), Moeng and Sullivan (1994) and Khanna and Brasseur (1998) indicate that shear-dominated flows require careful formulation of the SGS model. This point will be further investigated in Chapter 3.2.2. Consequently, for the present LES model a second-order closure approach following Canuto et al. (2001) was applied.

The work is divided into eight Chapters. Chapter 2 deals with the theoretical treatment of atmospheric and oceanic boundary layers. In Chapter 3, the foundations of the LES model are described. The description includes the filter operation, the physical principles of the turbulence closure and the underlying model equations. Chapter 4 is devoted to the implementation of the mathe-

matical model. It contains numerical algorithms as well as boundary and initial conditions and the implementation of the turbulence closure. In Chapter 5, a short overview of bulk modeling is given which is used to configurate the numerical experiments described in Chapter 6 and tested against the results which are presented in Chapter 7. Chapter 8 summarises the results and gives an outlook on future work.

Chapter 2

Geophysical boundary layers

2.1 Ekman layer theory

The ocean surface is not in contact with a solid surface but imposed to atmospheric forcing. For this reason the oceanic Ekman layer departs from its counterpart in the atmosphere in which the tangential velocities vanish at the surface (*no slip* condition). Instead, continuity of pressure and continuity of frictional stress across the ocean surface will be used as upper boundary conditions. The classic Ekman theory (Ekman 1905) delivers the steady-state motion of a boundary layer in which the Coriolis force is balanced by friction stress. The profiles of the horizontal velocities U, V (which are departures from the geostrophic velocity) can be calculated from the Ekman equations assuming infinite depth and horizontal homogeneity and a steady-state,

$$\begin{aligned} 0 = \frac{\partial U}{\partial t} &= f_z V - \frac{\partial \langle uw \rangle}{\partial z}, \\ 0 = \frac{\partial V}{\partial t} &= -f_z U - \frac{\partial \langle vw \rangle}{\partial z}. \end{aligned} \tag{2.1.1}$$

The turbulent stresses $\langle u_i w \rangle$ ($i = 1, 2$) are approximated by an eddy viscosity approach,

$$\langle u_i w \rangle = -\nu_t \frac{\partial U_i}{\partial z}. \tag{2.1.2}$$

In order to solve the above equations analytically the eddy viscosity is assumed to be a constant. At the free surface at $z = 0$ they are subject to the tangential stresses

$$\frac{\tau_i}{\rho_0} = -\nu_t \frac{\partial U_i}{\partial z} \Big|_{z=0}. \tag{2.1.3}$$

The integration of equation (2.1.1) with the upper boundary conditions yields

$$\begin{aligned} U &= e^{-z/\delta} (C_1 \cos(z/\delta) + C_2 \sin(z/\delta)), \\ V &= e^{-z/\delta} (-C_1 \sin(z/\delta) + C_2 \cos(z/\delta)), \end{aligned}$$

with

$$\begin{aligned}\delta &= \sqrt{\frac{2\nu_t}{f_z}}, \\ C_1 &= -\frac{\delta}{2\nu_t}(\tau_1 + \tau_2), \\ C_2 &= \frac{\delta}{2\nu_t}(\tau_1 - \tau_2).\end{aligned}$$

The depth in which the flow is damped to $\exp(-\pi)$ of its surface value is called *Ekman layer depth* D_{ek} ,

$$D_{ek} = \pi \sqrt{\frac{2\nu_t}{f_z}}. \quad (2.1.4)$$

The surface velocity vector is seen to be 45° to the right of the applied stress (in the northern hemisphere).

The assumption of a constant eddy viscosity is hard to justify in geophysical boundary layer flows. Observations show that the turning angle between surface current and geostrophic flow is less than the 45° predicted by classic Ekman theory (Tritton 1988). However, the most important property of the Ekman theory is that the horizontal mass flux associated with the Ekman-layer velocity is perpendicular to the wind stress (e.g. Kraus and Businger 1994). The magnitude of the mass flux in the Ekman layer does not depend on the value of the eddy viscosity. It is independent of any assumption about the turbulence. Consequently, for the description of the wind-driven oceanic boundary layer it is sufficient to know the wind field which is commonly available from routine measurements. The connection between boundary layer and interior ocean is described by the *Ekman layer suction*, i.e. the interior vertical velocity at the lower edge of the Ekman layer. It can be shown to be proportional to the divergence of the wind field.

However, the underlying assumption is that the stratification is close to neutral. It has been shown in an article by Barcilon (1967) that unstable stratification can inhibit vertical motions. As a result, the Ekman layer suction is prevented from controlling the dynamics of a rotating stratified flow.

2.1.1 The stratified Ekman layer

There are some limited solutions of the Ekman equations in the atmosphere possible without having to resort to turbulence closure assumptions. The solutions can be extended to take stratification effects into account using observational data. Therefore, it might be helpful to start the discussion with a look at the atmospheric boundary layer. For the sake of simplicity in the following discussion the x -axes will be aligned in the direction of the surface stress.

Geostrophic drag laws (e.g. Tennekes and Lumley 1982) relate the geostrophic

velocity outside the Ekman layer to the surface stress by asymptotic matching procedures (*Rossby-number similarity*). Two layers with distinct intrinsic length scales are matched. The one is the so-called inner layer in which the relevant length scale is the roughness length z_0 , the other is the so-called outer layer in which the relevant length scale is the Ekman depth D_{ek} . Under turbulent conditions, $D_{ek} \approx \kappa u_* / f$ where $\kappa = 0.4$ is v. Karman's constant. There exist an overlap region in which both scaling laws hold simultaneously provided that the Rossby number $Ro = D_{ek}/z_0$ is very large. A typical atmospheric value is $Ro \sim 10^3 m / 10^{-2} m = 10^5$. Matching of both layers yields the logarithmic law of the wall. More important for the present consideration is the profile of the turbulent Reynolds stress components which are given by (Kantha and Clayson 2000)

$$\begin{aligned} \langle uw \rangle &= -u_*^2 \left(1 - \frac{\mathcal{B}z'}{D_{ek}} \right), \\ \langle vw \rangle &= -u_*^2 \frac{z'}{D_{ek}} \left(\ln \frac{\kappa z'}{D_{ek}} + \mathcal{A} - 1 \right). \end{aligned}$$

For atmospheric conditions the Ekman layer height is much larger than the surface distance of the point under interest. Since the integration constants \mathcal{A} and \mathcal{B} are of order one, the profiles of the Reynolds stress components are close to constant throughout the surface layer.

If the stratification is not neutral, a similar matching can be done but another length scale enters the problem, the Monin-Obukhov length scale (Monin and Obukhov 1954) $L = u_*^3 / (\kappa B_0)$ (which is negative for unstable bouyancy flux). The integration constants \mathcal{A} and \mathcal{B} become similarity functions of the Monin-Kazanski parameter μ based on the Ekman layer extension D_{ek} and the Monin-Obukhov length L ,

$$\mu = \frac{D_{ek}}{L}. \quad (2.1.5)$$

From measurements the functional forms of $\mathcal{A}(\mu)$ and $\mathcal{B}(\mu)$ are known. However, the large scatter of the data raises some doubt as to whether the Ekman layer height D_{ek} is the relevant length scale of the unstably stratified atmospheric Ekman layer. Typical values for atmospheric conditions are $D \sim 1000m$, $B_0 \sim (10^{-3} - 10^{-2})m^2s^{-3}$, $u_* \sim 1ms^{-1} \rightarrow D_{ek} \sim 2000m$. They show that the mixed layer is often shallower than the Ekman layer. Therefore, better agreement between the data and theory can be achieved by defining the Monin-Kazanski parameter based on the mixed layer extension D ,

$$\mu = \frac{D}{L}. \quad (2.1.6)$$

By doing so, the similarity functions $\mathcal{A}(\mu)$ and $\mathcal{B}(\mu)$ under unstable conditions are approximated by (Yamada 1976)

$$\mathcal{A}(\mu) = 10.0 - 8.145(1 - 0.008376\mu)^{-1/3},$$

$$\mathcal{B}(\mu) = 3.020(1 - 3.290\mu)^{-1/3}.$$

For very unstable conditions, the similarity functions $\mathcal{A}(\mu)$ and $\mathcal{B}(\mu)$ become larger and the Reynolds stress profiles get a linear shape.

It can be summarized that in most cases of interest the Ekman layer height is not a relevant parameter in atmospheric boundary layer dynamics. The relevant length scale is the mixed layer height which marks the limit for surface friction processes to be significant. The shape of the Reynolds stress profiles is close to constant in the surface layer and become linear with increasing surface distance and/or increasing unstable stratification.

2.2 Numerical and observational studies

A review on large eddies of the atmospheric boundary layer covering theoretical, observational and numerical investigations was presented by Etling and Brown (1993). From stability theory, numerical simulations and laboratory experiments three instability modes have been identified: thermal instability, inflection-point instability and parallel instability. Although there are these three candidates for the large-eddy formation, most researchers attribute the formation by the interaction of strong shear with thermal instabilities (Etling and Brown 1993). Numerical and observational results provide a quantitative estimate of the ability of mean shear to organize the bouyant plumes into roll-like structures. The underlying mechanism for roll formation is probably the alignment of the temperature fluctuations in the high shear region near the surface (Sykes and Henn 1989). The convective rolls then cover the entire mixed layer depth. Thus, the shear can influence the bouyant eddies throughout the entire mixed layer. As control parameter for the formation of either convective rolls or convective cells, Deardorff (1972) identified the ratio of friction velocity to the convective velocity scale, $\Pi_* = u_*/w_*$. The role of Π_* can be illustrated in the budget equation for the turbulent kinetic energy K which reads in the horizontal homogeneous stationary boundary layer as

$$0 \approx P_S + \frac{\partial F}{\partial z} - B - \varepsilon, \quad (2.2.1)$$

where $P_S = - \langle uw \rangle \partial U / \partial z - \langle vw \rangle \partial V / \partial z$ is the production rate of turbulence due to the interaction of mean shear with the Reynolds stresses $\langle uw \rangle, \langle vw \rangle$, F is the vertical flux of turbulent kinetic energy, B is the buoyancy flux and ε is the turbulent dissipation rate. The Monin-Obukhov similarity theory for turbulent surface layers (Monin and Obukhov 1954) states that the only relevant parameters close to the surface are friction velocity u_* and distance from the surface z' . Let the near-surface values be denoted by the index

'0'. As a result, the production rate $P_{S,0}$ due to shear is approximated ¹. by

$$P_{S,0} \approx -\frac{u_*^3}{\kappa z'}. \quad (2.2.2)$$

Near the surface it is appropriate to identify the mixed layer depth with the surface distance, $D \approx z'$ (Wyngaard and Brost 1984). The ratio of production rates due to shear and buoyancy can be expressed as

$$-\frac{P_{S,0}}{B_0} = \left(\frac{u_*}{w_*}\right)^3 = \Pi_*^3. \quad (2.2.3)$$

The ratio is related to the ratio of the two relevant length scales in atmospheric stratified surface layer turbulence, namely the surface distance z' and the Monin-Obukhov length L as

$$\Pi_* = \kappa^{1/3} \cdot \left(\frac{-z'}{L}\right)^{-1/3}. \quad (2.2.4)$$

However, no agreement exists about the exact value of the threshold value Π_*^{th} at which the convective flow organises in roll structures. Sykes and Henn (1989) report $\Pi_*^{th} \approx 0.35$ whereas Moeng and Sullivan (1994) find $\Pi_*^{th} \approx 0.65$ and Khanna and Brasseur (1998) observe clear roll vortices in runs at $\Pi_* = 0.37$ and $\Pi_* = 0.51$. Observations by Grossman (1982) agreed with the early numerical study by Deardorff (1972) that $\Pi_*^{th} \approx 0.43$. For $\Pi_* \approx 0.58$, Walter and Overland (1984) and Brümmer (1985) observed roll structures. Clearly, for very large values of Π_* the flow is close to neutral. Zilitinkevich (1994) recommends to regard $\Pi_* = 2$ as upper bound for any convective effect.

Moeng and Sullivan attribute the different findings compared to Sykes and Henn (1989) to the inclusion of the Coriolis effect in their study which is absent in the study by Sykes and Henn. These authors regarded a plane Couette flow with heating, i.e. shear was taken as varying linearly whereas in Ekman layers shear shows exponential and turning behaviour. However, the linear approximation is justified as long as the Ekman layer extension is much larger than the mixed layer extension. It was shown that this is often true in atmospheric convection, consequently the Ekman layer height does not enter the list of relevant parameters. Simply adopting the atmospheric approach from (2.2.3), a value of $\Pi_*^{th} = 0.4$ would correspond to

$$D^{th} = -\frac{w_*^3}{B_0} = -(\Pi_*^{th})^{-3} \cdot \frac{u_*^3}{B_0} \sim 1600m \quad (2.2.5)$$

for moderate wind condition ($u_* \sim 10^{-2}m s^{-1}$) and moderate unstable buoyancy flux ($B_0 \sim -10^{-8}m^2 s^{-3}$). The formula states that convective roll structures

¹It is emphasized that the relations (2.2.1)-(2.2.2) only hold in the sense of an ensemble average or equivalently averaged over a horizontal domain of at least several km .

dominate the mixed layer down to a depth of $\sim 1600m$. This is an estimation for Greenland Sea condition. In contrast, the critical depth in the Labrador Sea is smaller by a factor of three due to its larger thermal expansion coefficient. Wind effects in 1600 m depth is clearly in conflict with the assumption that wind only affects the upper 100 – 200 m .

2.3 Difference between atmospheric and oceanic boundary layers

It can be seen that simply adopting the atmospheric threshold value Π_*^{th} to oceanic convection leads to unrealistic results. In contrast, the Rossby-number similarity procedure is hardly applicable in the ocean since the wave-influenced depth usually exceeds the theoretical depth of the inner layer (Kraus and Businger 1994). Wave breaking is known to create a substantial deviation from the 'law of the wall' (e.g. Kantha and Clayson 2000). Measurements show that under strong winds a region develops in the upper few meters in which the dissipation rate is much larger than predicted by the law of the wall (Melville 1994). Below these depths the law of the wall is often recovered. Under convective conditions the dissipation rate behaves similar to the atmospheric dissipation rate (Shay and Gregg 1986) although the larger scatter indicates the presence of wind-wave processes. The interaction between wind and sea surface is associated with additional length scales which are subject of ongoing research. To present knowledge, a wave-enhanced layer forms near the surface. Below that, the law of the wall is found in greater depths. The wave-enhanced layer is characterised by an approximate balance of turbulent transport and dissipation whereas the law of the wall requires an approximate balance of shear production and dissipation (Burchard 2002). A suitable formulation of boundary conditions for wind-wave interaction has been demonstrated by Craig and Banner (1994) and Craig (1996). Langmuir circulation is the most prominent feature of surface wave-turbulence interaction. It is considered to be caused by the vortex force that arises in a perturbation theory for the wave-averaged currents by Craik & Leibovich (1976). This perturbation theory has been integrated into LES models (Skylningstad and Denbo 1995; McWilliams et al. 1998) to explicitly resolve the dynamics of Langmuir circulation. Another example of surface wave-turbulence interaction is wave pumping. It describes the effect of a moving surface wave causing the surrounding fluid to move with it. Nonlinear wave pumping can induce a mean surface stress. LES results including this process can be found in the study by McWilliams et al. (1998). A generalized surface-layer model has been proposed by Huang (1979) which includes the balance between Coriolis forces due to the mean and wave-induced motions and the surface wind stresses. The result indicates that surface currents can be generated not only by direct wind stress, as in the classic Ekman

model, but also from the Stokes drift derived from the surface wave field, in an interrelated manner.

Even if surface wave effects can be neglected, as it is done in the present study, the Rossby-number similarity procedure is questionable. The oceanic Ekman layer is shallower by a factor of roughly 30, the square root of the density ratio, whereas z_0 is a nearly unknown value (Burchard 2002). It can be estimated that the typical Rossby number will be at least two orders of magnitude smaller than in the atmosphere, therefore the matching procedure might get invalid. The Ekman layer depth is indeed limited to at most 100- 200 *m* whereas convective mixing may homogenize the whole water column down to the bottom in several *km* depth. Thus, due to the shallowness of the Ekman layer in the ocean convection will generally cover depths much larger than the Ekman layer, as opposed to the atmosphere.

The main result of the analysis in this Chapter is that the appropriate scaling variables in atmospheric sheared convection are the distance from the surface z' (alternatively the mixed layer height D), the Monin-Obukhov length L , the friction velocity u_* and the Deardorff velocity w_* . The ratio of the velocities u_*/w_* can be related to the ratio of the length scales. Hereby, the nondimensional height z'/L is valid for the surface layer whereas in the bulk of the flow D/L (the Monin-Kazanski parameter) is appropriate.

Since there are no other scaling suggestions for oceanic sheared convection known to the author, the predictions of this Chapter will be compared to the numerical findings keeping in mind their limited validity. In the oceanographic context, however, the role of the Ekman layer with regard to convective penetration needs further investigation.

Chapter 3

Large Eddy Simulation

Turbulent flows contain a wide range of length and time scales where the large scale motions are generally much more energetic than the small scale ones. An estimation of the number of eddies (corresponding to the degrees of freedom) in a turbulent flow is made in the following. Let \mathcal{L} and η be the characteristic size of the biggest and the smallest eddies, respectively. Thus, the number M of eddies within a cube of volume \mathcal{L}^3 can be estimated as $M \sim (\mathcal{L}/\eta)^3$. The smallest size of eddies η (*Kolmogorov scale*) is given from dimension analysis as a function of molecular viscosity ν_{mol} and turbulent energy dissipation rate ε by $\eta = (\nu_{mol}^3/\varepsilon)^{1/4}$. Hence the number of degrees of freedom is of the order $M \sim \mathcal{L}^3 \varepsilon^{3/4} / \nu_{mol}^{9/4}$. Using the estimation of a characteristic velocity scale $U \sim (\mathcal{L}\varepsilon)^{1/3}$, the degrees of freedom can be related to the Reynolds number $Re = U\mathcal{L}/\nu_{mol}$ in the following way:

$$M \sim Re^{9/4}$$

In the oceanic boundary layer one finds Reynolds numbers of $10^7 - 10^8$ corresponding to the requirement of $10^{15} - 10^{18}$ grid points to resolve the turbulent motion. These numbers must be contrasted with today's supercomputers that can handle at most 10^9 grid points. Solving the Navier-Stokes equations for all of the motions in the flow in a *direct numerical simulation* (DNS) is therefore restricted to Reynolds numbers on the order of 10^4 .

In order to decrease the degrees of freedom, *large-eddy simulations* (LES) apply a local spatial filter to the basic equations. The simulation explicitly describes the large-scale turbulent motions, i.e. the low-frequency modes, while the unresolved small-scale motions, i.e. the high-frequency modes, are parameterised. Resolved and unresolved motions are separated by the filter operation under the (questionable) assumption that this separation does not influence the resolved motions significantly. The filter scale is assumed to be well within an inertial subrange of three-dimensional turbulence. The unresolved part is primarily responsible for dissipation of the resolved turbulent kinetic energy which is captured by the numerical model. The process of dissipation can be modeled in the framework

of Kolmogorov's (1941) inertial subrange theory, e.g. by an eddy-viscosity approach. Apparently, much of the uncertainty regarding LES results arise because there are regions in the flow field where the turbulent scale is sharply reduced and becomes smaller than the filter scale. This is especially true for boundary regions but it holds for strongly stratified regions as well. Here, Kolmogorov's inertial subrange theory does not apply.

Starting with the filter equation the governing LES equations are derived in Section 2.1. The importance of SGS modeling and a short review of common approaches is considered in Section 2.2. This discussion is followed by the presentation of the novel second-order closure approach in Section 2.3. In Section 2.4 the resulting model equations are summarized.

3.1 The filter operation

In geophysical applications it is common practice to neglect viscous friction in the high-Reynolds number limit. Consequently, no molecular effects are captured by the model as the flow is assumed to be fully turbulent anywhere. On the momentum equations for an incompressible inviscid fluid with velocity components U_i ($i=1,2,3$), dynamic pressure P and external force F_{ext} (skipping rotational terms),

$$\frac{\partial U_i}{\partial t} + \frac{\partial(U_i U_j)}{\partial x_j} = -\frac{1}{\rho_0} \frac{\partial P}{\partial x_i} + F_{ext}, \quad (3.1.1)$$

a spatial filter operation is applied which separates the fields into a filtered part (denoted by an overbar) and a fluctuation (denoted by small letters),

$$U_i = \overline{U_i} + u_i. \quad (3.1.2)$$

Commonly, explicit filtering of the basic equations is replaced by implicit filtering due the numerical grid (Sagaut 2001). This greatly complicates the theoretical analysis as different numerical algorithm will create different filtering properties. The formal decomposition results in

$$\frac{\partial \overline{U_i}}{\partial t} + \frac{\partial(\overline{U_i} \cdot \overline{U_j})}{\partial x_j} = -\frac{1}{\rho_0} \frac{\partial \overline{P}}{\partial x_i} + \frac{\partial \tau_{ij}}{\partial x_j} + \overline{F_{ext}}. \quad (3.1.3)$$

Equation (3.1.3) represents the dynamics of the large-scale motion. It cannot be solved yet, because it involves the unknown quantity $\overline{U_i U_j}$ which is absorbed into the definition of the subgrid scale (SGS) stress tensor

$$\tau_{ij} = -(\overline{U_i U_j} - \overline{U_i} \cdot \overline{U_j}). \quad (3.1.4)$$

The SGS stress tensor has to be parameterised by known quantities. Following Leonard (1974) and filtering the field a second time yields three sets of terms

$$\begin{aligned}
\tau_{ij} = & \overline{\overline{U_i \cdot U_j}} - \overline{U_i U_j} \\
& + \overline{\overline{U_i} u_j} + \overline{\overline{U_j} u_i} \\
& + \overline{u_i u_j}.
\end{aligned}
\tag{3.1.5}$$

There is a clear difference between the SGS stress tensor and the Reynolds stress tensor in statistical turbulence modeling which is build on the *Reynolds averaged Navier-Stokes* (RANS) equations. The SGS stress tensor only equals the Reynolds stress tensor $\overline{u_i u_j}$ for filters that satisfy the properties of ensemble averaging, namely

$$\begin{aligned}
\overline{\overline{U_i \cdot U_j}} &= \overline{U_i U_j}, \\
\overline{\overline{U_i} u_j} &= 0.
\end{aligned}
\tag{3.1.6}$$

Hence, if Reynolds (=ensemble) averaging were applied to (3.1.5), the first two terms on the right hand side would vanish and the twice filtered field would be equal to the once filtered field. Reynolds averaging implies that there is a clear scale separation between the mean and the fluctuating part. This is often true in mesoscale geophysical flows where turbulent and mean scales are observed to be separated by a 'spectral gap' (Stull 1988). The spectral gap expresses the fact that two different time scales are involved in mesoscale dynamics: the fast turbulent time scale and the comparatively slow mean flow time scale.

In contrast to RANS modeling, the filtering process in LES modeling invokes volume averaging which does not have the properties (3.1.6) of ensemble averaging. Ensemble averaging removes all the turbulence. In contrast, volume averaging only removes those components of the turbulent spectrum having smaller spatial scales than the filter scale. As a result, the three sets of terms in (3.1.5) have to be kept, each representing a different effect of the unresolved motions on the resolved motions. The terms in the first line represent the interaction of two resolved eddies to produce small scale turbulence. Because turbulence is transferred from the resolved to the unresolved scales, this term is called outscatter term. The terms in the second line represent the interaction between resolved scale eddies and small scale eddies. These terms, summarized as cross term, can transfer energy in either direction, but, on the average, transfer energy from the large scales to the small ones. The last term represents the interaction between two small scale eddies; as it may produce energy transfer from the small to the large scales, it is called the backscatter term; as noted above, the cross term may produce backscatter as well.

Obviously the interaction between resolved and unresolved motions is stronger than in RANS models. In LES, the smallest of the resolved and the largest of the unresolved scales have similar time scales, giving rise to a resonance, which is known to alter the Kolmogorov spectrum (Canuto 1994). As by far the most of the turbulent kinetic energy is contained in the resolved motions, the SGS

model is assumed to be less crucial than the turbulence model in Reynolds averaged flows. There have been suggestions how to approximate outscatter and cross terms by Taylor series expansion (Leonard 1974), (Clark et al., 1979). Nowadays, with respect to the uncertainty in modeling the SGS stress tensor it is common practice to neglect outscatter and cross term (Ferziger 1996). Then the components of the SGS stress tensor can be identified as SGS Reynolds stress terms. Equation (3.1.2) demonstrates the decomposition of the velocity field into a mean and a fluctuation part. The same procedure is carried out for the temperature field,

$$T = \bar{T} + \theta.$$

3.2 Introduction to SGS modeling

The most commonly SGS model was first proposed by Smagorinsky (1963)¹. It will be the starting point for a discussion of commonly used SGS models. In the concept of LES it is assumed that although it cannot provide detailed information about all the turbulent scales in the flow field, it should give the correct low-order statistics of the mean flow field such as mean velocity or temperature. As has been said above LES produces satisfactory results when the main producing mechanism of turbulence is well resolved. Then the SGS model mainly serves to drain the proper amount of energy from the resolved flow field. In those cases the importance of SGS effects is minor. However, when the significant mechanism of turbulence production is not fully resolved, SGS effects might even dominate. Examples are discussed in Section 3.2.2.

3.2.1 The Smagorinsky model and its shortcomings

In the Smagorinsky model subgrid stresses τ_{ij} are related to the filtered fields via the down-gradient assumption

$$\tau_{ij} - \frac{1}{3}\tau_{kk}\delta_{ij} = -2\nu_{Sm}S_{ij}, \quad (3.2.1)$$

where ν_{Sm} is the Smagorinsky SGS eddy viscosity, $S_{ij} = 1/2(\partial\bar{U}_i/\partial x_j + \partial\bar{U}_j/\partial x_i)$ is the rate-of-strain tensor and δ_{ij} is the Kronecker symbol.

The Smagorinsky approach can be extended in order to include buoyancy effects. The SGS eddy viscosity is assumed to be isotropic and given by the scalar

$$\nu_{Sm} = \lambda^2 \cdot S \cdot f(Ri), \quad (3.2.2)$$

¹In the following, whenever referring to Smagorinsky, reference is made to Smagorinsky (1963).

where λ is the SGS mixing length scale and $S = (2S_{ij}S_{ij})^{1/2}$. Additionally, $f = (1 + \sigma_0^{-1} Ri)^{1/2}$ accounting for stratification effects is a function of the gradient Richardson number Ri and the turbulent SGS Prandtl number σ_0 . The gradient Richardson number is given by $Ri = N^2/S^2$ where N is again the Brunt-Väisälä frequency. It can be seen from (3.2.2) that the Smagorinsky model is a three-dimensional mixing length approach.

In a grid point model the filter scale l_c can be related to the grid space $^2\Delta$. Inertial subrange theory allows to relate the mixing length scale λ to the grid space via

$$\lambda = C_S \cdot \Delta, \quad (3.2.3)$$

The Smagorinsky constant C_S has been found experimentally to be about 0.2 (Mason 1994). Within this approach, the SGS heat fluxes are computed analogously to the momentum fluxes,

$$\overline{u_i \theta} = -\chi_{Sm} \cdot \frac{\partial T}{\partial x_i} \quad (3.2.4)$$

with the SGS eddy diffusivity χ_{Sm} . The SGS Prandtl number σ relates SGS eddy viscosity and SGS eddy diffusivity via

$$\sigma = \frac{\nu_{Sm}}{\chi_{Sm}} \quad (3.2.5)$$

and is for simplicity taken as a constant, namely as its value under neutral conditions, σ_0 .

In applications it is found that the Smagorinsky 'constant' C_S is a rapidly varying function of the flow field (Ferziger 1996). This is a hint that the Smagorinsky model contains some deficiencies which will be discussed in the following.

The main assumptions of the Smagorinsky model are alignment of SGS stresses and strain rate (down-gradient assumption), the inertiality of the SGS, and a local equilibrium of turbulence (Canuto and Cheng 1997). The limitations of these assumptions have been recognized by various authors:

- the down-gradient assumption is the major deficiency of the Smagorinsky model (Ferziger 1996) because the principal axes of the SGS stress and the rate of strain tensor are only aligned in the case of pure strain but not for flows with mean vorticity. Consequently, the eddy viscosity is actually a

²When dealing with grids of unequal sizes in each direction, e.g. $\Delta x < \Delta y < \Delta z$, the anisotropy can be accounted for by using an anisotropic three-dimensional filter. The analysis by Scotti et al. (1993) yields to zeroth order in $\log(a_i)$ (where $a_1 = \Delta x/\Delta z$ and $a_2 = \Delta y/\Delta z$ are the two grid aspect ratios) that $\Delta = (\Delta x \Delta y \Delta z)^{1/3}$. Additionally, for very large filter anisotropies, the Smagorinsky constant should be replaced by $C_s \cdot \psi(a_1, a_2)$ where the correction function $\psi(a_1, a_2) \approx \cosh \left(4/27 \cdot \left((\ln a_1)^2 - \ln a_1 \ln a_2 + (\ln a_2)^2 \right) \right)^{1/2}$ (Scotti et al., 1993). As an example, for $a_1 = a_2 = 4$, $\psi(a_1, a_2) \approx 1.15$.

tensor quantity (Meneveau et al. 2001). The turbulence anisotropy, induced by the continuous transfer of energy from the generally anisotropic resolved flow towards the turbulent fluctuations, cannot be accounted for by the scalar definition of the SGS eddy viscosity.

- the Smagorinsky model implies that only shear contributes to SGS Reynold stress and only the temperature gradient contributes to the SGS heat flux. Thus, neither the contribution of both shear and buoyancy terms to the SGS fluxes is taken into account nor can the well-known 'countergradient' effect³ be captured (Canuto 1994).
- obviously, the eddy diffusivity is a tensor quantity as well. Neglecting this property does not allow to account for random gravity waves in stratified flows (Canuto 1994).
- the use of a constant SGS Prandtl number is a consequence of the down-gradient assumption. It contradicts experiments which show that with increasing stable stratification flows transport momentum increasingly more efficiently than heat (e.g. Webster 1964).
- the assumption of inertiality is not justified near boundaries or stably stratified regions. In these regions, the turbulence might do work against gravity.
- the local equilibrium assumption is a questionable simplification. The implication of locality is obviously wrong in a convective boundary layer where turbulence may be generated at one point but dissipated somewhere else.

Despite the list of shortcomings of the Smagorinsky SGS model it was applied in a number of succesful simulations of free convective flows (e.g., Mason 1994). It must be deduced that in these flows the turbulence producing mechanism are well resolved and the deficiencies of the SGS model are of minor importance.

3.2.2 Modified Smagorinsky SGS models

In contrast to free convective flows which are apparently well suited for the LES approach, LES of other kinds of flow using the Smagorinsky model have been reported to provide unsatisfactory results as will be discussed below.

The low-speed streaks typical for shear-dominated flows carry most of the turbulent fluxes of momentum and heat in a turbulent boundary layer. They are preferentially generated near the surface (Deardorff 1972, Khanna and Brasseur 1998). Since resolving the small but dynamically important near-surface region

³The 'counter-gradient' heat flux expresses that individual bouyant elements can transport heat downwards although the mean temperature gradient is greater at the bottom. Obviously, this feature cannot be correctly described by an eddy viscosity relation between flux and local mean gradient.

is prohibitively expensive (Baggett et al. 1997) the main burden is placed here on the SGS model. It is well known that commonly used SGS models of the Smagorinsky-type even fail to reproduce similarity theory predictions (Deardorff 1970, Schumann 1975, Mason and Thomson 1992, Sullivan et al. 1994). In the first LES of turbulent channel flow, Deardorff (1970) was not able to obtain the correct mean velocity profile unless the Smagorinsky 'constant' was lowered to about half of the theoretical value. He observed that the theoretical value of $C_S \approx 0.2$ resulted in too much diffusion corresponding to excessive shear, and hence - by integration - errors in the mean velocity profiles. The resulting shortcomings have been demonstrated by Khanna and Brasseur (1998) comparing the performance of their LES of atmospheric sheared convection with the Smagorinsky and the Sullivan et al. (1994) SGS model, respectively. As the Smagorinsky model tends to overestimate shear production, it predicts low-speed streaks that are too pronounced and elongated in the streamwise direction. There have been a number of proposals how to overcome the deficiencies of the Smagorinsky model. Some of them will be discussed below.

Mason and Thomson (1992) found that errors in the mean velocity profiles have a substantial indirect impact on the whole simulation. They failed to remove this tendency by simply retuning C_S . Instead they introduced stochastic backward cascade processes. Stochastic modeling has also been investigated by Schumann (1995). Backward processes account for the fact that intermittently occurring turbulent kinetic energy is transferred from small to large scales (backward) whereas in inertial subrange theory only the (mean) forward cascade is considered. In the computation a stochastic part is added to the subgrid scale stress tensor. The stochastic part contains a white random number in space with a characteristic correlation time which is of the same order of magnitude as the subgrid time scale.

A different approach has been chosen by Schumann (1975) who added a new SGS term in his channel flow LES. His SGS model might be viewed as a combination of a real LES in the flow interior and a RANS model near the channel walls. This approach has been modified in the work by Sullivan et al. (1994) and has also been used in the above mentioned study of Khanna and Brasseur (1998). In their formulation the resolved strain field is decomposed into horizontal mean (denoted by angle brackets) and fluctuation part. The SGS stress tensor contains two parts:

$$\tau_{ij} = -2\gamma\nu_t S_{ij} - 2\nu_T \langle S_{ij} \rangle, \quad (3.2.6)$$

where $\gamma = S_{ij}/(S_{ij} + \langle S_{ij} \rangle)$ is an isotropy factor. Near a solid boundary, the resolved strain field is highly anisotropic which results in $\gamma \ll 1$ and the mean-field term dominates in (3.2.6). The mean field eddy viscosity ν_T is chosen to match similarity theory prediction. In the interior, the flow is close to isotropic, hence $\gamma \approx 1$ and the first term in (3.2.6) dominates. In this case, the Smagorinsky formulation (3.2.1) is recovered from (3.2.6). Sullivan et al. (1994) report that

is was not required to correct the SGS model for the heat flux in an analogous manner since the improvement of the velocity field improved the mean temperature field accordingly. It must, however, be noted that the Sullivan et al. (1994) SGS model is tuned towards the predictions of the Monin-Obukhov similarity theory.

Another improvement of the Smagorinsky approach has been achieved by the *Dynamical Mixed Model* (e.g. Germano et al. 1991) in which the 'constant' C_S has been made a function of flow variables in a dynamical procedure assuming similarity between the smallest resolved and the largest unresolved turbulence spectrum. As has been recently pointed out by Gallerano and Napoli (2001), most Smagorinsky-type models implicitly assume a balance between dissipation and production of a turbulent kinetic energy budget which is not the pure *unresolved* but also contains a part of *resolved* turbulent kinetic energy. This is due to the fact that the definition of the SGS stress tensor τ_{ij} (3.1.5) provides the following SGS turbulent kinetic energy \tilde{e} ,

$$\tilde{e} = \frac{1}{2}\tau_{ii} = \frac{1}{2}\left(\overline{\mathbf{U}_i \cdot \mathbf{U}_i} - \overline{U_i U_i} + 2\overline{\mathbf{U}_i \mathbf{u}_i} + \overline{\mathbf{u}_i \mathbf{u}_i}\right). \quad (3.2.7)$$

This expression contains two terms, the first and second term of the right-hand side, which depend solely on the resolved field. Hence, the energy \tilde{e} is not the *unresolved* turbulent kinetic energy and the assumption of local equilibrium, i.e. the balance of production and dissipation, is not justified for \tilde{e} . Alternatively, Gallerano and Napoli (2001) suggest the concept of a tensorial dynamic mixed SGS model which greatly increases the expense of the computation. Additionally, the dynamic model approach suffers from numerical instability and it is unclear how to account for body-force effects such as stratification or rotational strains which are often dominant in geophysical applications.

A different approach is the concept of nonlinear Reynolds stress modeling. It allows a nonlinear stress-strain relationship that transcend the Boussinesq hypothesis of a scalar eddy viscosity. The non-linear Reynolds stress model is based on analogies between the mean turbulent flow of a Newtonian fluid and the laminar flow of a non-Newtonian fluid⁴. Using a reduced form of the constitutive relation for the non-linear Rivlin-Ericksen (Rivlin and Ericksen, 1955) fluids, Pope (1975) developed a general eddy-viscosity hypothesis relating the SGS stresses to a finite number of known tensors and scalars. The mean flow tensors under consideration are rate-of-strain tensor S_{ij} and vorticity tensor $\omega_{ij} = 1/2 \cdot (\partial \overline{U}_i / \partial x_j - \partial \overline{U}_j / \partial x_i)$. The SGS stress tensor is assumed to be a functional of these tensors,

$$\tau_{ij} = \mathcal{F}(S_{ij}, \omega_{ij}) \quad (3.2.8)$$

which results in a polynomial of five tensor products $S_{ij}^{m_1} \omega_{ij}^{m_2}$ where $m_1, m_2 = 0, 1, 2$. Numerical experiments with this SGS model (Lund and Novikov, 1992)

⁴Additionally to turbulence problems, the constitutive law of simple non-Newtonian fluids has also been used in sea ice modeling, see e.g. Overland and Pease (1988)

yielded good results but are costly. In a simplified version the nonlinear model has been used by Kosovic (1997) in LES of the neutral shear-driven atmospheric boundary layer. Kosovic defined the SGS stress tensor as

$$\tau_{ij} = -c_{K1}\Delta \left(2e^{1/2}S_{ij} - c_{K2}\Delta(S_{ik}S_{kj} - \frac{1}{3}S_{mn}S_{mn}\delta_{ij}) - c_{K3}\Delta(S_{ik}\omega_{kj} - \omega_{ik}S_{kj}) \right) \quad (3.2.9)$$

where the coefficients have to be determined analytically. Kosovic (1997) recommends the values $c_{K1} = 0.116$ and $c_{K2} = c_{K3} = 0.823$. For setting $c_{K2} = c_{K3} = 0$ the linear down-gradient model is recovered. The second and third terms account for the backscatter of turbulent kinetic energy near the surface as well as its redistribution among the normal SGS stress components which are caused by anisotropy and nonlinear interactions. His results yielded the experimentally observed and theoretically predicted logarithmic mean velocity profile. While the linear Smagorinsky SGS model exhibited streaky streamwise velocity structures aligned with the mean wind, the nonlinear SGS model exhibited more chaotic and less coherent structures. As the Sullivan et al. (1994) SGS model, the Kosovic (1997) SGS model successfully reduces the excessive damping of the Smagorinsky model. It is, however, not obvious how to extend the expression (3.2.9) to stratified flows.

3.3 Second-order algebraic SGS model

In the present work, the SGS fluxes of momentum and heat are modeled by second-order closure. In RANS simulations Reynolds stress models are known for a long time (e.g. Launder et al. 1975, Speziale 1991). The aim of second-order closure models is to derive a close set of second-moment equations. In the present model, the differential equation for the turbulent kinetic energy will be solved explicitly while all the other second-order moments are given by algebraic relations. The derivation of the equations will be discussed in the following Chapter. It will afterwards be shown in Chapter 3.3.5 how simpler turbulence models (Smagorinsky, Kosovic) can be derived from the present formulation. Outscatter and cross terms from (3.1.5) are neglected due to the large modeling uncertainty.

3.3.1 Second-order closure in SGS modeling

The budget equation for the SGS turbulent kinetic energy $e = \frac{1}{2}\overline{u_i u_i}$ will be solved explicitly to avoid the above mentioned difficulties of a correct algebraisation which arises in the framework of 'Dynamical Mixed Models'. Obviously, information about the degree of anisotropy in the SGS turbulence cannot be gained from the SGS turbulent kinetic energy. Instead, the equations for the SGS Reynolds stress and the heat flux tensors are considered and solved in an

approximate manner.

In the framework of the Reynolds stress formalism and second-order closure, the following equations for the SGS turbulent kinetic energy e , the temperature variance $\overline{\theta^2}$, the anisotropic part of the SGS Reynolds stress tensor $b_{ij} = \tau_{ij} - 2/3e\delta_{ij}$ and the SGS heat flux $\overline{u_i\theta}$ are derived (e.g., Lumley et al. 1978):

$$\frac{De}{Dt} = -D_f(e) - b_{ij}S_{ij} + \lambda_k \overline{u_k\theta} - \frac{3}{2}\varepsilon_{ii}, \quad (3.3.1)$$

$$\frac{D\overline{\theta^2}}{Dt} = -D_f(\overline{\theta^2}) - 2\overline{u_i\theta}\frac{\partial T}{\partial x_i} - 2\varepsilon_\theta, \quad (3.3.2)$$

$$\frac{Db_{ij}}{Dt} = -D_f(b_{ij}) - \Sigma_{ij} - Z_{ij} + B_{ij} - \Pi_{ij} - \frac{4}{3}eS_{ij}, \quad (3.3.3)$$

$$\begin{aligned} \frac{D\overline{u_i\theta}}{Dt} = & -D_f(\overline{u_i\theta}) - \left(b_{ij} + \frac{2}{3}e\delta_{ij}\right)\frac{\partial T}{\partial x_j} \\ & - \overline{u_j\theta}S_{ij} + \lambda_i\overline{\theta^2} - \Pi_i^\theta - 2\epsilon_{ijk}\Omega_j\overline{u_k\theta}, \end{aligned} \quad (3.3.4)$$

where $D\eta/Dt = \partial/\partial t + U_j\partial\eta/\partial x_j$ for any quantity η , $D_f(\eta)$ contains third-order contributions from turbulent and pressure transport, $\lambda_k = (0, 0, g\alpha)$ with gravity g and thermal expansion coefficient α , ϵ_{ijk} is the antisymmetric tensor and ε_θ is half the dissipation rate of temperature fluctuations.

As can be seen from (3.3.1)-(3.3.4), the equations for the second-order moments contain unknown moments of third-order (ε_{ij} , $D_f(\eta)$, Π_{ij} , Π_i^θ) which are discussed in the next Chapter.

The traceless tensors in (3.3.3) are given by

$$\begin{aligned} \Sigma_{ij} &= S_{ik}b_{kj} + S_{jk}b_{ik} - \frac{2}{3}\delta_{ij}S_{kl}b_{kl}, \\ Z_{ij} &= b_{ik}\omega_{jk} + b_{jk}\omega_{ik} + \frac{1+c_5}{c_5}(\epsilon_{jkl}b_{ik} + \epsilon_{ikl}b_{jk})\Omega_l, \\ B_{ij} &= \lambda_i\overline{u_j\theta} + \lambda_j\overline{u_i\theta} - \frac{2}{3}\delta_{ij}\lambda_k\overline{u_k\theta}. \end{aligned} \quad (3.3.5)$$

While B_{ij} represents a source of turbulence due to buoyancy, Σ_{ij} and Z_{ij} represent anisotropic interaction of b_{ij} with the mean flow (described by S_{ij} and ω_{ij}). Again, ω_{ij} denotes vorticity. The exact value of the coefficient c_5 will be discussed below. It couples vorticity and Earth's rotation. The components of Earth's rotation are given by $\vec{\Omega} = (0, \Omega_2, \Omega_3) = 1/2 \cdot (0, f_h, f_z)$ with f_h, f_z the zonal and the vertical components of the Coriolis parameter, respectively⁵.

The terms on the right hand side of equation (3.3.1) can be interpreted as follows: The first one is the diffusive transport of turbulence by velocity and pressure fluctuations. The second one, called the 'production term' is the rate at which the

⁵In the present formulation f_h is neglected in the SGS model since in polar regions $f_h \ll f_z$.

mean flow does work on the turbulence. The third one is the buoyancy contribution which increases the amount of turbulent kinetic energy under unstable stratification and limits the amount under stable stratification conditions. Often, both terms are merged together as 'production term'. Finally, the last term of (3.3.1) describes the dissipation, i.e. the mean rate at which the turbulence does work against viscous stresses.

Similar, equation (3.3.2) expresses the fact that the amount of temperature fluctuations is changed by an imbalance of the diffusive transport (first term on the right-hand side), production rate of temperature fluctuations by mean temperature gradients (second term) and the dissipation of fluctuations through molecular processes (third term). The temperature variance is especially important in stratified turbulence as it is proportional to the turbulent potential energy ($TPE = \lambda_3^2 \overline{\theta^2} N^{-2}$).

The balance of SGS Reynolds stresses (3.3.3) is determined by turbulent transport (first term on the right hand side of (3.3.3)), shear (second term) rotation force (third term), buoyancy contribution (fourth term), pressure-strain correlation (fifth term) and shear production (last term). Neglecting the molecular dissipation in high-Reynolds number flow, it is the pressure redistribution which limits the growth of the fluxes.

The first term on the right-hand side of (3.3.4) denotes the rate of turbulent transport of temperature. The second and the third terms express the rate of creation of the heat flux due to the actions of mean temperature and mean velocity gradients, respectively, the former tending to increase the magnitude of temperature fluctuations, the latter the magnitude of velocity fluctuations. The fourth term represents augmentation of the heat flux due to gravity. Finally, the last term is the pressure-temperature gradient correlation, the counterpart of the pressure-strain correlation in the stress equations.

3.3.2 The Third-Order Moments

Closure of the set of second-order moment equations (3.3.1)-(3.3.4) requires elimination of the unknown third-order tensors related to the effect of turbulent and pressure transport (D_f), of pressure correlations (Π_{ij} , Π_i^θ) and of dissipation (ε_{ij}). The transport terms are entirely neglected (equivalent with assuming conditions of homogeneous turbulence) apart from the ones appearing in the equation for the turbulent kinetic energy (3.3.1). These third-order terms are implicitly accounted for by the upstream-discretization of (3.3.1) whereby the numerical induced diffusion is proportional to the velocity. Therefore, the numerical induced diffusion in vertical direction is probably too small near the surface where the vertical velocity is small but the flow is expected to be strongly inhomogeneous. Vertical diffusion is for this reason additionally modeled via

$$D_f(e) \approx -\nu_e \frac{\partial^2 e}{\partial z^2}. \quad (3.3.6)$$

The eddy viscosity ν_e has been adopted from Zeman and Tennekes (1975),

$$\nu_e = c_e \tau (\overline{w^2} + \frac{c_e}{2} \tau \lambda_3 \overline{w\theta}), \quad (3.3.7)$$

using the turbulent time scale $\tau = 2e/\varepsilon$, $\lambda_3 = g\alpha$, and $c_e = 0.3$.

The pressure-strain correlation tensor and the pressure-temperature gradient correlation tensor,

$$\begin{aligned} \Pi_{ij} &= \overline{u_i \frac{\partial p}{\partial x_j}} + \overline{u_j \frac{\partial p}{\partial x_i}}, \\ \Pi_i^\theta &= \frac{1}{\rho_0} \overline{p \frac{\partial \theta}{\partial x_i}}, \end{aligned}$$

are known to play a crucial role in determining the structure of most turbulent flows (Speziale 1991). In one-point closure, the pressure-correlations have to be modeled in terms of the known local tensors b_{ij} , S_{ij} , B_{ij} , ω_{ij} : start with the pressure-strain correlation tensor which is expressed following Launder et al. (1975). It can formally be derived as low-order Taylor-series expansion in b_{ij} about the isotropic-turbulence state (corresponding to $b_{ij} = 0$) in the case of homogeneous turbulence. Especially the underlying requirement of approximate vertical homogeneity of the mean shear is not satisfied in a geophysical surface flow. The coefficients therefore contain the consequences of inhomogeneity. In mathematical terms, the constraint of form invariance under coordinate transformations requires that Π_{ij} be an isotropic tensor function of its arguments,

$$-\Pi_{ij} \approx -\frac{C_{\Pi 1}}{\tau} b_{ij} + C_{\Pi 2} e S_{ij} - C_{\Pi 3} B_{ij} + C_{\Pi 4} Z_{ij} + C_{\Pi 5} \Sigma_{ij}, \quad (3.3.8)$$

where the first three terms describe the 'return-to-isotropy'-part, the mean shear interaction and the buoyancy contribution, respectively. The fourth and fifth term are symmetric tensors constructed from vorticity contribution and anisotropic production, respectively. The coefficients have to be calibrated from experiments and simplified calculations. An overview over the variety of recommended coefficients is listed in table 3.1⁶. In this work, the values $C_{\Pi 1} - C_{\Pi 4}$ are chosen following the plume experiments in Shih and Shabbir (1992) whilst $C_{\Pi 5}$ is taken equal to $C_{\Pi 4}$. An analogous procedure for the pressure-temperature gradient correlation tensor results in

$$-\Pi_i^\theta \approx -\frac{C_{\theta 1}}{\tau} \overline{u_i \theta} - C_{\theta 2} \lambda_i \overline{\theta^2} + C_{\theta 3} S_{ik} \overline{u_k \theta} + C_{\theta 4} (\omega_{ik} - \epsilon_{ikl} \Omega_l) \overline{u_k \theta} \quad (3.3.9)$$

where the coefficients (see table 3.2 for a collection)⁷ are taken from Shih and Shabbir (1992) as well. In most common second-order RANS models in geo-

⁶Some coefficients result from asymptotic considerations, e.g. the Rapid-Distortion theory result for $C_{\Pi 2} = 0.8$ by Crow (1968), and the isotropic result for $C_{\Pi 3} = 0.33$ by Launder (1976).

⁷In isotropic turbulence, $C_{\theta 2} = C_{\theta 3} = 0.33$ (Launder 1976). The coefficient $C_{\theta 1}$ is related to $C_{\Pi 1}$ via Equation (3.3.23).

Authors	$C_{\Pi 1}$	$C_{\Pi 2}$	$C_{\Pi 3}$	$C_{\Pi 4}$	$C_{\Pi 5}$
Champagne et al. (1970), <i>Wind tunnel data of homogeneous shear flow</i>	3.24	0.8	-	0.61	0.74
Wyngaard et al. (1974), <i>Atmospheric surface layer data</i>	3.46	0.8	-	0.45	0.62
Launder, Reece and Rodi (1975)	3.0	0.8	-	0.655	0.875
Gibson & Launder (1978)	3.6	0.8	0.6	0.6	0.6
Shih & Shabbir (1992)	4.76	0.8	0.4	0.57	0.98
Gatski and Speziale (1993) (linearised)	3.4	0.36	-	0.2	0.625

Table 3.1: Coefficients in the modeled pressure strain-correlation tensor

Authors	$C_{\theta 1}$	$C_{\theta 2}$	$C_{\theta 3}$	$C_{\theta 4}$
Gibson & Launder (1978)	6.0	0.33	0.33	-
Shih & Shabbir (1992)	7.5	0.42	0.6	1.0

Table 3.2: Coefficients in the modeled pressure temperature gradient-correlation tensor

physics, the correlation tensors are highly simplified by assuming $C_{\Pi 3} = C_{\Pi 4} = C_{\Pi 5} = 0$ (see, e.g., Mellor and Yamada (1982), Kantha and Clayson (1994), Burchard and Baumert (1995) and the detailed comparison study by Burchard and Bolding 2001)). However, it must be kept in mind that the recommended coefficients are derived for RANS calculations. It is not clear whether they can simply be adopted to LES calculations where a large amount of turbulence is resolved. As the small-scale dissipative structures are nearly isotropic, the dissipation tensor

$$\varepsilon_{ij} = 2\nu_{mol} \overline{\frac{\partial u_i}{\partial x_k} \frac{\partial u_j}{\partial x_k}} \quad (3.3.10)$$

is commonly modeled as

$$\varepsilon_{ij} = \frac{2}{3}\varepsilon\delta_{ij}. \quad (3.3.11)$$

There are different suggestions how to extend this expression to slightly anisotropic cases (Lewellen 1977, Canuto 1994) which contain (3.3.11) in the limit of $Re \rightarrow \infty$. However, these corrections are neglected here despite the presence of both shear and stratification. Durbin and Speziale (1991) argued that for local isotropy to be a valid approximation, the relation $S \cdot \tau \ll 1$ must hold. This is in conflict with the concept of algebraic stress modeling (see footnote 10 in this Chapter). The existence of local isotropy in stably stratified flows is the subject of current research. Experiments of van Atta (1991) reveal that stable stratification has a strong influence even on the smallest turbulent scales. The

commonly used isotropic model for the scalar dissipation rate reads

$$\varepsilon = \frac{e^{3/2}}{l_\varepsilon}, \quad (3.3.12)$$

where l_ε is the dissipation length scale. It can be deduced from inertial subrange theory to be connected to the effective grid size (footnote (2) in this Chapter) Δ by

$$l_\varepsilon = \frac{\Delta}{c_\varepsilon}, \quad (3.3.13)$$

where $c_\varepsilon = \pi \left(\frac{2}{3Ko} \right)^{3/2} \approx 0.85$ for the Kolmogorov constant $Ko \approx 1.6$.

In the presence of rotation the dissipation rate is known to decrease which means that the dissipation length scale tends to increase (Greenspan 1968). Rotation disturbs the energy cascade from the large to the small scales since the effective vorticity is suppressed. This is modeled following Canuto and Dubovikov (1997) and Canuto et al. (2001) by making the dissipation length scale a function of an inverse Rossby number $Ro = \Omega_3 \cdot l_\varepsilon^0 / e^{1/2}$ where l_ε^0 denotes the non-rotating dissipation length scale. The present formulation is a truncated version of the Canuto and Dubovikov (1997) expression. The complete derivation is given in the appendix A. The rotational correction function is given by

$$g(Ro) = \frac{l_\varepsilon^{rot}}{l_\varepsilon^0} = \frac{2}{1 + \sqrt{1 - Ro^2}} \quad (3.3.14)$$

In the non-rotational case, $g(Ro) = 1$ and (3.3.13) is recovered. The present formulation is obviously only valid for small inverse Rossby numbers, $Ro < 1$, i.e. slow rotation. It does not yield the correct limit $l_\varepsilon^{rot} \rightarrow \infty$ for rapidly rotating turbulence since for rapid rotation, the truncation of the Canuto and Dubovikov (1997) expression becomes invalid.

It is noted by Canuto et al. (2001) that since rotation tends to suppress the turbulent cascading while stratification increases it both effects have to be taken into account. However, it is expected that for the present application the effect of (3.3.14) is small since $Ro \ll 1$ in shallow convection. The effect of stratification is considered in the next Chapter.

3.3.3 Near-'wall' turbulence

The presence of a wall at the surface and of the density jump at the thermocline strongly affects the turbulent flow and limits the accuracy of the LES method. In both regions, the near-wall region and the entrainment zone, vertical motion is suppressed. The relevant turbulent length scale is determined by local conditions rather than by the LES filter scale (or equivalently, the grid spacing). As the energy-containing eddies of near-wall and entrainment region cannot be represented on the numerical grid, the main burden is placed here on the SGS model.

Commonly, it is assumed that in LES the subgrid scales can be described by a Kolmogorov inertial energy spectrum

$$E(k) = Ko \cdot \varepsilon^{2/3} k^{-5/3}, \quad (3.3.15)$$

where Ko is the Kolmogorov constant (≈ 1.6). In this range (*inertial subrange*), the energy spectrum is determined entirely by ε , the constant energy dissipation, and k , the magnitude of the wavenumber. By integrating over all wavenumber contributions, equation (3.3.12) is derived with l_ε given by (3.3.13). However, the assumption that the SGS eddies are isotropic is not valid in the near-wall region and the thermocline; more sophisticated SGS formulations are required. Some of them addressing the near-wall flow (Mason and Thomson 1992, Sullivan et al. 1994, Kosovic 1997) have been described in chapter 3.2.2.

In the present work, the SGS model modification is extended to the entrainment zone. The aim is to connect the grid spacing (which is the relevant turbulent length scale in isotropic turbulence, see (3.3.13)) with the appropriate turbulent length scales in both regions in a correct manner.

The surface region

Near the surface wall, the dissipation length scale is known to vary with distance from the surface. As a result, the number of grid points required to resolve the near-wall eddies increases dramatically. Baggett et al. (1997) calculated that the number of grid points needed for accurate LES of the turbulent boundary layer in shear flows scales as $M_* \sim Re_*^2$ where $Re_* = u_* l_\varepsilon / \nu$ is the friction Reynolds number. For the flows under consideration here, M_* is only slightly lower than the estimation for direct numerical simulation.

The most common approach to alleviate the near-wall resolution requirements is to replace the no-slip boundary condition with an appropriate 'wall model'. The wall model derives boundary conditions for the mean variables of the flow (see Chapter 3). In this Chapter the discussion is focussed on the effect of wall and thermocline on the SGS turbulent quantities.

The most pronounced effect of the presence of a wall on turbulence is impeding the energy transfer from the streamwise direction to that normal to the wall, thus shortening the relevant turbulent (wall-normal) time scale. Therefore, Gibson and Launder (1978) introduced wall damping corrections into the models of the pressure-strain and pressure temperature-gradient correlation tensors. This is not done here. Instead, the shortening of the turbulent time scale is implicitly incorporated within the formulation for the dissipation length scale which is proportional to the turbulent time scale. Near the wall, the dissipation length scale is known to grow linearly with the wall distance. It is computed by

$$l_\varepsilon^{wall} = a_1 \cdot \kappa(z' + z_0) \quad (3.3.16)$$

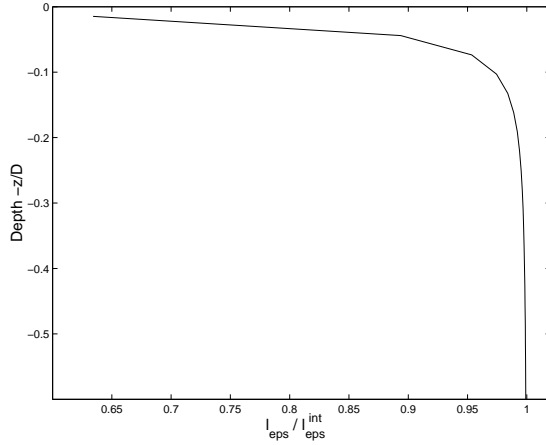


Figure 3.1: The dissipation length scale versus non-dimensionalised depth according to equation (3.3.17). In the interior, the dissipation length scale is constant and only a function of the grid spacing, see (3.3.13). Near the surface, it varies linearly with surface distance according to (3.3.16).

where $\kappa = 0.4$ is the von Karman constant, z' is the vertical distance from the surface, z_0 is the roughness length and the coefficient a_1 is derived following Mason (1994)⁸, $a_1 = (c_\varepsilon C_S)^{-1} = (15C_{\Pi 1}/4)^{3/4}$. In the interior of the flow, the inertial subrange result (3.3.13) is used which is valid for isotropic turbulence. For convenience it gets the label 'int' (for 'interior'):

$$l_\varepsilon^{int} = \Delta/c_\varepsilon$$

The two expressions are matched smoothly following Mason (1994) via

$$l_\varepsilon = l_\varepsilon^{int} \cdot \left(1 + (l_\varepsilon^{int}/l_\varepsilon^{wall})^2\right)^{-1/2}. \quad (3.3.17)$$

The shortening of the length scale towards the rigid surface is illustrated in Figure 3.1. Note that equation (3.3.12) relates dissipation length scale and dissipation rate. It is hence possible to account for enhanced dissipation, e.g. due to wave-breaking, by modifying the surface length scale formulation (3.3.16) to $l_\varepsilon^{wall} \sim z'^n$. A discussion of appropriate values for the exponent n is found in Burchard 2002.

The entrainment region

In the presence of stable stratification, especially in the thermocline, the dissipation length scale is strongly reduced. The validity of the Kolmogorov hypothesis

⁸Mason (1994) determines the mixing length scale (3.2.3) as $\lambda = (C_S \Delta) \cdot (1 + C_S \Delta / (\kappa(z' + z_0)))^{-1}$. The dissipation length scale is taken as proportional to his mixing length scale. The coefficient a_1 is seen to depend on the coefficient $C_{\Pi 1}$ from the model of the pressure-gradient correlation tensor (3.3.8).

is violated if there is any substantial transfer of energy directly into or out of the 'inertial subrange'. Consequently, in the presence of stratification, the energy spectrum may deviate from the '-5/3 power law': the buoyancy force tends to increase the dissipation rate by converting part of the turbulent kinetic energy into potential energy. Because velocity shear tends to decrease the dissipation rate by supplying kinetic energy to the turbulence, shear partially balances the deviation (Weinstock 1978). Therefore, both stratification and shear have to be taken into account. Cheng and Canuto (1994) generalised the inertial energy spectrum (3.3.15) to

$$E(k) = Ko \cdot \varepsilon(k)^{2/3} k^{-5/3} \quad (3.3.18)$$

and define a correction function

$$f(N, S) := \varepsilon(k)/\varepsilon$$

to express the deviation from isotropy. The correction function depends on shear frequency S and Brunt-Väisälä frequency N (for stable stratification, $N^2 < 0$), satisfying $f(N=0, S=0) = 1$. Using the relation (3.3.12) and the maximal resolvable wavenumber $k_{max} = 2\pi/2\Delta$, and after substituting the two-point closure result for $\varepsilon(k)$, the correction function reads as (Cheng and Canuto 1994, Canuto and Cheng 1997)

$$f(N, S) = \left(\int_0^1 \left(1 - b \ln(1 + a q^2) \right)^2 dq \right)^{3/2} \quad (3.3.19)$$

with

$$b = \frac{3^{1/2}}{8} Ko^{3/2} \beta (R_f^{-1} - 1), a = \frac{2}{\pi^2} Fr^{-2} f(N, S)^{2/3}$$

$$q := \left(\frac{k}{k_{max}} \right)^{-2/3}, Fr = \frac{e^{1/2}}{N \cdot \Delta}, \beta = \frac{1}{2},$$

where Fr is a Froude number and $R_f = B / -b_{ij} S_{ij}$ is the flux Richardson number. In order to use the function in a numerical model, the integral is approximated by Cheng and Canuto (1994), depending on the ratio between the critical and the actual Richardson number $r_f = R_f^{cr} / R_f$,

$$f(N, S) = \begin{cases} \left(1 + \frac{0.081 f_1}{Fr^2} \right)^{f_2} & \text{if } r_f > 1, \\ \left(1 + \frac{f_3}{Fr(Fr + 2/3 \cdot f_4)} \right)^{-3/2} & \text{if } r_f < 1, \end{cases} \quad (3.3.20)$$

where $f_1 = 1 + 0.88(r_f - 1)$, $f_2 = 1.25(1 - f_1)/f_1$, $f_3 = 0.068(f_1 - 1)$ and $f_4 = 0.12|f_1 - 1 + 1.5/f_1|^{4/9}$. The correction function $f(N, S)$ can in turn be regarded as correction function for the dissipation length in stable stratification,

$$l_\varepsilon = l_\varepsilon^0 \cdot f(N, S). \quad (3.3.21)$$

By that, two correction functions for the dissipation length have been derived which match the interior value from inertial subrange theory (3.3.13) with the correct length scales near the surface via (3.3.17) and near the thermocline⁹ via (3.3.21), respectively.

3.3.4 Algebraisation of the second-order moment equations

In order to get the equations (3.3.1)-(3.3.4) tractable, they are strongly simplified by algebraic stress modeling (Rodi 1976, Canuto 1994). The main purpose is to transform them from differential equations into algebraic relations. Finally only one differential equation is solved numerically, namely that for the SGS turbulent kinetic energy, (3.3.1), while all the others are solved algebraically. The following approximations are made: In the equations (3.3.2)-(3.3.4) the turbulent diffusion terms are entirely neglected. In principle, this corresponds to the assumption of homogeneous turbulence in the unresolved scales. This assumption is less restrictive than the assumption of isotropic turbulence which leads to the Smagorinsky SGS model. Weak inhomogenities are accounted for by including turbulent diffusion terms in the approximation of the equation for the SGS turbulent kinetic energy, (3.3.1).

In (3.3.1), the horizontal part of the turbulent diffusion term $D_f(e)$ is implicitly taken into account by the numerical diffusion of the chosen advection scheme. Since equation (3.3.1) is discretized using the upstream method the numerical diffusion is expected to be larger than $D_f(e)$. The vertical part of $D_f(e)$ is accounted for by a down-gradient formulation following Zeman and Tennekes (1975). The approximated equation is given by (3.3.26).

In (3.3.2), the time-derivative and turbulent diffusion are neglected in order to get the diagnostic expression $\varepsilon_\theta = -\overline{u_i \theta \partial \overline{T}} / \partial x_i$. Introducing the time scale of temperature fluctuations τ_θ by $\tau_\theta = \overline{\theta^2} / \varepsilon_\theta$, the time scale of temperature fluctuations is commonly connected to the turbulent time scale $\tau = 2e/\varepsilon$ by

$$\tau_\theta = \frac{\tau}{c_1}. \quad (3.3.22)$$

Inertial subrange theory predicts $c_1 = 1/2c_\varepsilon \cdot Ba/Ko \approx 0.5$ (Ba , Ko are the Batchelor and the Kolmogorov constant having a value of 1.34 and 1.6, respectively) but this contrasts shear flow experiments by Webster (1964) which indicate that $c_1 \approx 0.7$ (Launder 1976). As the Webster (1964) data will be used for $f(N, S)$ in Chapter 4.4.2, the latter value for c_1 is adopted. Finally, the algebraic expression (3.3.27) is derived. The relation (3.3.22) can in turn be regarded as ratio of the

⁹The correction function $f(N, S)$ is applied anywhere in the flow but it differs from unity only in stably stratified regions.

return-to-isotropy coefficients in (3.3.8) and (3.3.9),

$$C_{\theta 1} = \frac{C_{\Pi 1}}{c_1}. \quad (3.3.23)$$

In (3.3.3), the dimensionless anisotropic part of the Reynolds stress tensor $a_{ij} = b_{ij}/e$ is introduced. Hence, the left hand side of (3.3.3) becomes

$$\frac{Db_{ij}}{Dt} = e \frac{Da_{ij}}{Dt} + a_{ij} \frac{De}{Dt}. \quad (3.3.24)$$

Taken furthermore the approximation $D_f(b_{ij}) \approx \frac{b_{ij}}{e} D_f(e)$ suggested by Rodi (1980) and assuming Da_{ij}/Dt to be small, (3.3.24) together with the diffusion term results in

$$\frac{Db_{ij}}{Dt} + D_f(b_{ij}) = a_{ij} \left(\frac{De}{Dt} + D_f(e) \right) = \frac{b_{ij}}{e} (P_e - \varepsilon) = \frac{2b_{ij}}{\tau} (G - 1), \quad (3.3.25)$$

where $P_e = -b_{ij}S_{ij} + \lambda_k \overline{u_k \theta}$ and ε are the production and dissipation of turbulent kinetic energy, respectively, from (3.3.1) and $G = P_e/\varepsilon$. Thus time derivative and third-order moments are taken as proportional to the corresponding terms in the equation for the turbulent kinetic energy (3.3.1), allowing to get a diagnostic expression for the Reynolds stresses. This procedure is hoped to be a better approximation to the Reynolds stress dynamics than simply neglecting the time derivative and diffusion terms in (3.3.3)¹⁰. Hence, the Reynolds stresses are expressed as composed from non-stationarity contributions arising from shear, buoyancy, and vorticity given in (3.3.28). In (3.3.4), the third-order moments are neglected and local equilibrium is assumed to get an algebraic relation. Not only the contribution of the temperature gradient is retained but also that of temperature fluctuations and anisotropic production by shear (see (3.3.29)).

Equation (3.3.12), connecting dissipation rate of turbulent kinetic energy and dissipation length scale, is modified to account for wall-proximity according to (3.3.16) and for the effects of stratification, shear and rotation on the dissipation length scale by the correction functions $f(N, S)$ according to (3.3.20) and $g(R\theta)$ according to (3.3.14). The approximated equations for the SGS second-order moments and the modified expression for the dissipation rate of turbulent kinetic energy can now be written as follows

$$\frac{De}{Dt} = \nu_e \frac{\partial^2 e}{\partial z^2} - b_{ij}S_{ij} + \lambda_k \overline{u_k \theta} - \varepsilon, \quad (3.3.26)$$

¹⁰ However, there are some deficiencies in this derivation. Firstly, neglecting Da_{ij}/Dt is only appropriate for $\tau \cdot S \geq 1$ (Taulbee, 1992), where S is the shear frequency. This requirement is only met in strong sheared flows in which in turn the assumption of local isotropy becomes questionable. Secondly, the assumption that Reynolds stress diffusion is proportional to diffusion of turbulent kinetic energy implies constant anisotropy of the stress tensor.

$$\overline{\theta^2} = -\frac{\tau}{c_1} \overline{u_k \theta} \frac{\partial \overline{T}}{\partial x_k}, \quad (3.3.27)$$

$$\begin{aligned} \frac{2}{\tau} (c_2 + (G - 1)) b_{ij} &= -c_3 e S_{ij} + c_4 (\lambda_i \overline{w \theta} + \lambda_3 \overline{u_i \theta} \\ &\quad - \frac{2}{3} \delta_{i3} \lambda_k \overline{u_k \theta}) - c_5 (\Sigma_{ij} + Z_{ij}), \end{aligned} \quad (3.3.28)$$

$$\begin{aligned} \frac{2c_6}{\tau} \overline{u_i \theta} &= -(b_{ij} + \frac{2}{3} e \delta_{ij}) \frac{\partial \overline{T}}{\partial x_j} \\ &\quad - c_7 \lambda_3 \delta_{i3} \overline{\theta^2} - c_8 S_{ij} \overline{u_j \theta}, \end{aligned} \quad (3.3.29)$$

$$\varepsilon = \frac{e^{3/2}}{f(N, S) g(Ro) l_\varepsilon}, \quad (3.3.30)$$

where $c_1 = 1.4$, $c_2 = C_{\Pi 1}/2 = 2.38$, $c_3 = 4/3 - C_{\Pi 2} = 0.53$, $c_4 = 1 - C_{\Pi 3} = 0.7$, $c_5 = 1 - C_{\Pi 4} = 0.43$, $c_6 = C_{\theta 1}/2 = 3.75$, $c_7 = 1 - C_{\theta 2} = 0.58$, $c_8 = 1 - C_{\theta 3} = 0.4$.

In summary, the SGS model is composed of one differential equation (for the SGS turbulent kinetic energy). The effects of shear and buoyancy are taken into account via algebraic relations for $\overline{\theta^2}$, b_{ij} and $\overline{u_i \theta}$. The main deficiencies of the Smagorinsky model are removed within this formulation. The assumption of alignment of SGS stresses and the rate of strain tensor is released in the formulation of (3.3.28). Shear and buoyancy terms contribute to both the SGS fluxes of momentum (3.3.28) and of heat (3.3.29). The concept of the turbulent SGS Prandtl number is obsolete since the fluxes of momentum and heat adjust themselves according to the flow conditions. The work turbulence has to do against gravity under stably stratified conditions is accounted for by the correction function $f(N, S)$. The differential equation for the turbulent kinetic energy (3.3.26) accounts for (weak) deviations from local equilibrium. The system (3.3.26)-(3.3.30) is solved in an iterative manner (Chapter 4.4).

3.3.5 Recovering of simpler SGS models

The formulation of the SGS fluxes may be simplified and rewritten in order to compare it with commonly used SGS models.

The down-gradient types of SGS models (this approach is e.g. used by Deardorff (1980) and Mironov et al.(2000)) assume alignment of SGS Reynolds stress tensor and strain rate tensor. All the non-diagonal terms, the temperature fluctuations and the vorticity terms are simply neglected. This results in skipping all terms of (3.3.28) and (3.3.29) apart from the mean gradient, hence

$$\begin{aligned} \frac{2c_2}{\tau} b_{ij} &= -c_3 e S_{ij}, \\ \frac{2c_6}{\tau} \overline{u_i \theta} &= -\frac{2}{3} e \frac{\partial \overline{T}}{\partial x_i} \end{aligned}$$

are the simplified counterparts of (3.3.28) and (3.3.29), respectively. The SGS eddy viscosity and diffusivity then reads as

$$\nu_d = \frac{-b_{ij}}{2S_{ij}} = c_\nu e^{1/2} l_\varepsilon, \quad (3.3.31)$$

$$\chi_d = \frac{-\overline{u_i \theta}}{\partial T / \partial x_i} = c_\chi e^{1/2} l_\varepsilon, \quad (3.3.32)$$

where the suffix 'd' denotes the down-gradient approach. All the model constants are summarized in $c_\nu = c_3/2c_2$ and $c_\chi = 2/3c_6$, respectively.

Within the Smagorinsky approach, the local equilibrium assumption is made additionally. It changes (3.3.26) to

$$\varepsilon = -b_{ij}S_{ij} + \lambda_k \overline{u_k \theta} = -b_{ij}S_{ij}(1 - R_f),$$

where R_f is the flux Richardson number approximated by $R_f = -\sigma_0^{-1} Ri$, Ri is the gradient Richardson number and $\sigma_0 = \nu_d/\chi_d = c_\nu/c_\chi = 3/4 \cdot c_3 c_6 / c_2$ the SGS turbulent Prandtl number under neutral conditions. Hence, using $\varepsilon = e^{3/2}/l_\varepsilon = e^{3/2}/(\Delta/c_\varepsilon)$, thus neglecting the shortening of the dissipation length scale near the surface,

$$\nu_d^{Sm} = c_\nu e^{1/2} l_\varepsilon = (C_S \Delta)^2 \cdot S(1 + \sigma_0^{-1} Ri)^{1/2},$$

where $S = (2S_{ij}S_{ij})^{1/2}$. The result corresponds to (3.2.2). All model constants have been summarized in the Smagorinsky constant C_S where

$$C_S = \left(\frac{c_3}{c_2}\right)^{3/4} K o^{3/2} \frac{3\sqrt{3/2}}{8\pi}$$

shows up to depend on the model coefficients c_3 and c_2 and, in turn, on the model coefficients $C_{\Pi 1}, C_{\Pi 2}$ of the pressure-strain correlation tensor (3.3.8). For the present set of coefficients, $C_S \approx 0.096$. The Kosovic approach (3.2.9) can be recovered from the proposed iterative procedure in Chapter 4.4.2. By inserting the down-gradient estimation $b_{ij}^{(1)}$ from (3.3.31) into the second iteration $b_{ij}^{(2)}$ from (4.4.10), it can be seen that under neutral conditions, assuming inertiality, local equilibrium and neglecting Coriolis contributions,

$$b_{ij}^{(2)} = -c'_{K1} \Delta \left(2e^{1/2} S_{ij} - c'_{K2} \Delta \left(S_{ik} S_{kj} - \frac{1}{3} S_{mn} S_{mn} \delta_{ij} - c'_{K3} (S_{ik} \omega_{kj} - S_{jk} \omega_{ik}) \right) \right),$$

which is of the same structural form as the Kosovic formulation (3.2.9). In the highly simplified formulation here the coefficients have the values $c'_{K1} = c_3/(2 \cdot c_2 c_\varepsilon) \approx 0.13$, $c'_{K2} = 4c_5/(c_2 c_\varepsilon) \approx 1.13$, $c'_{K3} = 2c_5/(c_2 c_\varepsilon) \approx 0.57$ whereas in the Kosovic approach (3.2.9), $c_{K1} = 0.116$, $c_{K2} = 0.823$, $c_{K3} = 0.823$. The coefficients are in reasonable agreement which demonstrates that the Kosovic approach can be regarded as a special case of the present second-order moment model.

3.4 The model equations

After the filter operation described in Chapter 3.1 the conservation equations for ocean momentum in Boussinesq approximation read (e.g. Tritton 1988):

$$\frac{\partial \overline{U}_i}{\partial t} + \frac{\partial(\overline{U}_i \cdot \overline{U}_j)}{\partial x_j} = -\frac{1}{\varrho_0} \frac{\partial \overline{P}^*}{\partial x_i} - 2\epsilon_{ijk} \Omega_j \overline{U}_k - \frac{\partial b_{ij}}{\partial x_j} - \frac{\varrho'}{\varrho_0} g_i, \quad (3.4.1)$$

where \overline{U}_i are the cartesian components of the filtered velocity vector, \overline{P}^* is the nonhydrostatic part of the total mean dynamic pressure, Ω_j are the components of the Earth rotation vector (taken here at $75^\circ N$ geographic latitude), b_{ij} are the components of the anisotropic part of the SGS stress tensor, $\varrho' = \varrho - \varrho_r(z)$ is the reduced density, where ϱ denotes the local density and $\varrho_r(z)$ is the ambient background density and $g_i = (0, 0, g)$ is the Earth's gravity. The pressure term includes the diagonal elements of the subgrid scale stress tensor, i.e. $\overline{P}^* = \overline{P} + \varrho_0 \cdot (2/3 + a_{\alpha\alpha})e$ (see Chapter (4.4.2)).

In the present model there is only one additional conservation equation for scalar properties, namely for heat,

$$\frac{\partial \overline{T}}{\partial t} + \frac{\partial(\overline{U}_j \cdot \overline{T})}{\partial x_j} = -\frac{\partial}{\partial x_j} \overline{u_j \theta}. \quad (3.4.2)$$

The budget equation for the SGS turbulent kinetic energy (equation (3.3.26)) is repeated here for clarity. It reads

$$\frac{\partial e}{\partial t} + \frac{\partial(\overline{U}_j \cdot e)}{\partial x_j} = \nu_e \frac{\partial^2 e}{\partial z^2} - b_{ij} S_{ij} + \lambda_k \overline{u_k \theta} - \varepsilon.$$

Chapter 4

Implementation

The effective filter operation which had transformed the basic unfiltered equations into the LES equations is not known in detail. It is an interplay of the representation on the numerical grid with the numerical algorithms and the SGS model. The effective filter can therefore only be deduced *a posteriori* and it is common practice to use the same initial and boundary conditions as for the unfiltered equations (Sagaut 2001). For the sake of simplicity, the overbars indicating the LES filtering process will be omitted from now on.

The implementation Chapter starts with the discussion of appropriate initial and boundary conditions. Section 4.2 is devoted to the numerical algorithms used to integrate the LES equations. A closer look on the numerical formulation of the SGS model is undertaken in Section 4.3. Suitable initial conditions are considered in Section 4.4.

4.1 Initial Conditions

With respect to initial conditions, i.e. for a model 'spin-up', the one-dimensional Ekman dynamics according to equation (2.1.1) together with the eddy viscosity approach (2.1.2) is prescribed. The equations are integrated by a forward-in-time-centered-in-space (FCTS) method until a quasi-stationary state is reached. It has been shown by Svensson (1979) that the constant eddy viscosity

$$\nu_t = 0.026 \frac{u_*^2}{f_z} \quad (4.1.1)$$

yields nearly identical results to more sophisticated turbulence parameterisations. The resulting one-dimensional velocity profiles are stored as initial values for the three-dimensional simulations.

As an example, the integrated profiles of the run 'strong' (see Chapter 6) are shown in figure along with the corresponding analytical solutions according to (2.1.4). While the agreement for the v -component (in blue) is satisfactory the

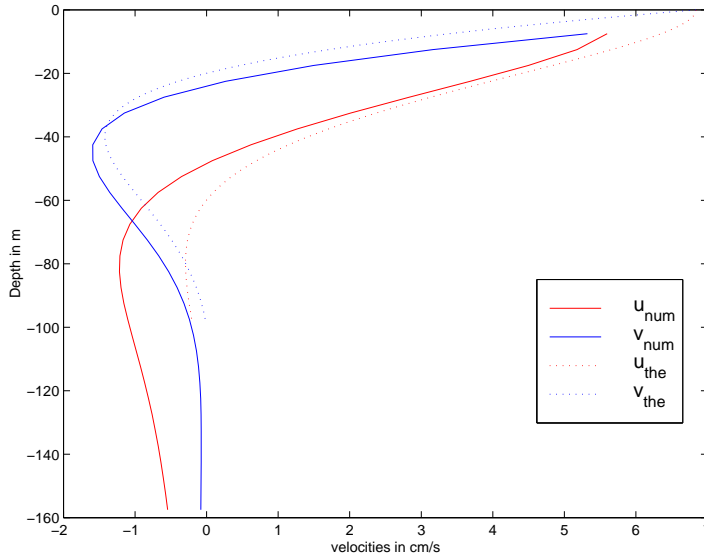


Figure 4.1: The horizontal velocity components from the numerical integration of the Ekman layer equations u_{num} (solid red line) and v_{num} (solid blue line) for run 'strong' in comparison with the theoretical results u_{the} (dotted red line) and v_{the} (dotted blue line) according to (2.1.4).

u -component (red line) significantly differs from the theoretical profiles. The result is due to the fact that the wind was chosen in the y -direction and thus, the boundary condition for u according to (2.1.3) was zero. For too coarse resolution the transfer of momentum from v to u is underpredicted. This deficit can only be overcome by very fine vertical resolution¹.

The initial values for the turbulent kinetic energy are derived from the simplified equation (3.3.32) via

$$e^{init} = \left(\frac{\nu_t}{c_\nu l_\varepsilon} \right)^2.$$

4.2 Boundary Conditions

The surface heat flux \mathcal{H}_0 is gained from a balance equation for the sum of long-wave radiation, sensible and latent heat fluxes in the form

$$\mathcal{H}_0 = \Delta\mathcal{H}_{LW} + \mathcal{H}_{sens} + \mathcal{H}_{lat}. \quad (4.2.1)$$

While short-wave radiation can be omitted in winter time at a latitude of 75° (Smith et al., 1990), the difference of in- and outgoing long-wave radiation is

¹Alternatively, a kind of 'wall function' is currently under investigation in order to bridge the first grid point.

given by Boltzmann's law:

$$\Delta\mathcal{H}_{LW} = \epsilon_{air}\sigma_{SB} \left(T_{air}^4 - T_{sea}^4\right), \quad (4.2.2)$$

where $\epsilon_{air} \approx 0.97$ (Harms, 1994) is the transmission coefficient, σ_{SB} is the Stefan-Boltzmann constant, T_{air} is the air temperature and T_{sea} is the sea surface temperature. Sensible heat fluxes are computed from

$$\mathcal{H}_{sens} = \beta_{sens}\varrho_{air}c_{P,air}|W_{10}|(T_{air} - T_{sea}). \quad (4.2.3)$$

The turbulent exchange coefficient for sensible heat $\beta_{sens} \approx 1.5 \cdot 10^{-3}$ is chosen following Maykut (1986). Thereby, $c_{P,air}$ is the specific heat of air at constant pressure. The latent heat flux

$$\mathcal{H}_{lat} = \beta_{lat}\varrho_{air}L_{vap}|W_{10}|(q_{air} - q_0) \quad (4.2.4)$$

is determined by the turbulent exchange coefficient for latent heat β_{lat} , taken as equal to the exchange coefficient for sensible heat. Thereby, L_{vap} denotes the latent heat of vaporisation, q_{air} is the constant ambient humidity and q_0 is the humidity close to the sea surface which depend on the actual temperature. The kinematic heat flux will be used for the bulk formula (4.2.9). It is related to the dynamic heat flux and the buoyancy flux (see (1.0.2)) via

$$Q_0 = \frac{\mathcal{H}_0}{c_P\varrho_0} = -\frac{B_0}{g\alpha}. \quad (4.2.5)$$

At the surface, the rigid-lid condition $w = 0$ at $z = 0$ is employed. As surface waves are thus excluded, neither wave breaking nor Langmuir circulation can be described.

However, the importance of surface gravity waves is largely reduced in polar boundary layers compared to midlatitude or tropical regions. Waves are likely to be damped in arctic leads and polynyas by ice floes or growing frazil ice (Martin and Kaufmann 1981). It should be kept in mind that the common rigid-lid approximation based on the hydrostatic approximation does not apply here. Instead, it should be viewed as an observational finding that surface displacements are small. The surface fluxes of momentum and heat are prescribed by atmospheric input. From constant wind and temperature fields, surface fluxes are computed using bulk formulae (Gill 1982). The surface stress tensor $\vec{\tau}_0$ is determined from

$$\vec{\tau}_0 = \varrho_{air}C_D \cdot \left(\vec{W}_{10} - \vec{U}_{1,j,k}\right) |\vec{W}_{10} - \vec{U}_{1,j,k}|, \quad (4.2.6)$$

where ϱ_{air} is the mean density of air, C_D is the drag coefficient, \vec{W}_{10} is the wind vector taken at 10 meters height and $\vec{U}_{1,j,k}$ is the surface current vector with grid indices 1, j and k for the vertical, meridional and zonal direction, respectively. For the sake of simplicity, the drag coefficient was chosen to be

constant throughout the test cases at a value of $C_D = 1.0 \cdot 10^{-3}$. This value is at the lower bound of the available estimations (Harms, private commun.). Thus, it tends to *underestimate* the momentum flux associated with a given wind speed. Measurements and theoretical arguments suggest that the drag coefficient may be a good indicator of wind-wave interactions (Kraus and Businger 1994). Therefore, it appears possible to extend the present formulation of the boundary conditions to a free surface flow using empirical laws for the drag coefficient (Smith 1988, Kraus and Businger 1994) accounting for fetch and stability effects. Since from the bulk formula (4.2.6) the surface stress is known, the velocity gradient can be prescribed:

$$\begin{aligned} \frac{\partial U}{\partial z} &= \frac{\tau_0^{(x)}}{\rho_0 \nu_*} & \text{at } z = 0, \\ \frac{\partial V}{\partial z} &= \frac{\tau_0^{(y)}}{\rho_0 \nu_*} & \text{at } z = 0, \end{aligned} \quad (4.2.7)$$

where ν_* denotes the horizontally isotropic vertical eddy viscosity near the surface. The actual value of ν_* is unknown and will be discussed below.

Additionally, the following relations hold at the surface:

$$w = \frac{\partial P}{\partial z} = \frac{\partial e}{\partial z} = 0 \quad \text{at } z = 0, \quad (4.2.8)$$

$$\frac{\partial T}{\partial z} = -\frac{Q_0}{\chi_*} \quad \text{at } z = 0, \quad (4.2.9)$$

where χ_* the vertical eddy diffusivity near the surface. Eddy diffusivity and eddy viscosity are related by the turbulent Prandtl number. Its value has to be specified at the surface according to equation (4.4.6). Corresponding to the Neumann boundary condition for pressure, the density term is prescribed as zero resulting in a balance of pressure gradient and buoyancy at the surface.

The boundary condition for temperature - and that for horizontal velocities (4.2.7) - require closer inspection. The surface fluxes of momentum and heat are explicitly known from the bulk formulae (4.2.6) and (4.2.5), respectively. Thus, gradients of the mean velocity and temperature can be directly linked to the surface fluxes. As both of them are similar in structure, only the temperature boundary condition is considered in detail. It is Fourier's law with the molecular diffusivity for heat replaced by an eddy diffusivity. The first implication of the Fourier law due to the parabolic character of the heat conduction equation is an infinitely fast spreading velocity. Fourier's law implies the assumption that the surface fluxes (4.2.7), (4.2.9) apply instantaneously. This is confirmed by observations in which records of current changes closely followed pronounced changes of the surface wind (Kraus und Businger 1994). The second more severe point is the determination of eddy diffusivity (and eddy viscosity, respectively). Fortunately, due to the explicit time integration of the turbulent diffusion, the exact value is of

no importance. It cancels out during the computation (demonstrated in Chapter 4.4.3) and is therefore taken as a constant.

The following relations hold at the lower boundary:

$$\begin{aligned} \frac{\partial P}{\partial z} = \frac{\partial T}{\partial z} = \frac{\partial e}{\partial z} = 0 & \quad \text{at} \quad z = -L_z, \\ u = v = w = 0 & \quad \text{at} \quad z = -L_z. \end{aligned} \quad (4.2.10)$$

To avoid reflecting internal gravity waves, a Rayleigh damping function is applied to the lower 1/4 of the model domain where the horizontal components of the SGS eddy viscosity and eddy viscosity tensors (4.4.1) are increased according to

$$\nu_{ij}^{(new)} = \nu_{ij}^{(old)} + \nu_{damp}, \quad (4.2.11)$$

for $I \geq 3/4 \cdot NZ$, where I is the vertical layer index and NZ the total number of vertical layers. The damping value is taken as

$$\nu_{damp} = \nu_{damp,0} \cdot \sin^2 \left(\pi/2 \cdot \frac{I - 3/4 \cdot NZ}{1/4 \cdot NZ} \right),$$

with $\nu_{damp,0} = 0.1 m s^{-1}$.

The requirement for the horizontal boundary conditions is that the model domain is chosen sufficiently large such that the flow is not affected by the boundaries. The horizontal conditions therefore satisfy periodicity where flow out of a horizontal boundary enters the opposite boundary. The requirement will be discussed in the model set up (Chapter 5).

4.3 Numerical Algorithms

The equations are discretized as finite differences on a staggered C-grid (Mesinger and Arakawa 1976). Scalar mean quantities are located in the mid-cell, the vertical velocity component at the top wall of the cell and the horizontal velocity components at the side walls corresponding to their respective directions. The turbulent kinetic energy is located at the top wall. The totally six components of the SGS eddy viscosity and diffusivity tensors $\nu_k, \chi_k (k = 1, 2, 3)$, see equation (4.4.1), are located differently. Figure 4.2 displays the numerical grid in the horizontal direction. The numerical grid in vertical direction is shown in Figure 4.3.

The discretization of the momentum equations is done by a TVD flux-limited modified MacCormack scheme (MacCormack 1969). Originally, it combines forward differencing in the first step with backward differencing in the second step to achieve second order accuracy in space and time. For the use in a flux-limited advection algorithm, the steps are slightly modified.

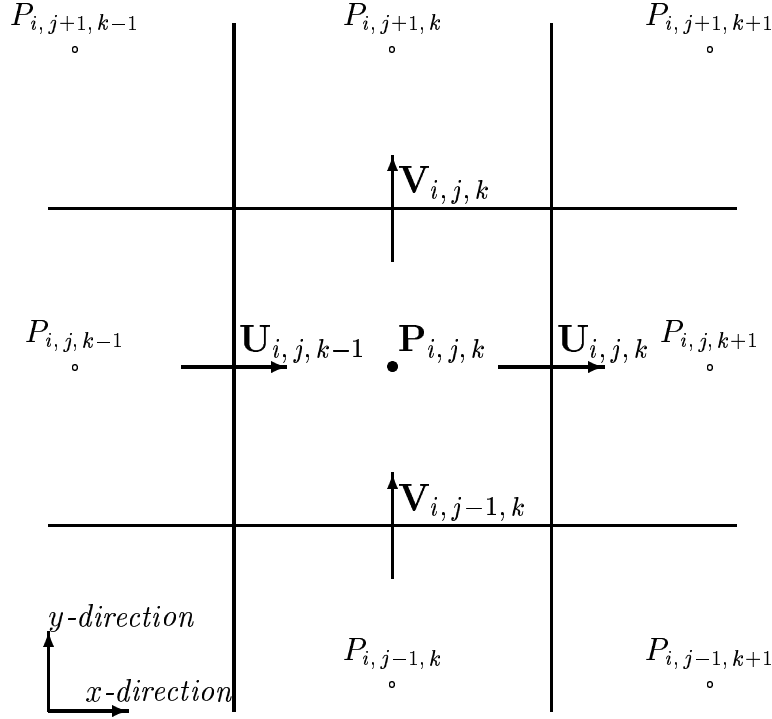


Figure 4.2: The Arakawa C Grid in *horizontal* direction

The mean flow scalar variables P and T are located in the middle of the cell while the horizontal velocity components U and V are located at the corresponding cell boundaries. The grid indices j and k refer to the meridional and the zonal direction, respectively. The horizontal components of the SGS eddy viscosity and diffusivity tensors, ν_1, χ_1, χ_2 , from (4.4.1), are located in the middle of the cell as well.

To simplify the presentation, regard a two-dimensional advection equation of velocity u with source term $q(u)^2$:

$$\frac{\partial u}{\partial t} = - \left(\frac{\partial f(u)}{\partial x} + \frac{\partial g(u, v)}{\partial y} \right) + q(u), \quad (4.3.1)$$

where $f(u) = u^2, g(u, v) = u \cdot v$ are the flux functions. With respect to the following discussion the numerical approximation is written in conservation form,

$$\begin{aligned} U_{j,k}^{n+1} = U_{j,k}^n & - \frac{\Delta t}{\Delta x} \cdot (F_{j,k+1/2} - F_{j,k-1/2}) \\ & - \frac{\Delta t}{\Delta y} \cdot (G_{j+1/2,k} - G_{j-1/2,k}) + \Delta t \cdot Q_{j,k}, \end{aligned} \quad (4.3.2)$$

where U, F, G and Q denote the numerical approximations to velocity u , flux functions f, g and source term q , and j, k are the grid indices in x - and y -direction,

²The term $q(u)$ contains diffusion, rotation and pressure-gradient in the model equations.

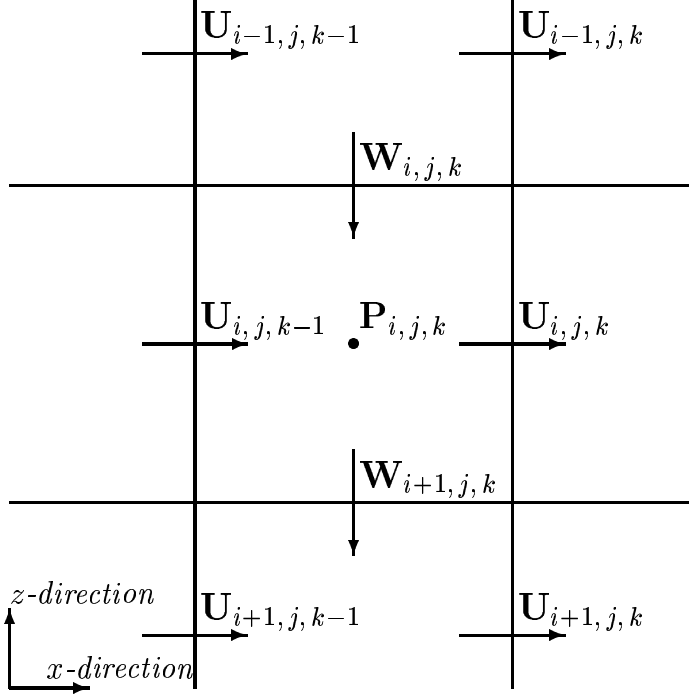


Figure 4.3: The Arakawa C Grid in *vertical* direction.

The vertical velocity component W is staggered by half a vertical grid size compared to the other mean flow variables. The grid index i and k refers to the vertical direction. The SGS turbulent kinetic energy e is located on the W -point. The same is true for the vertical components of the SGS eddy viscosity and diffusivity tensors, ν_2, ν_3, χ_3 , from (4.4.1).

respectively. Skipping the source term for a moment, methods which can be written in this form are guaranteed to converge to a weak solution of the original equation (4.3.1) (as long as they are convergent and consistent). The numerical flux functions F, G can be viewed as approximating the flux functions f, g averaged over the time step. The predictor step of the modified MacCormack algorithm is an upstream approximation,

$$U_{j,k}^{(1)} = U_{j,k}^n - \Delta t \cdot \left(\frac{F_{j,k+1/2}^{up} - F_{j,k-1/2}^{up}}{\Delta x} + \frac{G_{j+1/2,k}^{up} - G_{j-1/2,k}^{up}}{\Delta y} - Q_{j,k} \right), \quad (4.3.3)$$

where

$$\begin{aligned} F_{j,k+1/2}^{up} &= \frac{U_{j,k+1/2}^n + |U_{j,k+1/2}^n|}{2} U_{j,k}^n + \frac{U_{j,k+1/2}^n - |U_{j,k+1/2}^n|}{2} U_{j,k+1}^n, \\ G_{j+1/2,k}^{up} &= \frac{V_{j+1/2,k}^n + |V_{j+1/2,k}^n|}{2} U_{j,k}^n + \frac{V_{j+1/2,k}^n - |V_{j+1/2,k}^n|}{2} U_{j+1,k}^n \end{aligned}$$

are the upstream flux functions in x - and y -direction, respectively, and velocities $U_{j,k+1/2}^n, V_{j+1/2,k}^n$ derived from the Rankine-Hugenot jump condition (Sweby

1984).

In the corrector step, antidiffusive downstream fluxes are added in each direction to correct the upstream predictor step. In order to avoid oscillations, the corrector fluxes are limited by so-called flux limiters $\phi^{(x)}, \phi^{(y)}$. The corrector step has the structure

$$\begin{aligned} U_{j,k}^{(2)} &= U_{j,k}^{(1)} - \frac{\Delta t}{2} \left(\frac{F_{j,k+1/2}^C - F_{j,k-1/2}^C}{\Delta x} + \frac{G_{j+1/2,k}^C - G_{j-1/2,k}^C}{\Delta y} \right) \\ &\quad + \frac{\Delta t}{2} (Q_{j,k}^{(1)} - Q_{j,k}^n), \end{aligned} \quad (4.3.4)$$

where F^C, G^C denote the corrected fluxes,

$$\begin{aligned} F_{j,k+1/2}^C &= \phi_{j,k+1/2}^{(x)} \cdot \left(\frac{U_{j,k+1/2}^{(1)} + |U_{j,k+1/2}^{(1)}|}{2} U_{j,k+1}^{(1)} + \frac{U_{j,k+1/2}^{(1)} - |U_{j,k+1/2}^{(1)}|}{2} U_{j,k}^{(1)} \right), \\ G_{j+1/2,k}^C &= \phi_{j+1/2,k}^{(y)} \cdot \left(\frac{V_{j+1/2,k}^{(1)} + |V_{j+1/2,k}^{(1)}|}{2} U_{j+1,k}^{(1)} + \frac{V_{j+1/2,k}^{(1)} - |V_{j+1/2,k}^{(1)}|}{2} U_{j,k}^{(1)} \right). \end{aligned}$$

The flux-limiters $\phi^{(x)}, \phi^{(y)}$ are chosen to enforce the TVD property to the solution. Their derivation is given in the Appendix.

The solution is denoted $U^{(2)}$ instead of U^{n+1} since it is not divergence-free. Now $U^{(2)}$, containing the modified pressure field P^* of the previous time step³, is used to compute the actual pressure implicitly in order to guarantee conservation of mass. This is done implicitly by correcting the velocity field according to

$$U^{n+1} = U^{(2)} - \frac{\Delta t}{\rho_0} \frac{\partial(P^{n+1} - P^*)}{\partial x}. \quad (4.3.5)$$

Using the one-dimensional continuity equation $\partial U^{n+1} / \partial x = 0$, this expression yields a Poisson equation for the pressure update

$$\frac{\partial^2}{\partial x^2} (P^{n+1} - P^*) = \frac{\rho_0}{\Delta t} \frac{\partial U^{(2)}}{\partial x}. \quad (4.3.6)$$

The pressure equation is solved by a successive overrelaxation (SOR) iteration (e.g. Meister 1999).

The heat equation is approximated by a flux-limited, modified two-step Lax-Wendroff scheme which is in close analogy to the MacCormack scheme. The only difference lies in the use of the advection velocity U^n which is identical in the predictor and the corrector step of temperature advection. This fact would in principle allow to compute the solution within a single step. However, the two-step procedure implicitly contains fourth-order derivatives which are effectively

³The old pressure includes the normal stress components $\overline{u_\alpha^2}$.

in damping high-wave number noise. The conservation equation for heat and the constant salinity (34psu) are linked to the momentum equations by the nonlinear equation of state (UNESCO, 1981). As the study deals with shallow convection the pressure dependence of the equation of state (*thermobaric effect*) is neglected. The approximated budget equation for the SGS turbulent kinetic energy e , (3.3.26), is treated by the upstream method. In order to guarantee the positivity of e and ε the sink term ε is computed by the quasi-implicit treatment proposed by Patankar (1980).

The time step of the convection model is chosen as 30s. It is neither limited by the stability criterion for the explicit TVD advection scheme (CFL number) nor by stability criterion for the centered-in-space diffusion scheme. The limiting factor was found to be the pressure equation. During the penetration of sinking plumes into the stably stratified layer below, fast-travelling internal waves are radiated which require high temporal resolution.

4.4 The SGS model algorithm

As the system of equations (3.3.26)-(3.3.30) describing subgrid-scale second-order moments is nonlinear despite of the algebraisation procedure, it cannot be solved explicitly. In this Chapter a short explanation is given how the simplified equations are stored and solved iteratively in the LES model.

4.4.1 Storage procedure

The coupling of mean and SGS flow is given by (compare with equations (3.4.1) and (3.4.2)) the following expressions in which the SGS contribution have been isolated on the right-hand side,

$$\begin{aligned} \frac{\partial U}{\partial t} + \frac{\partial(U \cdot U_j)}{\partial x_j} + \frac{1}{\rho_0} \frac{\partial P^*}{\partial x} + 2\epsilon_{1jk}\Omega_j U_k &= - \left(\frac{\partial(b_{11} + 2e/3)}{\partial x} + \frac{\partial b_{12}}{\partial y} + \frac{\partial b_{13}}{\partial z} \right), \\ \frac{\partial V}{\partial t} + \frac{\partial(V \cdot U_j)}{\partial x_j} + \frac{1}{\rho_0} \frac{\partial P^*}{\partial y} + 2\epsilon_{2jk}\Omega_j U_k &= - \left(\frac{\partial b_{12}}{\partial x} + \frac{\partial(b_{22} + 2e/3)}{\partial y} + \frac{\partial b_{23}}{\partial z} \right), \\ \frac{\partial W}{\partial t} + \frac{\partial(W \cdot U_j)}{\partial x_j} + \frac{1}{\rho_0} \frac{\partial P^*}{\partial z} + 2\epsilon_{3jk}\Omega_j U_k &= - \left(\frac{\partial b_{13}}{\partial x} + \frac{\partial b_{23}}{\partial y} + \frac{\partial(b_{33} + 2e/3)}{\partial z} \right), \\ \frac{\partial T}{\partial t} + \frac{\partial(U_j \cdot T)}{\partial x_j} &= - \left(\frac{\partial \overline{u\theta}}{\partial x} + \frac{\partial \overline{v\theta}}{\partial y} + \frac{\partial \overline{w\theta}}{\partial z} \right). \end{aligned}$$

Within the computation both the SGS Reynolds stress and the heat flux tensors are related to the strain rate and temperature gradient tensors via the quasi-tensors of eddy viscosity and eddy diffusivity, respectively⁴. These quasi-tensors

⁴The turbulence model is still an eddy viscosity diffusion approach but a tensorial one. The diffusion approach induces a parabolic behavior of the turbulent fluxes whereas it might be

are written in a way that they finally contain three elements only. Each element is related to a three-dimensional array. Consequently, the quasi-tensors are stored in six three-dimensional arrays.

The quasi-viscous laws $b_{ij} = -2\nu_{ijkl}S_{ij}$ and $\overline{u_i\theta} = -\chi_{ijkl}\partial T/\partial x_i$ can be simplified as all tensors are symmetric, e.g. $b_{ij} = b_{ji}$ and the diagonal terms are treated separately. Rewriting the traceless part of the Reynolds stress tensor and the heat flux tensor in vector form, the eddy viscosity and diffusivity quasi-tensors are defined by

$$\begin{pmatrix} b_{12} \\ b_{13} \\ b_{23} \end{pmatrix} = -2 \begin{pmatrix} \nu_1 & 0 & 0 \\ 0 & \nu_2 & 0 \\ 0 & 0 & \nu_3 \end{pmatrix} \cdot \begin{pmatrix} S_{12} \\ S_{13} \\ S_{23} \end{pmatrix},$$

$$\begin{pmatrix} \overline{u\theta} \\ \overline{v\theta} \\ \overline{w\theta} \end{pmatrix} = - \begin{pmatrix} \chi_1 & 0 & 0 \\ 0 & \chi_2 & 0 \\ 0 & 0 & \chi_3 \end{pmatrix} \cdot \begin{pmatrix} \partial T/\partial x \\ \partial T/\partial y \\ \partial T/\partial z \end{pmatrix}. \quad (4.4.1)$$

As can be seen there are only three elements in the SGS eddy viscosity and diffusivity quasi-tensors, respectively, which are computed by

$$\begin{aligned} \nu_k &= -\frac{b_{\alpha\beta}}{2S_{\alpha\beta}}, \\ \chi_k &= -\frac{\overline{u_\alpha\theta}}{\partial T/\partial x_\alpha} \end{aligned} \quad (4.4.2)$$

where $k = 1, 2, 3$. The six three-dimensional fields ν_k and χ_k ($k = 1, 2, 3$) have to be stored which is equivalent with storing the arrays of the six SGS fluxes $b_{12}, b_{13}, b_{23}, \overline{u\theta}, \overline{v\theta}$ and $\overline{w\theta}$.

Additionally there are three normal components of the SGS Reynold stress tensor $\overline{u_\alpha^2} = b_{\alpha\alpha} + 2/3 \cdot e$ with $\alpha = 1, 2, 3$. The components $b_{\alpha\alpha}$ are given by contraction of (3.3.28) and the additional condition that $b_{ii} = 0$, i.e. the tensor of anisotropic SGS Reynolds stresses is traceless. The SGS turbulence is assumed to be anisotropic only in the first two model layers and to relax to an isotropic state in the interior. Consequently, the anisotropic parts $b_{\alpha\alpha}$ of the normal stress components $\overline{u_\alpha^2}$ are only stored in the first two model layers. They are assumed to be negligible further away from the surface where $\overline{u_\alpha^2} \approx 2/3 \cdot e$. Note that during the iterative computation of the tangential stress and the heat flux components ((4.4.10), (4.4.12)), the anisotropic normal stress components $b_{\alpha\alpha}$ are taken into account. They are only neglected apart from the first two model layers in the determination of the modified pressure P^* (see footnote 3 in this Chapter).

equally reasonable to assume a hyperbolic behavior.

4.4.2 Iterative computation

The notation of the constants is the same as in (3.3.26)-(3.3.30) and the same as in the source coding as well.

- The SGS turbulent kinetic energy e is given at the old time level (e^n).
- The dissipation length scale l_ε^{n+1} is taken as $f(N, S)g(Rb) \cdot \Delta/c_\varepsilon$, where $c_\varepsilon = 0.85$, Δ is the grid size, $f(N, S)$ is the correcture function given by (3.3.20), and $g(Rb)$ is the correction function given by (3.3.14). With respect to the computation of $f(N, S)$ the flux Richardson number R_f is needed. As R_f is not yet known at this stage, it is replaced by an expression containing the actual available gradient Richardson number $Ri = N^2/S^2$ and an estimation of the SGS Prandtl number σ , which is itself a function of the Richardson number,

$$R_f = -\sigma^{-1}(Ri) \cdot Ri, \quad (4.4.3)$$

where $\sigma(Ri)$ is fitted from experimental data (Webster, 1964) resulting in

$$\frac{\sigma(Ri)}{\sigma_0} \approx 1 + 1.6Ri + 2Ri^2. \quad (4.4.4)$$

The dissipation length scale is now available and the dissipation can be computed from (3.3.12) :

$$\varepsilon^{n+1} = \frac{(e^n)^{3/2}}{l_\varepsilon^{n+1}}. \quad (4.4.5)$$

It is in this step and in the computation of the surface boundary (4.2.9) that an estimation for σ_0 , the SGS turbulent Prandtl number under neutral conditions is required. From equation (3.3.32) the following estimation is available:

$$\sigma_0 = \frac{3c_3c_6}{4c_2} \approx 0.63. \quad (4.4.6)$$

Unfortunately, this value is seen to depend on the coefficients from the model of the pressure-gradient correlation tensors.

- A first estimation for the Reynolds stresses b_{ij}^{n+1} is made with the aid of the eddy viscosity at the previous time step. The preliminary Reynolds stress reads

$$b_{\alpha\beta}^{(1)} = -2\nu_k^n \cdot S_{\alpha\beta}^n, \quad (4.4.7)$$

where greek symbols indicate that there is no index summation. Additionally, $\alpha \neq \beta$.

- The temperature fluctuation is estimated as

$$\overline{\theta^2}^{(1)} = \frac{\tau^2}{2c_1c_6} \left(\frac{2e}{3} \left(\frac{\partial T}{\partial z} \right)^2 + 2b_{ij}^{(1)}(1 - \delta_{ij}) \left(\frac{\partial T}{\partial x_i} \right) \left(\frac{\partial T}{\partial x_j} \right) \right). \quad (4.4.8)$$

- The provisional heat flux $\overline{u_i\theta}$ is determined by

$$\overline{u_i\theta}^{(1)} = -\frac{\tau}{2c_6} (b_{ij}^{(1)} + \frac{2}{3}e^n\delta_{ij}) \frac{\partial T^n}{\partial x_j} + \frac{c_7}{2c_6} \tau \lambda_3 \delta_{i3} \overline{\theta^2}^{(1)}. \quad (4.4.9)$$

- Using (4.4.9), the Reynolds stresses are corrected as

$$b_{ij}^{(2)} = pp_5 \left(-c_3 e^n S_{ij}^n + c_4 (\lambda_i \overline{u_j\theta} + \lambda_j \overline{u_i\theta} - \frac{2}{3} \lambda_k \overline{u_k\theta}) - c_5 (\Sigma_{ij}^{(1)} + Z_{ij}^{(1)}) \right), \quad (4.4.10)$$

where

$$\begin{aligned} pp_5 &= \frac{\tau}{2c_2 + 2 \left(\frac{P^{(1)}}{\varepsilon} - 1 \right)}, \\ P^{(1)} &= -b_{ij}^{(1)} S_{ij} + \lambda_k \overline{u_k\theta}, \\ \Sigma_{ij}^{(1)} &= S_{ik} b_{kj}^{(1)} + S_{jk} b_{ik}^{(1)} - \frac{2}{3} \delta_{ij} S_{kl} b_{kl}^{(1)}, \\ Z_{ij}^{(1)} &= b_{ik}^{(1)} \omega_{jk} + b_{jk}^{(1)} \omega_{ik} + c_9 (\epsilon_{jkl} b_{ik}^{(1)} + \epsilon_{ikl} b_{jk}^{(1)}) \Omega_l. \end{aligned}$$

- The temperature fluctuation is updated to

$$\overline{\theta^2}^{(2)} = -\frac{\tau}{c_1} \overline{u_k\theta}^{(1)} \left(\frac{\partial T}{\partial x_k} \right). \quad (4.4.11)$$

- The new heat flux reads as

$$\overline{u_i\theta}^{(2)} = -\frac{\tau}{2c_6} (b_{ij}^{(2)} + \frac{2}{3}e^n\delta_{ij}) \frac{\partial T^n}{\partial x_j} + \frac{c_7}{2c_6} \tau \lambda_3 \delta_{i3} \overline{\theta^2}^{(2)}. \quad (4.4.12)$$

- The iteration procedure (4.4.10)-(4.4.12) is repeated two times.
- The eddy viscosity and diffusivity components are computed in the form

$$\begin{aligned} \nu_k &= -\frac{b_{\alpha\beta}}{2S_{\alpha\beta}}, \\ \chi_k &= -\frac{\overline{u_\alpha\theta}}{\partial T / \partial x_\alpha}, k = 1, 2, 3, \alpha \neq \beta. \end{aligned} \quad (4.4.13)$$

These values are used in the approximations for momentum and temperature to compute the eddy diffusion terms.

- The anisotropic normal stress components are only stored in the first two layers, see Chapter 4.4.1,

$$a_{\alpha\alpha} = \frac{b_{\alpha\alpha}}{e}. \quad (4.4.14)$$

In the first two layers, these values are added to the modified pressure to give $P^* = P^n + \varrho_0(2/3 + a_{\alpha\alpha})e$ (see Chapter 4.3).

- Finally, the e -equation is solved by the discrete approximation of (3.3.26).

4.4.3 Numerical considerations of the SGS model

In order to keep the numerical model stable it is required to specify minimum and maximum values of the SGS fields.

Unfortunately, numerical stability requires the eddy viscosity and diffusivity to be positive. From a physical point of view, they might become negative representing a backscatter of energy towards the resolved scales. Whereas on average the energy cascade is in the forward direction, backscattering is known to occur intermittently. In the present model the appearance of physically possible negative viscosity and diffusivity is suppressed by prescribing a minimum value of $\nu_{min} = 1 \cdot 10^{-5} m^2 s^{-1}$. Especially the process of 'counter-gradient fluxes' (e.g., Deardorff 1974) during penetrative convection cannot be captured by the present SGS formulation. The maximum value of the vertical eddy viscosity and diffusivity components (ν_2, ν_3, χ_3) is given by $0.15 m^2 s^{-1}$ whereas the horizontal components (ν_1, χ_1, χ_2) are limited by $1 m^2 s^{-1}$. One (among others) of the limiting factors is numerical stability of the centered-in-space diffusion scheme.

A further remark is required concerning the numerical discretization of the first model layer. For computing the boundary conditions (4.2.7) and (4.2.9) there are auxiliary grid points $U_{0,j,k}, V_{0,j,k}, T_{0,j,k}$. They are located half a vertical grid size outside the grid domain corresponding to the vertical grid index $i = 0$ (see Figure 4.4) such that

$$\begin{aligned} U_{0,j,k} &= U_{1,j,k} + \Delta z \cdot \frac{\partial U}{\partial z} = U_{1,j,k} + \Delta z \cdot \frac{\tau_0^{(x)}}{\varrho_0 \nu_*}, \\ V_{0,j,k} &= V_{1,j,k} + \Delta z \cdot \frac{\partial U}{\partial z} = V_{1,j,k} + \Delta z \cdot \frac{\tau_0^{(y)}}{\varrho_0 \nu_*}, \\ T_{0,j,k} &= T_{1,j,k} + \Delta z \cdot \frac{\partial T}{\partial z} = T_{1,j,k} - \Delta z \cdot \frac{Q_0}{\chi_*}. \end{aligned}$$

The values $U_{0,j,k}, V_{0,j,k}, T_{0,j,k}$ are computed in order to give the correct boundary fluxes at $z = 0$ which is the top of the model domain where all fluxes enter through SGS turbulent diffusion. At the boundary, the resolved fluxes are zero due to the boundary condition $w = 0$. It has been mentioned above that the

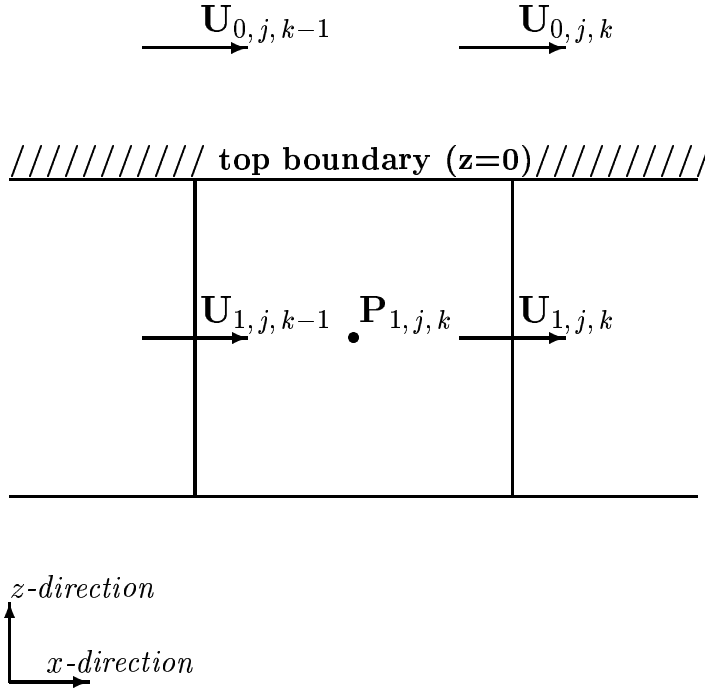


Figure 4.4: The auxiliary grid points U_0 are located half a vertical grid size outside the model domain. The correct surface flux is given by the central difference $(U_{0,j,k} - U_{1,j,k})/\Delta z$. Analogously for the V -component and the temperature field.

exact value of the surface eddy viscosity ν_* is of no importance since it cancels out during computation. This can be seen as follows. The vertical diffusion of velocity $U_{1,j,k}$ is given by

$$\begin{aligned} \frac{\partial}{\partial z} \left(\nu_2 \frac{\partial U}{\partial z} \right)_{(1,j,k)} &= \frac{1}{\Delta z^2} \left(\nu_* (U_{0,j,k} - U_{1,j,k}) - \nu_{2,(3/2,j,k)} (U_{1,j,k} - U_{2,j,k}) \right) \\ &= \frac{1}{\Delta z^2} \left(\nu_* \frac{\tau_0^{(x)}}{\varrho_0 \nu_*} - \nu_{2,(3/2,j,k)} (U_{1,j,k} - U_{2,j,k}) \right). \end{aligned}$$

Here the notation $\nu_{2,(3/2,j,k)}$ refers to the eddy viscosity ν_2 inbetween the points $(1, j, k)$ and $(2, j, k)$ and ν_* is located inbetween the points $(0, j, k)$ and $(1, j, k)$. It is visible that ν_* cancels out. It has just been required to define $U_{0,j,k}$ as sum of $U_{1,j,k}$ and shear stress contribution. Any other choice of ν_* would have only changed $U_{0,j,k}$ but not the term $\nu_* (U_{0,j,k} - U_{1,j,k})$ which appears in the diffusion equation.

Unfortunately, the employed TVD advection schemes are relatively diffusive as will be shown in Chapter 7. The reason for using TVD Lax-Wendroff schemes⁵

⁵The MacCormack scheme is simply a nonlinear formulation of the Lax-Wendroff scheme.

instead of more sophisticated formulations is the following. The coefficient of numerical diffusion of the TVD Lax-Wendroff scheme is proportional to the flow velocity (LeVeque 1992). Therefore, numerical diffusion is large only in horizontal directions where the near-surface velocities are several cm/s . This is relatively uncritical for the prediction of the convective flow as the physical eddy viscosity and diffusivity in horizontal directions are larger in general. It has been shown in the introductory Chapter that LES of convective flows mainly suffer from the inability of the SGS models to predict the near-wall flow correctly. The vertical turbulence structure is hardly influenced by the vertical numerical diffusivity. Its effect is negligible simply because due to the small vertical (wall-normal) velocity the coefficient of vertical numerical diffusion is small accordingly. That is only true for the near-surface flow. In greater depths, the vertical velocity becomes larger, thus the numerical induced diffusion will grow.

Chapter 5

Bulk modeling of penetrative convection

5.1 Introduction

The bulk model of Zilitinkevich (1991) originally developed for the atmospheric boundary layer is used in the present study for two reasons: 1) under certain not too restrictive conditions it results in an analytic solution for the growth of the mixed layer depth with time. This allows to choose the LES model domain size according to the applied surface cooling, 2) it gives a simple picture of the main effects of convective mixing including the phenomenon of 'counter-gradient' heat flux. This feature cannot be captured by traditional eddy-viscosity models as they rely on the down-gradient hypothesis.

Bulk (or slab) models represent a second group of mixed layer models apart from the diffusion models. While the latter solve partial differential equations for turbulence quantities bulk models approximate the mixed layer in an integral sense. The main feature in bulk modeling is the strong turbulent mixing embracing the whole layer and causing the approximate uniformity of the vertical profile of momentum, heat and tracers. At the interfaces to the surface and the entrainment layer, respectively, zero-order discontinuities are applied. At least under convective conditions the vertical homogeneity of the mixed layer is well verified from laboratory (Deardorff et al. 1980) and field studies (Anis and Moum 1994). Bulk models pioneered in oceanic research by Kraus and Turner (1967) are of low computational cost. Therefore, they are used to make long-time predictions (e.g., Gaspar 1988) or to parameterize the surface boundary layer in large-scale circulation models (e.g., Oberhuber 1993).

Closure of the vertically integrated equations requires knowledge about the entrainment processes at the base of the mixed layer. As the turbulence in the entrainment zone is highly intermittent accurate field measurements are difficult to make. On the other hand side, laboratory data only cover a small range of

Reynolds numbers.

In the next Section, the zero order jump model is introduced. Closure hypotheses for the zero order jump model is derived in Section 4.2. The distinct closure hypotheses will be derived as asymptotic cases of the Zilitinkevich (1991) model in Section 4.3. Analytical solutions for simple flow configurations will be shown in Section 4.4. It will then be discussed how the solutions can be applied in the setup of numerical studies.

In this Chapter, the letter ' D ' will refer to the dissipation rate of turbulent kinetic energy. The mixed layer depth will instead be referred to as ' h '.

5.2 The zero order jump model

Resulting from an unstable surface buoyancy flux (due to cooling or freezing), a density gradient forms near the surface. The density ϱ is expressed here in terms of buoyancy b ,

$$b(z) = g \frac{\varrho - \varrho_r(z)}{\varrho_0}.$$

A well-mixed layer forms which is separated from the surface region by a buoyancy jump. Since the layer is nearly homogeneous in vertical direction, the buoyancy can be considered as depth constant. The homogeneous mixed layer is separated from the nonturbulent layer underneath. The stable stratification of this layer is characterised by the Brunt-Väisälä frequency N . The interfacial layer between the mixed and the nonturbulent layer is called 'entrainment zone'. In the entrainment zone kinetic energy of bouyant plumes is spent for penetration into the stably stratified layer and for upward entrainment.

In zero order jump modeling (Lilly 1968) horizontal homogeneity without large-scale subsidence is assumed. Vertical buoyancy b and buoyancy flux B are represented by discontinuous functions:

$$\begin{aligned} b &= \begin{cases} \bar{b} & \text{if } z < h \\ \bar{b} + \Delta b + N^2 \cdot z & \text{if } z > h, \end{cases} \\ B &= \begin{cases} (1 - z/h) B_0 + z/h \cdot B_h & \text{if } z < h \\ 0 & \text{if } z > h. \end{cases} \end{aligned} \quad (5.2.1)$$

Here, \bar{b} is the mean buoyancy, Δb is the buoyancy jump at the mixed layer base, h is the mixed layer depth (the letter ' D ' is reserved in this Chapter for the dissipation rate of turbulent kinetic energy), B_0 is the surface buoyancy flux and the negative buoyancy flux at the mixed layer base is given by

$$B_h = -\Delta b \frac{dh}{dt} = -\Delta b w_e, \quad (5.2.2)$$

where $w_e = dh/dt$ is often called 'entrainment velocity'. The discontinuous approximation is illustrated in Figure 5.1. However, it is more convenient for comparison with the LES results to replace the buoyancy flux B by the kinematic heat

flux Q . Both are linearly related via equation (1.0.2) but their sign is reversed. The evolution equation for the buoyancy b in the case of horizontal homogeneity

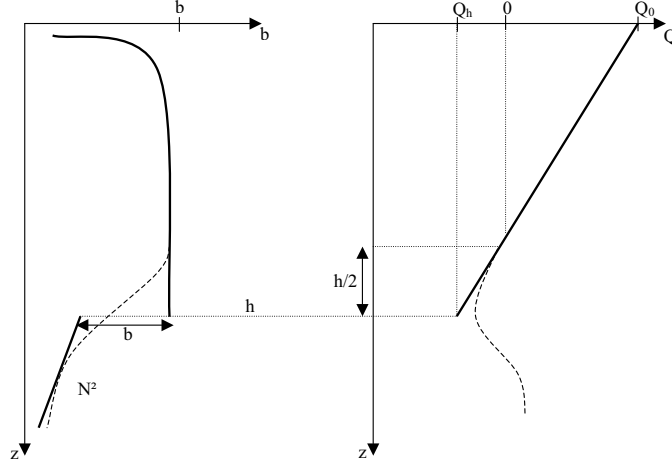


Figure 5.1: The discontinuous approximation of buoyancy b and heat flux Q . For calculating, buoyancy flux B is more convenient but for comparison with LES results Q is displayed. The dashed lines indicate the continuous profiles and the thick lines the discontinuous approximation. The buoyancy jump Δb is taken at the outer edge of the mixed layer and $\Delta h/2$ denotes half the entrainment zone extent.

takes the form

$$\frac{\partial b}{\partial t} = -\frac{\partial B}{\partial z}. \quad (5.2.3)$$

Termwise vertical integration of (5.2.3) from the surface to the mixed layer depth h and ignoring molecular transfer as well as temperature transport through the mixed-layer base can be simplified (Zilitinkevich 1991) to result in

$$\frac{d}{dt} \left(\frac{1}{2} N^2 h^2 - h \Delta b \right) = B_0. \quad (5.2.4)$$

Hence, the profiles of mean temperature and buoyancy flux in penetrative convection are determined by two time-dependent parameters, mixed layer depth $h(t)$ and buoyancy jump $\Delta b(t)$, which are coupled via (5.2.4). Closure of the mixed layer equations requires knowledge of the entrainment process at the mixed layer base.

5.3 The entrainment law

The simplest approach to the entrainment phenomenon is assuming that the negative buoyancy flux at the mixed layer base is a fixed fraction of the surface flux,

$$B_h = -A \cdot B_0, \quad (5.3.1)$$

with the 'entrainment coefficient' A . Equation (5.3.1) forms, together with (5.2.4), a closed pair of equations for determining $h(t)$ and $\Delta b(t)$. Experimental results for the entrainment coefficient A lay in the range 0.1 - 0.3 (Stull 1976). The entrainment velocity can be nondimensionalized by the Deardorff velocity scale $w_* = (B_0 h)^{1/3}$ which is the appropriate velocity scale for not too strong shear. The resulting parameter is the 'entrainment rate'

$$E = \frac{1}{w_*} \frac{dh}{dt}. \quad (5.3.2)$$

Entrainment rate and entrainment coefficient are commonly related by a Richardson number based on the buoyancy jump in the thermocline, $Ri_1 = h\Delta b/w_*^2$, via

$$E = A \cdot Ri_1^{-1}, \quad (5.3.3)$$

This formulation of the 'entrainment law' has been suggested by, e.g. Betts (1973), Tennekes (1973) and the laboratory studies by Deardorff et al. (1980). It will be shown below how (5.3.3) can be recovered from the Zilitinkevich (1991) formulation as a special case.

Starting point for the derivation of the entrainment law is the budget equation for turbulent kinetic energy K in the mixed layer¹

$$\frac{\partial K}{\partial t} = -D_f(K) + P_S - B - D. \quad (5.3.4)$$

P_S is the production rate due to wind generated shear,

$$D_f(K) = \frac{\partial F}{\partial z}$$

denotes the third-order terms which are vertical gradients of turbulent fluxes F due to velocity and pressure fluctuations and D is the dissipation rate of turbulent kinetic energy. Equation (5.3.4) is integrated over the whole mixed layer depth starting from the surface. Assuming that below the mixed layer turbulence is small (i.e. $K_h \approx 0$), the left-hand side term is given by

$$\int_0^h \frac{\partial K}{\partial t} dz = h \frac{dK}{dt} + K_h \frac{dh}{dt}. \quad (5.3.5)$$

¹The total amount of turbulent kinetic energy is called K and its corresponding dissipation rate is called D . In contrast, e in the previous Chapters denotes the *subgrid* turbulent kinetic energy and ε its dissipation rate. K can be thought of being the sum of e and the amount of turbulent kinetic energy which is explicitly resolved in Large-eddy simulations.

From now on, vertical averages over the mixed layer are considered which are indicated by calligraphic letters.

The first term on the right side of (5.3.4) denotes vertical losses of turbulence due to the radiation of internal waves into the adjacent stable layer. Zilitinkevich (1991) takes

$$\int_0^h \frac{\partial F}{\partial z} dz = F_h \approx C_F N^3 h^3 \left(\frac{A}{1+A} \right)^3, \quad (5.3.6)$$

where the turbulent fluxes through the surface vanish, N is the Bruunt-Vaisala frequency and $C_F \approx 0.02$. The parameterisation (5.3.6) for the energy transport is questionable in the presence of shear but no other has yet been proposed (Mironov, priv. comm.).

The second term of (5.3.4) gives the contribution of shear which reads

$$P_S = - \left(\tau^{(x)} \frac{\partial U}{\partial z} + \tau^{(y)} \frac{\partial V}{\partial z} \right), \quad (5.3.7)$$

where $\tau^{(x)} = \overline{uw}$, $\tau^{(y)} = \overline{vw}$ are the Reynolds shear stresses. The Ekman layer equations (2.1.1) are integrated to give

$$\begin{aligned} h \frac{d\mathcal{U}}{dt} &= fh(\mathcal{V} - V_{geo}) - \tau_0^{(x)} + (U_h - \mathcal{U}) \frac{dh}{dt}, \\ h \frac{d\mathcal{V}}{dt} &= fh(\mathcal{U} - U_{geo}) - \tau_0^{(y)} + (V_h - \mathcal{V}) \frac{dh}{dt}, \end{aligned} \quad (5.3.8)$$

where the index 'geo' denotes the geostrophic velocity component. Here the last terms on the right side represent effective momentum entrainment at the mixed layer base where velocities U_h and V_h are from the non-turbulent layer underneath. They have to be specified, for instance by geostrophic balance. The integral production rate can be approximated as (Zilitinkevich, 1990)

$$\int_0^h P_S dz = (\mathcal{U} \tau_0^{(x)} + \mathcal{V} \tau_0^{(y)}) + \frac{1}{2} \left((U_h - \mathcal{U})^2 + (V_h - \mathcal{V})^2 \right) \frac{dh}{dt}. \quad (5.3.9)$$

The third term of (5.3.4) shows the entrainment effect of turbulence. The buoyancy flux profile is approximated as linear composition of two contributions, at the surface and at the base,

$$B = \left(1 - \frac{z}{h} \right) B_0 + \frac{z}{h} B_h. \quad (5.3.10)$$

Vertical integration results in

$$\int_0^h B dz = \frac{h}{2} (B_0 + B_h). \quad (5.3.11)$$

It remains to evaluate the vertical averaged profiles of turbulent kinetic energy and its dissipation rate, i.e. \mathcal{K} and \mathcal{D} . Three velocities enter the problem : the

free convective scale w_* , the surface friction velocity u_* and the friction velocity based on the velocity jump at the mixed layer base,

$$u_*^{(h)} = 2^{-1/2} \left((U_h - \mathcal{U})^2 + (V_h - \mathcal{V})^2 \right)^{1/4} \left(\frac{dh}{dt} \right)^{1/2}. \quad (5.3.12)$$

Zilitinkevich (1990) argues that in the bulk of the mixed layer energy and dissipation rate might be scaled with w_* while the other two velocities are only important near the boundaries. However, Sullivan et al. (1994) found it appropriate to account for surface shear stress and scaled sheared convection LES data with the velocity $w_m = (w_*^3 + 5u_*^3)^{1/3}$. Therefore, a general expression is

$$\begin{aligned} \mathcal{K} &\approx c_{\mathcal{K}3} w_m^2, \\ \mathcal{D} &\approx c_{\mathcal{D}3} \frac{w_m^3}{h}. \end{aligned} \quad (5.3.13)$$

The constants have been found from atmospheric observations, water tank experiments and LES data (Schmidt and Schumann 1989, Zilitinkevich 1991) to be $c_{\mathcal{K}3} \approx (0.4 - 0.5)$, $c_{\mathcal{D}3} \approx (0.3 - 0.4)$. The constants were originally found for shear-free boundary layers but they are simply adopted for the sheared case. The entrainment equation can now be found by inserting (5.3.5), (5.3.6), (5.3.9), (5.3.11) and (5.3.13) into the vertical integrated version of (5.3.4), resulting in

$$\begin{aligned} h \frac{d(c_{\mathcal{K}3} w_m^2)}{dt} + c_{\mathcal{K}3} w_m^2 \frac{dh}{dt} = & -C_F N h \left(\frac{A}{1+A} \right)^3 + \\ & (\mathcal{U} \tau_0^{(x)} + \mathcal{V} \tau_0^{(y)}) + \frac{1}{2} \left((U_h - \mathcal{U})^2 + (V_h - \mathcal{V})^2 \right) \frac{dh}{dt} + \\ & \frac{h}{2} (B_0 + B_h) - c_{\mathcal{D}3} w_m^3. \end{aligned} \quad (5.3.14)$$

The main goal of the one-dimensional modeling of turbulent penetrative convection has now been reached: the equation of total buoyancy budget (5.2.4), the entrainment equation (5.3.14), the evolution equations for the velocity components (5.3.8), together with the initial conditions (5.2.1), form a closed set of equations for the four unknown mixed layer depth $h(t)$, buoyancy jump $\Delta b(t)$ and velocities $\mathcal{U}(t), \mathcal{V}(t)$.

5.4 Recovering of the empirical entrainment law

The entrainment equation considerably simplifies in the case of free convection in which the surface stress $\vec{\tau}_0$ vanishes and $w_m = w_*$. Then, (5.3.14) reads as

$$c_{\mathcal{K}3} \left(w_*^2 \frac{dh}{dt} + h \frac{d}{dt} w_*^2 \right) = -C_F N h \left(\frac{A}{1+A} \right)^3 + \frac{h}{2} (B_0 + B_h) - c_{\mathcal{D}3} w_*^3. \quad (5.4.1)$$

This expression can be rewritten using $B_0 \cdot h = w_*^3$, (5.3.2), (5.3.3), Ri_1 and introducing a second Richardson number based on the stratification of the undisturbed layer underneath,

$$Ri_2 = \frac{1}{2} \frac{N^2 h^2}{w_*^2}, \quad (5.4.2)$$

resulting in

$$\left(\frac{5}{3} c_{K3} + \frac{1}{2} Ri_1 \right) E = \frac{1}{2} - c_{D3} - C'_F Ri_2^{3/2} \left(\frac{Ri_1 E}{1 - Ri_1 E} \right)^3, \quad (5.4.3)$$

where $C'_F = C_F \cdot 2^{3/2}$. If the undisturbed layer is weakly stratified, i.e. $Ri_2 \approx 0$, and the system is in a quasi-stationary state, i.e. $Ri_1 \gg 10/3 c_{K3}$, then

$$E = (1 - 2c_{D3}) \cdot Ri_1^{-1}. \quad (5.4.4)$$

The result corresponds to the empirical entrainment law (5.3.3) and the entrainment coefficient A can be identified with $1 - 2c_{D3}$.

5.5 Analytical Solutions for Free Convection

An analytical solution related to the LES experiments can be derived for the situation of quasi-stationary free convection in which (5.4.3) takes the form

$$A + C''_F Ri_2^{3/2} \left(\frac{A}{1 + A} \right)^3 = A, \quad (5.5.1)$$

($C''_F = C_F \cdot 2^{5/2} \approx 0.1$), which forms, together with (5.2.4) and the initial conditions,

$$h = \Delta b = 0 \text{ at } t = 0, \quad (5.5.2)$$

a closed set of equations for the growth of the mixed layer depth $h(t)$ and the buoyancy jump $\Delta b(t)$. At the beginning the asymptotic solutions are

$$\begin{aligned} h(t) &= \left(\frac{2B_0 t (1 + 2A)}{N^2} \right)^{1/2}, \\ \Delta b(t) &= A N \left(\frac{2B_0 t}{1 + 2A} \right)^{1/2}. \end{aligned} \quad (5.5.3)$$

With increasing time there is another asymptotic solution,

$$\begin{aligned} h(t) &= \left(\frac{2B_0 t}{N^2} \right)^{1/2}, \\ \Delta b(t) &= \left(\frac{4A}{C''_F} \right)^{1/3} N^{2/3} B_0^{1/2} t^{1/6}. \end{aligned} \quad (5.5.4)$$

The solutions (5.5.4) allow to configurate numerical experiments as they are a fairly accurate estimation of the steady-state flow. The use of (5.5.4) will be described in the next Chapter.

Chapter 6

The LES experiments

In this study, free convective flows are compared with convective shear flows. One approximately shear-free convective flow, referred to as 'weak', and two flows affected by shear, referred to as 'moderate' and 'strong', respectively, are generated.

The three external parameters B_0 , N^2 and simulation time t from (5.5.4) can be combined in a way to fulfill the following requirements:

- The simulation time t_{end} is large enough to reach a steady state which requires that $t_{end} \approx 7t_*$ where $t_* = D/w_*$ is the large eddy-turnover time scale (Schmidt and Schumann 1989),
- The vertical domain should be almost twice as large as the mixed layer depth because of internal wave reflections at the lower boundary.

The buoyancy flux is entirely caused by temperature fluctuations and salinity is taken as constant. This is simply done to save computational time and a conservation equation for salinity can easily be added.

The study's focus is on the evolution of convection after former convective events due to which the upper layers are homogenized. For any particular simulation, the initial potential temperature profile is therefore chosen as a three-layer structure: in the upper mixed layer a constant temperature, a strong gradient at the thermocline and a weaker constant stratification in the depth. The model ocean is assumed to be in Ekman equilibrium due to strong shear stress at the atmosphere-ocean interface.

The simulations start with the mixed layer at rest. Initially, the mixed layer depth is 100 m and its temperature is $-1.0K$. Below the mixed layer the entrainment zone extends over 30 m with a constant temperature gradient of $2 \cdot 10^{-3} K m^{-1}$. Underneath, in the stable stratified deeper part there is a constant temperature gradient of $5 \cdot 10^{-4} K m^{-1}$ throughout the whole model domain. The initial profile shown in Figure 7.1. The flow is then perturbed by adding a small random component to the temperature field. The simulation is run for several large-eddy

Run	$W_{10}(m/s)$	$u_*(m/s)$	$T_{air}(^{\circ}C)$	$B_0(m^2s^{-3})$
WEAK	2	$2.24 \cdot 10^{-3}$	-97	$-3.82 \cdot 10^{-8}$
MODERATE	7	$7.78 \cdot 10^{-3}$	-32.6	$-3.82 \cdot 10^{-8}$
STRONG	14	$1.56 \cdot 10^{-2}$	-15	$-3.82 \cdot 10^{-8}$

Table 6.1: Numerical parameters for the three runs

turnover times. After about six large-eddy turnover times, the flow is expected to achieve a stationary state. The final mixed layer depth can be estimated from equation (5.5.4) to $230m$ after a simulation time of $24 h$. These estimations will be used to create the numerical grid. In order to accomodate several plume structures, the horizontal extent of the computational domain has to be about ten times the mixed layer depth (Moeng and Sullivan 1994). The vertical extent has to be about twice the mixed layer depth. The second requirement ensures that internal waves reflected at the bottom boundary do not disturb the solution significantly.

The grid spacing has to provide that the energy-containing parts of the spectrum are well resolved. As a reasonable cut-off wave number $k_c \cdot D = 100$ is chosen. At wavenumber k_c , the spectral energy is found to be decreased relative to the peak value (at $k \cdot D = 20$) by a factor of 50 (Deardorff and Willis, 1985). In the inertial subrange, Mason (1994) shows that grid spacing Δ and cut-off wave number are related via

$$\Delta = \frac{D}{C_S k_c D} (1.5 Ko)^{-3/4} \approx \frac{D}{40}. \quad (6.0.1)$$

Consequently, 40 vertical points are used to resolve the mixed layer and the vertical grid spacing is given by $\Delta z = 230m/40 \approx 5m$. In summary, 64 vertical grid cells are used. It should be noted that according to the values for the friction velocity in table 6.1 the Ekman layer depths are 11, 40 and $80m$ which is clearly the lower limit of what can be represented on a grid with $5m$ vertical resolution, to say the least. In the x - and y -directions, the computational domain contains 128 grid cells with a grid spacing $\Delta x = \Delta y = 20m$. The horizontal grid size is a compromise between the requirement that the computational domain is large enough and the requirement that the numerical grid does not induce an artificial anisotropy between horizontal and vertical scales.

The mixed layer depth D is computed from LES data as the vertical location of the average minimum heat flux following Deardorff (1980)¹. All runs are tuned to have the same thermodynamical forcing, namely a surface heat loss to the atmosphere of $\mathcal{H}_0 = 650Wm^{-2}$. This corresponds to different atmospheric surface temperatures. The 'strong' run has been chosen as the reference case

¹This definition allows a simple computation. However, it can hardly be compared to field measurements and ignores horizontal variations. More realistic definitions have been investigated by Sullivan et al. (1998).

with a (realistic) atmospheric temperature of $-15^{\circ}C$. In order to give the same heat flux for all runs, it was necessary to choose an atmospheric temperature of $-32.6^{\circ}C$ for the 'moderate' case and a rather artificial temperature of $-97^{\circ}C$ for the 'weak' run. However, it is the scope of the work to isolate the role of mean shear.

The input parameters of the three runs are listed in Table 6.1. The wind blows in meridional direction.

Chapter 7

Results

The analysis is applied after a simulation time of 24 h . The values are nondimensionalised by the velocity, temperature and height scales appropriate for convective flows (Deardorff 1972), namely Deardorff velocity w_* , temperature scale $T_* = Q_0/w_*$ where Q_0 is the kinematic heat flux at the surface and D is the mixed layer depth. The simulation time corresponds to roughly eight large eddy-turnover time scales $\tau_* = D/w_*$ which is expected to be sufficient for a steady-state (Schmidt and Schumann 1989). Applying the minimum heat flux criterion from Chapter 5 results in the following scales (see table 7.1).

It can be seen that the estimation from the bulk model (5.5.4), $D \approx 230m$ is within 10 per cent of the numerical results. This is a good agreement regarding that (5.5.4) resulted from a strong simplification of the more complete equation (5.3.14) and that the parameter have simply been adopted from laboratory and atmospheric measurements.

7.1 Mean flow profiles

Mean values are averaged over the horizontal plane denoted by $\langle f \rangle$ where f is any quantity.

Figure 7.1 shows the mean potential temperature profiles versus nondimensional depth. They are compared with the initial temperature distribution (thick line). The run 'weak' is indicated by a dash-dotted line whereas the 'moderate' and the 'strong' case are indicated by dotted and solid lines, respectively. This notation

Run	$D(m)$	$w_*(m/s)$	$\Pi_* = u_*/w_*$	sampling time/ τ_*	$T_{ML}(^{\circ}C)$
WEAK	220	$2.03 \cdot 10^{-2}$	0.11	7.97	-1.0959
MODERATE	225	$2.05 \cdot 10^{-2}$	0.38	7.87	-1.0955
STRONG	210	$2.00 \cdot 10^{-2}$	0.78	8.23	-1.0929

Table 7.1: Internal parameters for the three runs

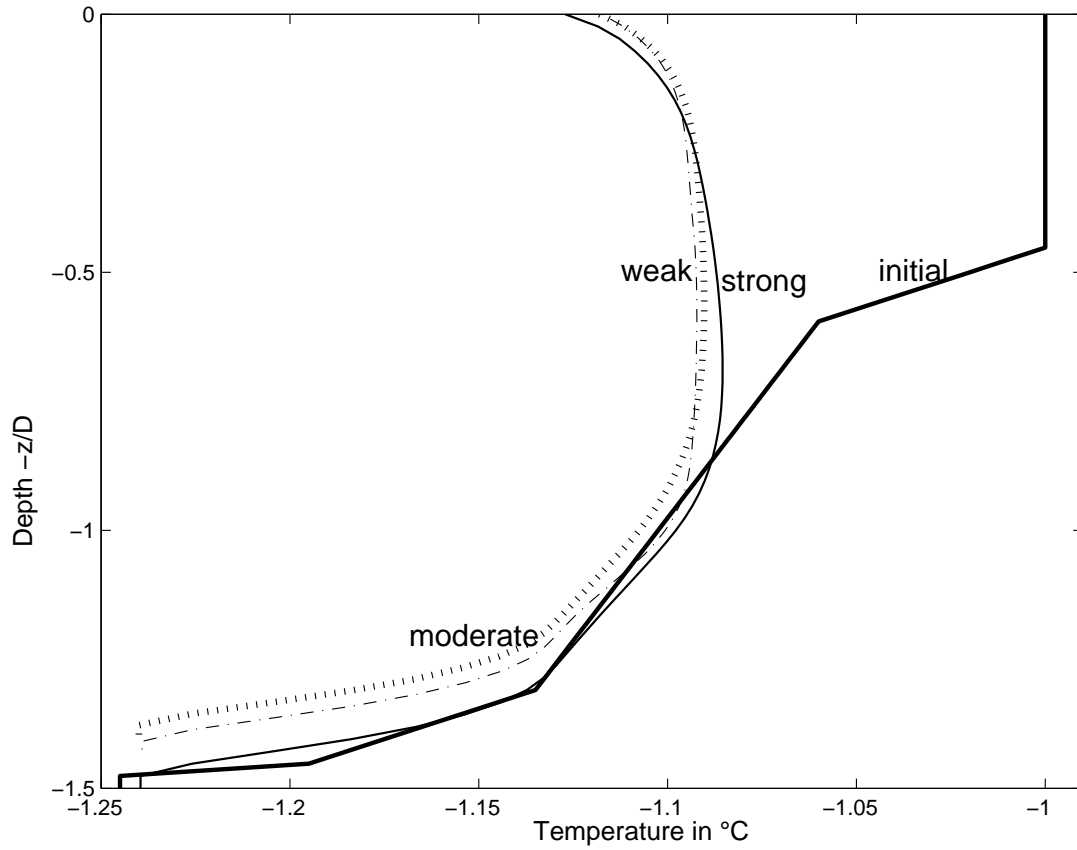


Figure 7.1: Vertical distributions of the mean potential temperature. The thick line denotes the initial profile whereas the dash-dotted, dotted and solid lines depict the runs 'weak', 'moderate' and 'strong', respectively.

holds for all the mean profile figures. The comparison with the simplified Figure 5.1 from bulk modeling reveals that the main features are the same for all of the three runs: the nearly homogeneous mean temperature profile in the bulk of the mixed layer indicates the effectiveness of turbulent mixing by the convective plumes. In the surface layer, a temperature gradient has formed. Hence the plumes fail to homogenize the water column in wall proximity where they are strongly damped. While the profiles of runs 'moderate' and 'weak' are nearly the same close to the surface the run 'strong' exhibits a broader surface layer. The minimum temperature in the bulk of the layer is lowest for the 'strong' case. However, in an integral sense averaged from the surface to the mixed-layer depth, the averaged temperature for the run 'weak' is the lowest, namely $-1.0959^{\circ}C$ (see Table 7.1). The corresponding averaged temperatures for the runs 'moderate' and 'strong' are $-1.0955^{\circ}C$ and $-1.0929^{\circ}C$, respectively. It has to be kept in mind that the temperature difference is rather small but the mixed layers in run 'weak' and 'moderate' are significantly deeper than in run 'strong' according to Table 7.1. However, the differences are small, especially those between the runs 'moderate' and 'weak'. One can only conclude that if there is any influence of shear on the efficiency of convective mixing at all, it will be rather negligible. The deviation from homogeneity at about $0.9 D$ markers the extent of the entrainment region. As a consequence of entrainment a gradient has formed here but less pronounced than at the surface. The gradient is strongest for run 'moderate'.

Figure 7.2 displays the profiles of the horizontal velocity components at the end of the simulations (thick lines) for the three cases, respectively. They are compared with the initial velocity field (thin lines) derived from the simplified Ekman balance (equation (2.1.1)). The red lines show the zonal components, the blue lines the corresponding meridional components. Note the different range of velocities in the three figures. The run 'weak' reveals a shallow Ekman layer. The non-smooth profiles of the Ekman velocity components (thin lines) indicate that the grid spacing is hardly sufficient to resolve the initial Ekman dynamics properly. The runs 'moderate' and 'strong' show the well-known Ekman spiral for the initial velocity field. In these cases, the Ekman dynamics is well-resolved. In the final stage (thick lines), the profiles have turned considerably. Apparently, the characteristics of the Ekman spiral have been partially transported in greater depths by convective turbulence but its features have been strongly damped additionally. A common feature to all the runs is that the velocity profiles are close to zero in the bulk of the mixed layer while the gradients near the surface have broadened compared to the Ekman profiles. For run 'strong' the near-surface current remains approximately the same as for the initial Ekman dynamics whereas for the runs 'weak' and 'moderate', even the flow at the very surface is strongly damped due to convective mixing. Apparently, convective plumes failed to homogenize the surface region in run 'strong' where unstable stratification shows little influence. In the entrainment regions there is little horizontal flow in run

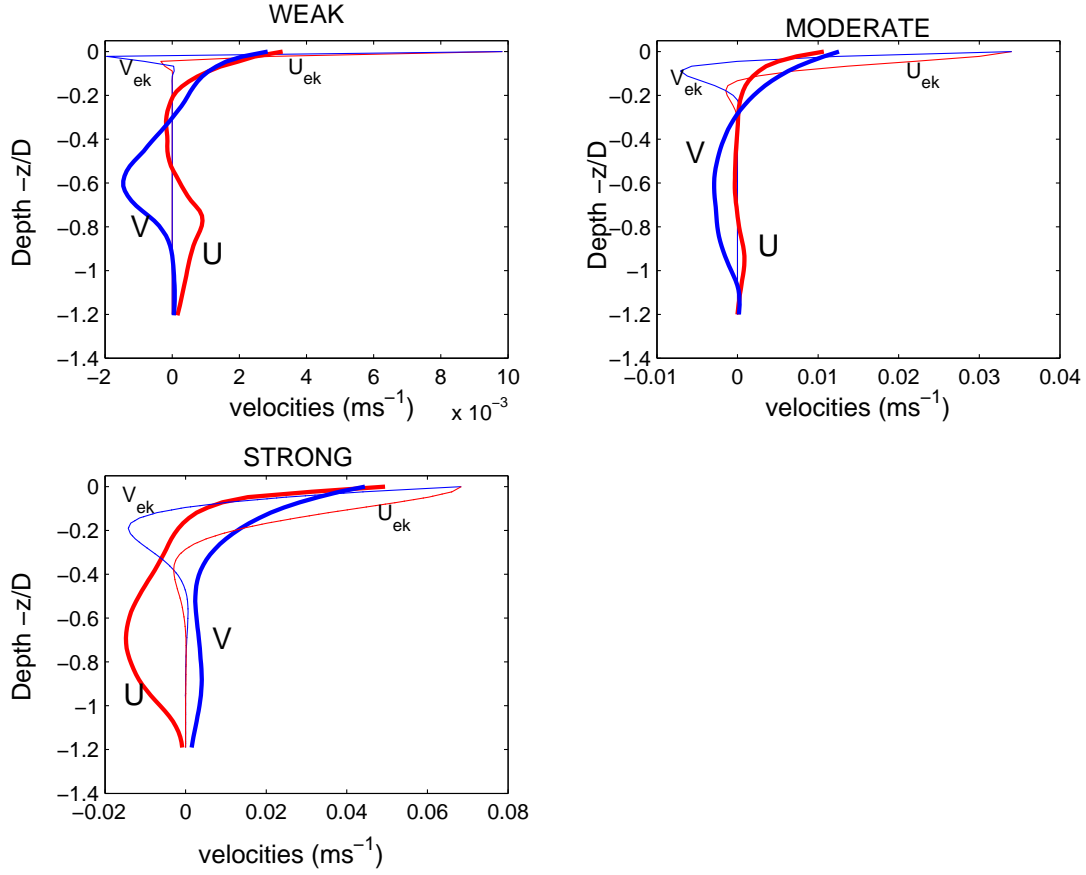


Figure 7.2: Vertical distributions of the mean horizontal velocity components. The LES results for runs 'weak', 'moderate' and 'strong' are displayed. The thick lines represent the final velocities after 24 *h* of simulation while the thin lines represent the initial velocities from the Ekman 'spin-up'. Red lines depict the meridional components and blue lines depict the zonal components, respectively.

Horizontal velocity from $z/D = 0.02$ to $z/D = 0.28$

from $z/D = 0.35$ to $z/D = 0.61$

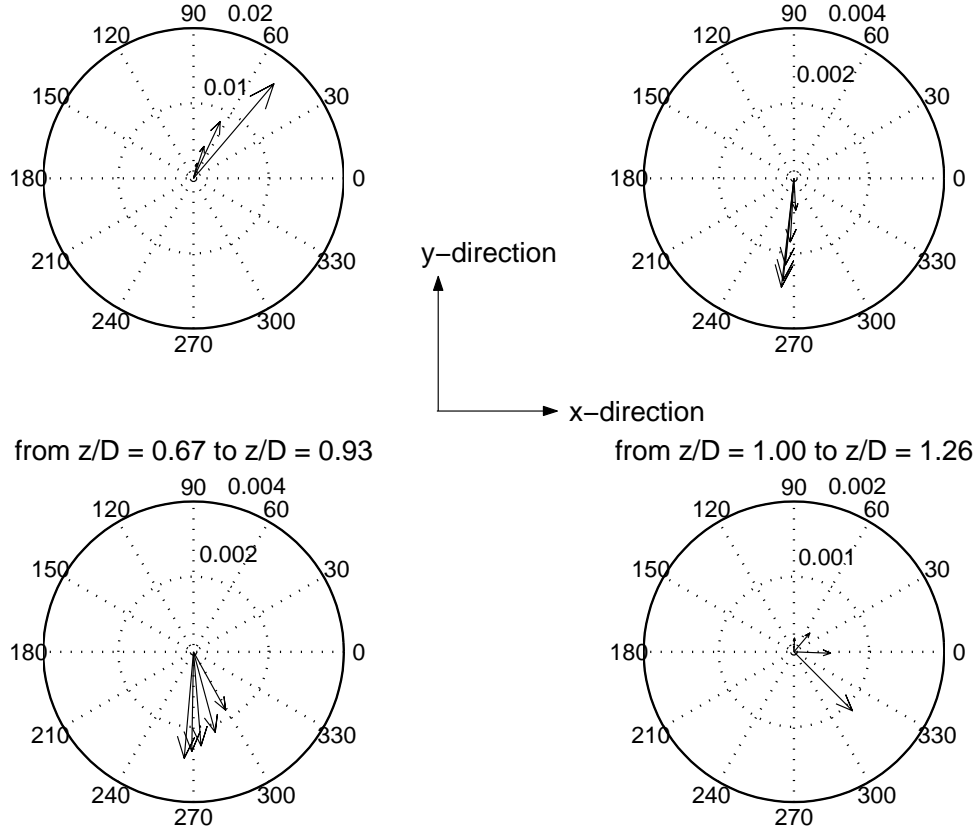


Figure 7.3: Polar plot for the horizontal velocity vector in run 'moderate'. The plots show four depth intervals starting from the upper left panel. The arrows display velocity vectors at a grid spacing of 10 m , respectively. Note the distinct range of velocity contours (in ms^{-1}).

'moderate' but significant flow and vertical shear in the runs 'weak' and 'strong'. This result might indicate that shear processes play a role during entrainment of heavier water from underneath. It cannot be explained why the run 'moderate' shows a distinct behaviour from the other two.

The turning of the horizontal velocity vector is displayed somewhat differently in polar plots for the runs 'moderate' (Figure 7.3) and 'strong' (Figure 7.4), respectively. The run 'weak' has been skipped from further analysis since its Ekman layer is only poorly resolved. Note that the Ekman spiral from the initialization would show up in this polar plot as an arrow pointing at 45° near the surface decreasing rapidly with depth and turning to the right. In contrast, run 'moderate' reveals that the magnitude of the velocity vector is much smaller near the surface. The vector points predominantly in negative zonal direction in the bulk

Horizontal velocity from $z/D = 0.02$ to $z/D = 0.30$

from $z/D = 0.38$ to $z/D = 0.65$

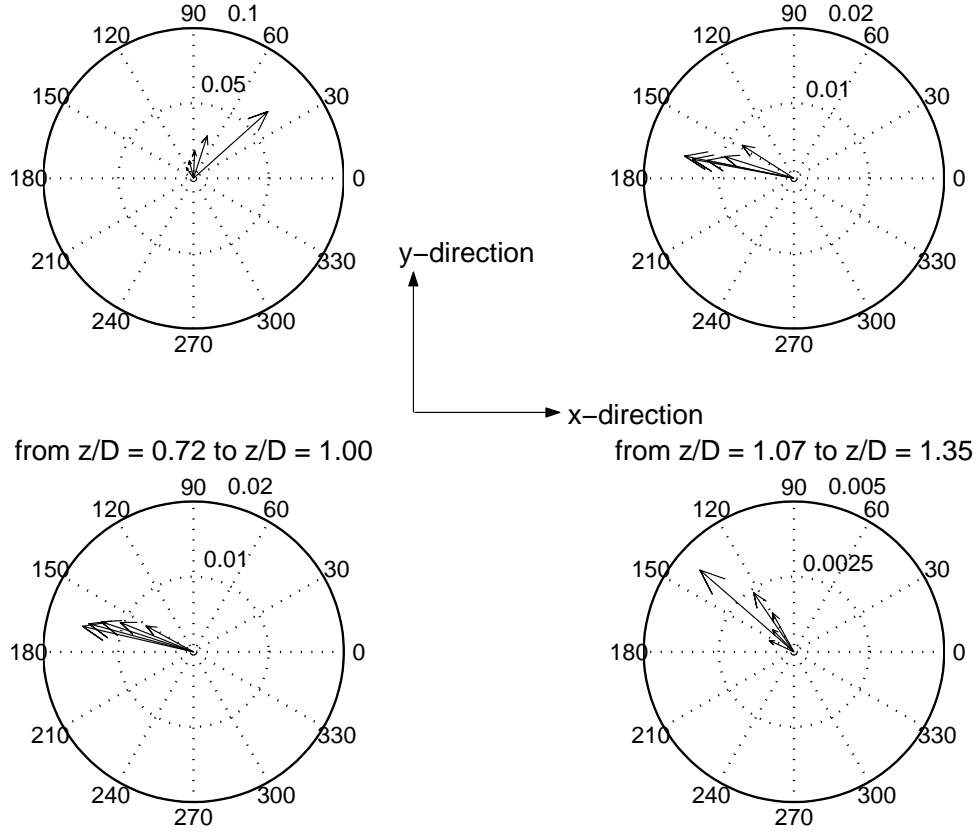


Figure 7.4: Polar plot for the horizontal velocity vector in run 'strong'. The plots show four depth intervals starting from the upper left panel. The arrows display velocity vectors at a grid spacing of $10\ m$, respectively. Note the distinct range of velocity contours (in ms^{-1}).

of the layer which can be interpreted as compensating the surface flow behaviour. Here, the velocity is on the order of $1/5$ of the near-surface value. At the mixed layer base, anticlockwise turning is observed. The run 'strong' shows a complete distinct picture. Here, the flow in the bulk of the layer is predominantly in negative meridional direction. The magnitude is again about $1/5$ of the near-surface value. The turning at the mixed-layer base is in clockwise direction. The two distinct behaviours in runs 'moderate' and 'strong' indicate the convective shear flow is not only a result of interaction between mean shear and thermal instability but that the effect of Earth's rotation enters the flow through the turning of the mean shear direction.

It is obvious that the momentum transport, i.e. the vertical integrated momentum is very different from what is known from classical Ekman theory. From

Run	$\mathcal{U}_E^{th} (m^2/s)$	$\mathcal{V}_E^{th} (m^2/s)$	$\mathcal{U}_E^{exp} (m^2/s)$	$\mathcal{V}_E^{exp} (m^2/s)$	$\alpha^{exp} (^\circ)$
MODERATE	0.43	0	0.19	-0.01	87
STRONG	1.73	0	-1.18	1.88	-58

Table 7.2: Ekman volume transport: Theoretical prediction for neutral conditions versus findings from numerical experiments with unstable conditions.

vertical integration of the Ekman equations the Ekman volume transport in neutral stratification can be calculated exactly. In steady conditions, the transport is directed at right angles to the surface stress. The transport component \mathcal{U}_E is equal to the surface stress in zonal direction divided by the vertical Coriolis parameter (e.g., Gill 1982). In the present study, the wind blows in meridional direction. Hence,

$$\begin{aligned}\mathcal{U}_E &= u_*^2/f_z, \\ \mathcal{V}_E &= 0,\end{aligned}$$

are the analytical steady-state solutions in neutral stratification. In Table 7.2, these results are contrasted with the numerical findings. The findings for run 'moderate' confirm that qualitatively the transport behaves similar as in the neutral case: The zonal component nearly vanishes since the near-surface transport is approximately balanced by the recirculating flow in the bulk of the mixed layer while the meridional component is small but nonzero throughout. Hence, the transport angle α_{exp} is close to 90° . Quantitatively, the mean flow transport is damped by more than 50 percent due to the secondary convective flow. For run 'strong' the meridional transport has almost reversed while the zonal transport is mainly made of its contributions near the surface and at the mixed layer edge. The resulting transport angle α_{exp} is -58° . Apparently, the mean flow is fed by the secondary convective flow.

In summary, the addition of a negative flux to the Ekman dynamics has two very distinct consequences depending on the wind. Run 'moderate' which corresponds to strong bouyant and moderate wind forcing shows that the mean flow is weakened compared to the neutral case. Run 'strong' which corresponds to strong bouyant and strong wind forcing shows the opposite: the mean flow is enhanced compared to the neutral case.

7.2 Instantaneous flow structures

In order to detect the presence of coherent structures in the convective flow field and to elucidate the differences due to the interaction with shear, a flow visualization study of the instantaneous flow field was carried out. Vertical sections in the $y - z$ -plane of temperature are displayed versus nondimensional depth for the three cases 'weak' (Figure 7.5), 'moderate' (Figure 7.6), and 'strong' (Figure

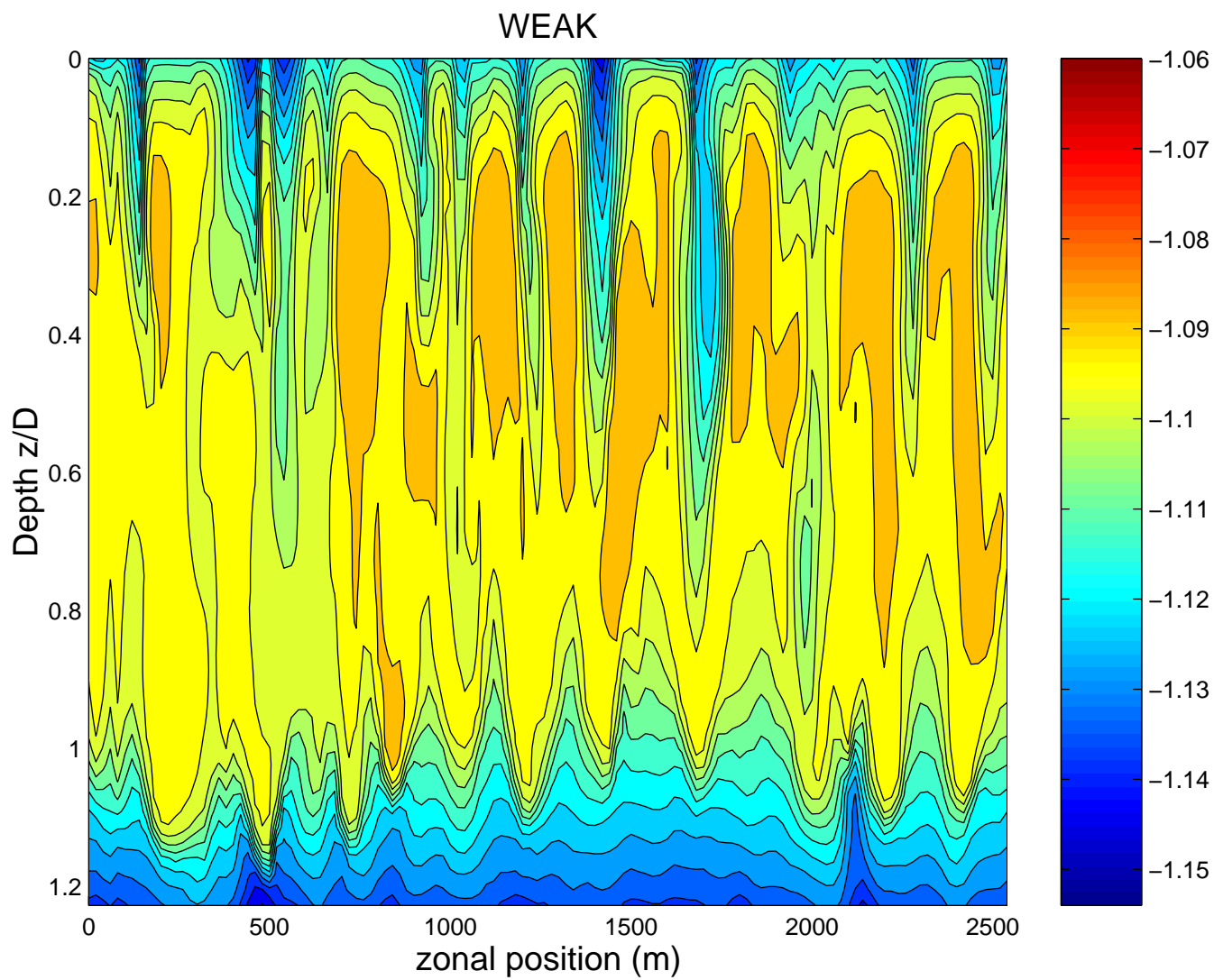


Figure 7.5: Cross-section of temperature field in the $y - z$ -plane, in the interior of the model domain, for run 'weak'.

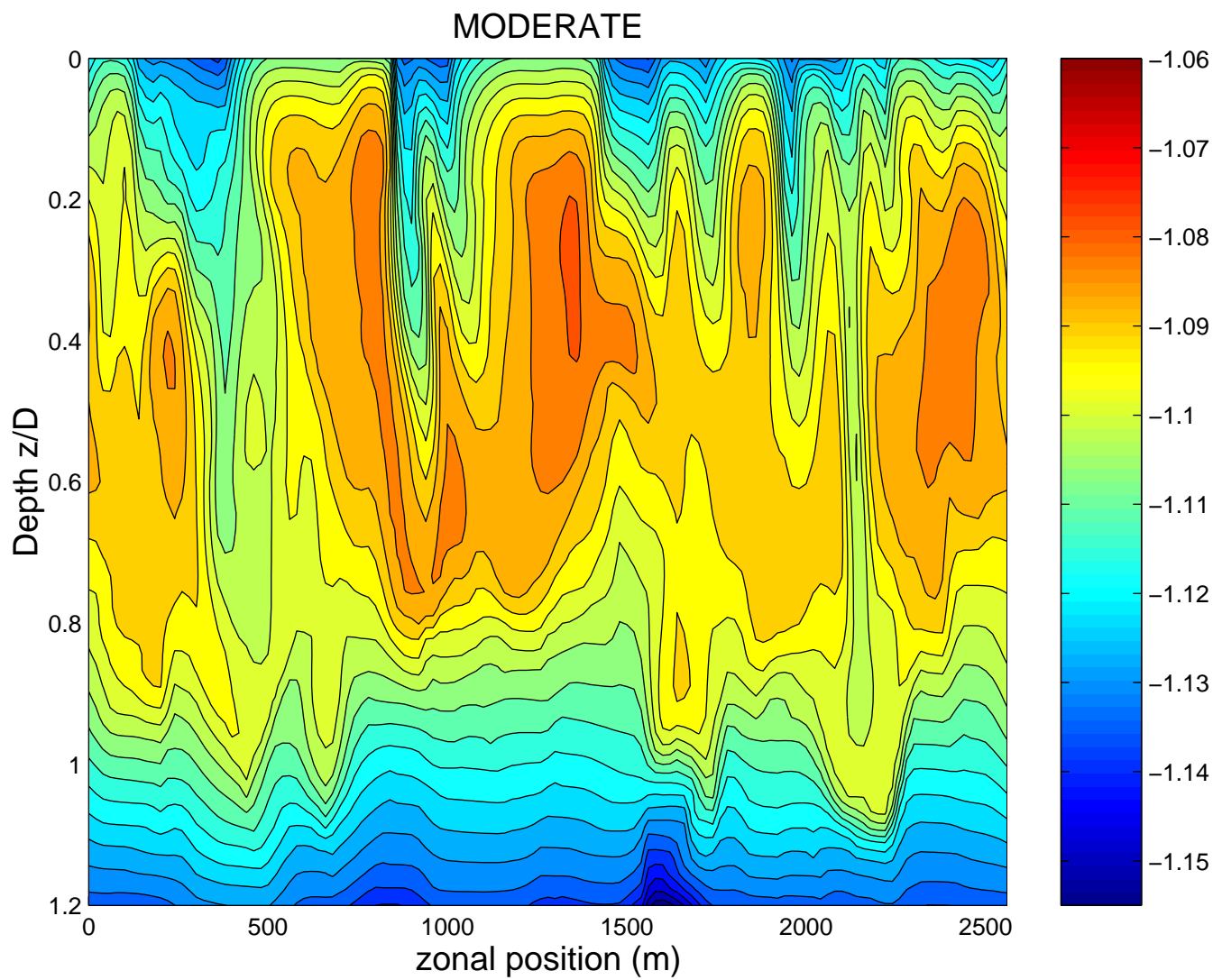


Figure 7.6: Cross-section of temperature field in the $y - z$ -plane, in the interior of the model domain, for run 'moderate'. The colorbar coincides with the colorbar in 7.5.

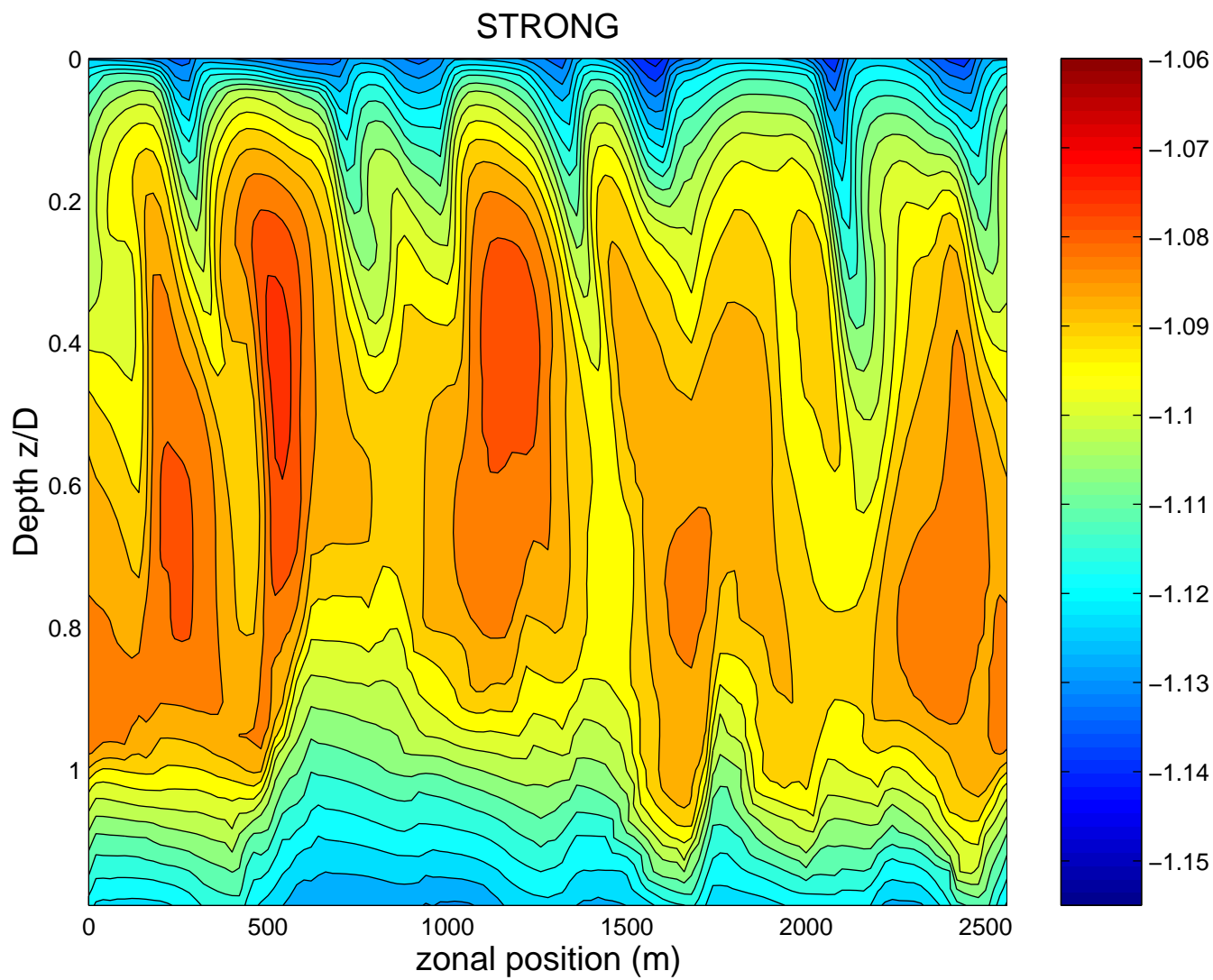


Figure 7.7: Cross-section of temperature field in the $y - z$ -plane, in the interior of the model domain, for run 'strong'. The colorbar coincides with the colorbar in 7.5.

7.7). The sections are taken at a zonal position of 1280 m , respectively. The model domain is shown only down to a nondimensional depth of about 1.2 and the vertical axes are enlarged compared to the horizontal ones. The range of color is the same in all three figures, the contour intervals are 0.005 $^{\circ}C$. Large plumes spanning the whole mixed layer are clearly visible in all three cases providing vigorous mixing. Single events penetrate down to about 1.2 D . The three simulations mainly differ in the surface and in the entrainment region. In run 'weak' (Figure 7.5), the well-mixed layer extends from 0.2 to 0.8 D in accordance with Figure 7.1. There is only a single plume event in the middle of Figure 7.5 which reaches from the surface to the outer edge of the mixed layer. All other plumes only reach down to roughly 0.5 D where they are entrained by the already homogenized water masses. At the outer edge of the mixed layer, plumes grow which intend to leave into the depth. The picture is in consistency with the 'filling-box' principle of convection (Backhaus, priv. comm.). The wave-like instability near the surface and near the base has a wavelength of roughly 200 m , i.e. approximately 1.0 D .

In contrast, the surface layer of run 'moderate' (Figure 7.6) looks quite different although the horizontal mean is very similar (see Figure 7.1). Local temperature gradients are higher than in simulation 'weak'. More deep-reaching events are visible which directly penetrate from surface into the stably stratified layer near the bottom. The mean wavelength of the wave-like instability near the surface is on the order of 320 m , i.e. 1.4 D but more random than for the case 'weak'. The middle of the mixed layer is still rather inhomogeneous. The entrainment zone shows less steep gradients compared to run 'weak'.

Run 'strong' (Figure 7.7) reveals even stronger localised temperature gradients in the near-surface region than run 'moderate'. In accordance with Figure 7.1, the well-mixed layer is restricted on the region between 0.4 and 0.8 D . All other flow regions are influenced whether by the near-surface instability or entrainment processes. The convective events penetrating into the mixed layer are as intense as the events in run 'moderate' but broader. Therefore they are easier to entrain by the well-mixed water masses on their way and less efficient in penetrating into the stably stratified layer underneath. The mean wavelength of the wave-like instability near the surface is on the order of 360 m , i.e. 1.7 D . It appears to be more regular than in run 'moderate' and resembles the smooth near-surface instability of run 'weak'. It might be speculated that due to the dominant wind stress the level of regularity is increased compared to run 'moderate'. A sequence of views of the temperature flow patterns at different depths are provided in the Figs. 7.8-7.10. They show the flow at the locations $z/D = 0.1, 0.5$, and 0.9 for run 'weak', 'moderate' and 'strong', respectively. The contour intervals are 0.005 $^{\circ}C$ again. For run 'weak' the temperature structure close to the surface is dominated by the forming of irregular cells. It is repeated that the wind blows in meridional direction. The cells show no visible orientation with the wind direction but are rather isotropic. The horizontal spacing of the cells is about 1.0 D . The cells are

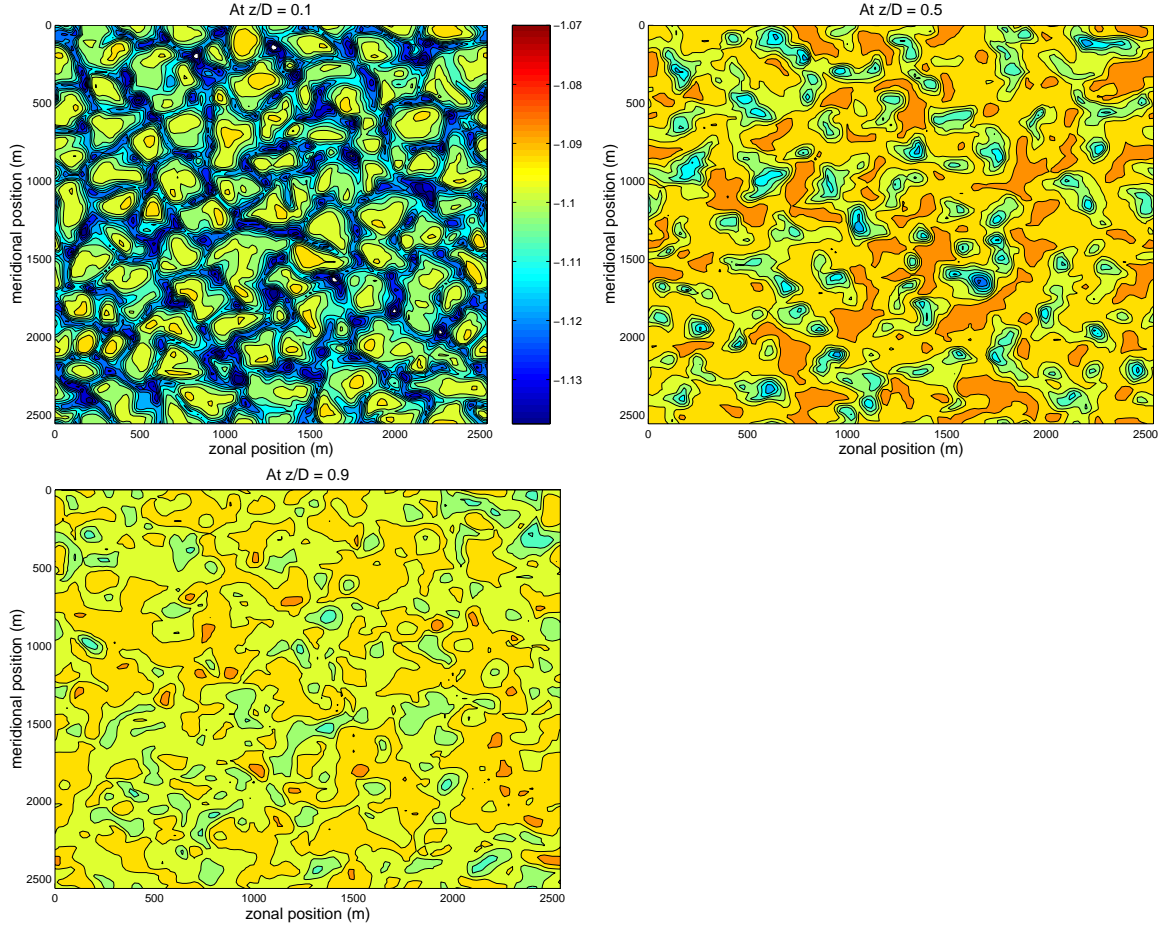


Figure 7.8: Cross-sections of temperature field in the $x-y$ -plane for run 'weak'. From left to right: at $z = 0.1D$, at $z = 0.5D$, and at $z = 0.9D$.

surrounded by cold sinking regions. The uprising warm regions are considerably larger in area. Continuity requires the sinking cold plumes (small area, high velocity) to be compensated by slowly rising warm water masses from below (large area, low velocity). This is to be compared with the flow fields of vertical velocity (Figures 7.11-7.13). The horizontal mean temperature is $-1.0959^{\circ}C$. Therefore, the colorbar indicates the strong asymmetry in the regions of sinking and rising water masses. In the middle of the mixed layer there are only few downward regions left. Still, the relatively warm regions are larger in area. At the outer edge of the mixed layer, the flow pattern is nearly homogeneous. The area is equally distributed between relatively warm and relatively cold water masses.

In Figure 7.9 it is readily visible that the dominating structure in run 'moderate' are cells. No transition to roll structures is visible although the velocity ratio $\Pi_* = 0.38$ appears to be large enough to expect the starting of transition according to atmospheric findings. The cells have broadened compared to the ones in run 'weak' and show a horizontal spacing on the order of $1.4 D$. However, no preferred direction of orientation is visible. The broadening of the structures indicates that the cell structures are influenced by local shear. The cell structure is strongly damped in the middle of the mixed layer. Convective activity is larger than in run 'weak'. The relatively warmer water masses are orientated at an angle of about 30° . At the outer edge of the mixed layer there is no cell structure left but still the temperature field is more inhomogeneous than in run 'weak'.

The transition to convective rolls is visible in Figure 7.10. As the velocity ratio in run 'strong' is $\Pi_* = 0.78$, the threshold value for roll formation might be estimated to be somewhere between 0.4 and 0.7. The roll orientation is in almost 90° to the wind direction with a roll spacing of roughly $1.7 D$. The depth $z/D=0.5$ corresponds to $105 m$ which is more than the Ekman depth $D_{ek} = \pi\sqrt{2\nu_t/f_z} = 80m$ with the eddy viscosity $\nu_t = 0.026u_*^2/f_z$ from Svensson (1979). The footprints of the convective rolls are clearly visible. Even at the outer edge of the mixed layer at a depth of $200 m$ the streaky structures indicate that the convective rolls have transported the wind's influence through the whole mixed layer. Thus, the wind influence manifesting in the roll structure is visible well below the Ekman layer.

In contrast to the temperature field, the field of vertical velocity becomes stronger with increasing surface distance. This is illustrated in the Figs. 7.11-7.13 where a sequence of views of the vertical velocity flow patterns at different depths are provided. They show the flow at the location $z/D= 0.1, 0.5$, and 0.9 for run 'weak', 'moderate' and 'strong', respectively. Contour intervals are $0.005 ms^{-1}$. Figure 7.11 displays a similar cell pattern near the surface as for the temperature field. However, the downward velocities are on the order of only $-0.01 ms^{-1}$. They are damped due to the presence of the rigid surface. The velocity of the downward elements increases in the middle of the mixed layer in which they reach their (negative) maximum of $-0.04 ms^{-1}$. At the outer edge of the mixed layer the coherent structures have broken up but still single downward elements reach

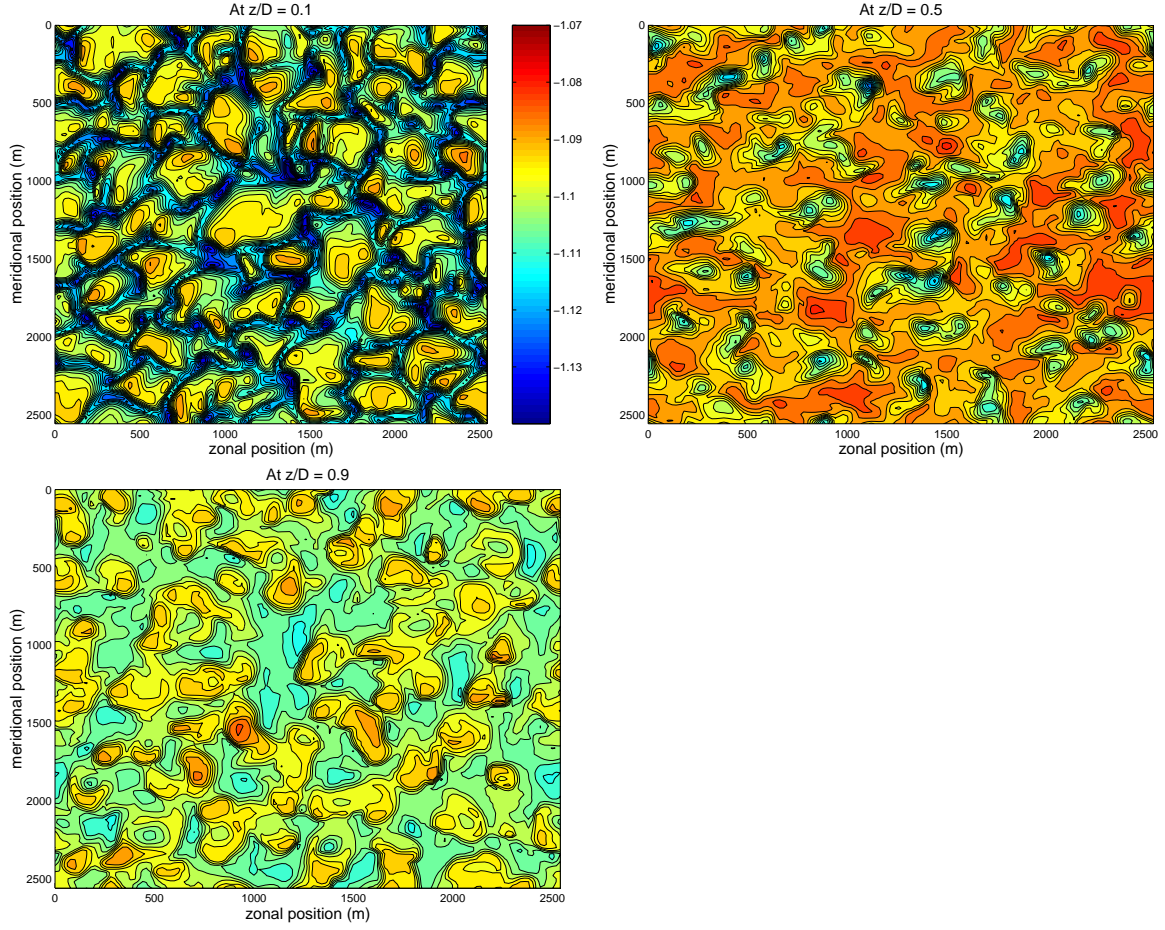


Figure 7.9: Cross-sections of temperature field in the $x - y$ -plane for run 'moderate'. From left to right: at $z = 0.1D$, at $z = 0.5D$, and at $z = 0.9D$. The colorbar coincides with the colorbar in 7.8.

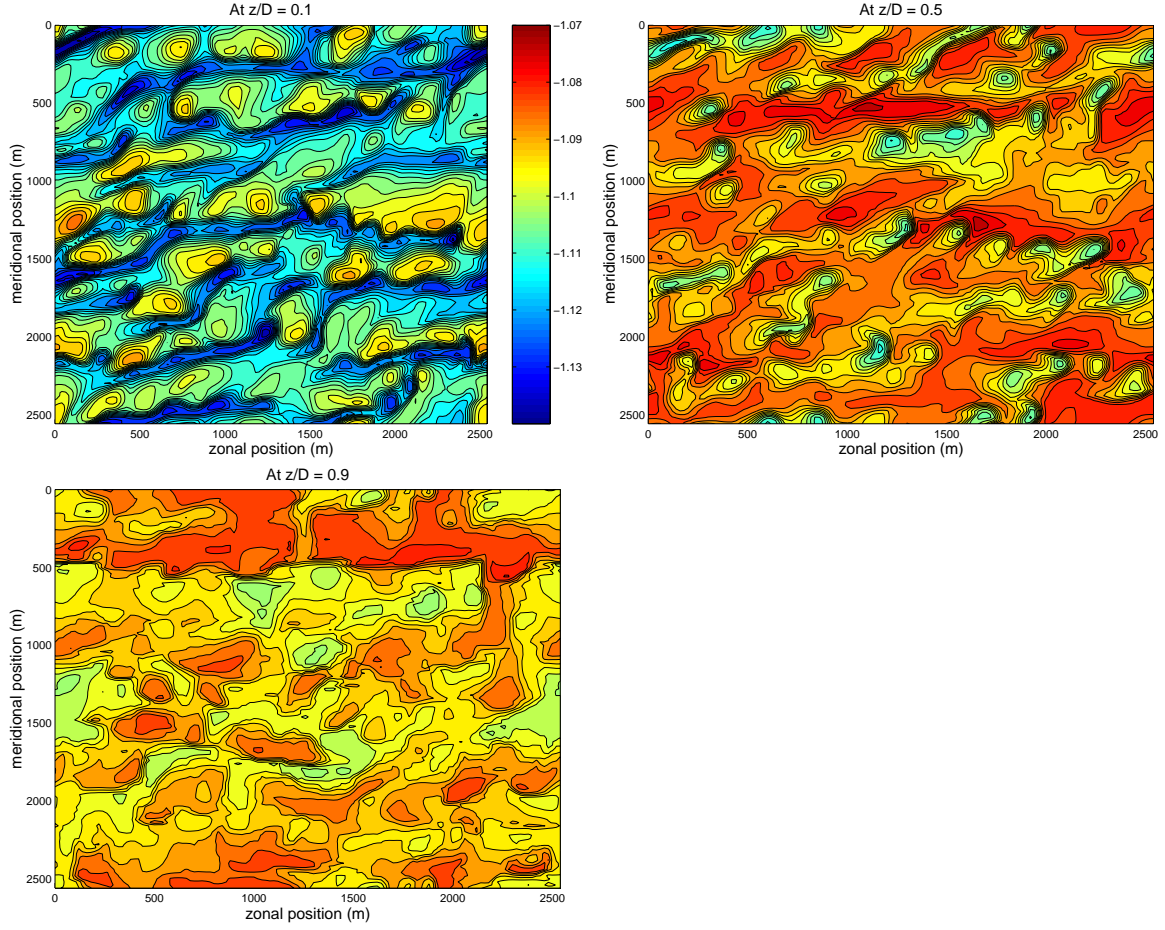


Figure 7.10: Cross-sections of temperature field in the $x - y$ -plane for run 'strong'. From left to right: at $z = 0.1D$, at $z = 0.5D$, and at $z = 0.9D$. The colorbar coincides with the colorbar in 7.8.

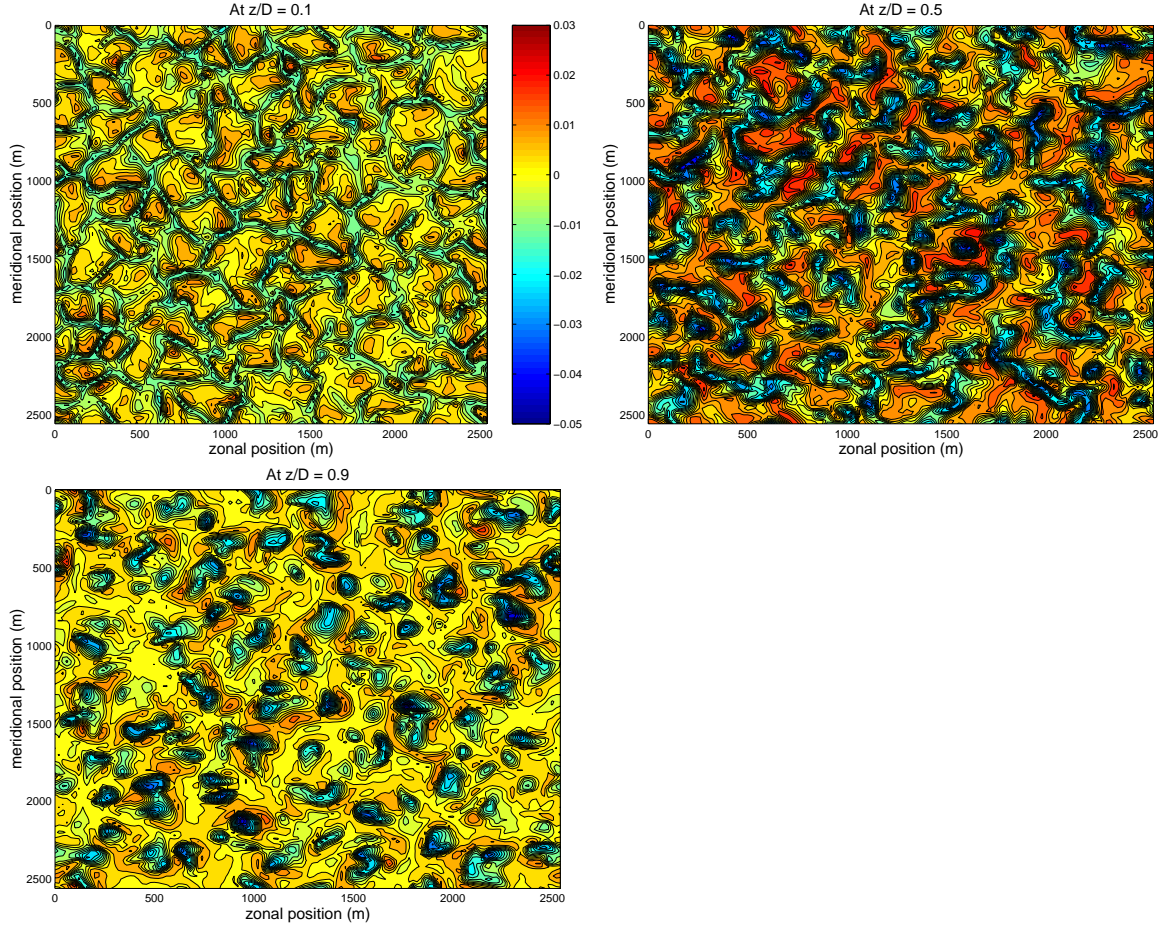


Figure 7.11: Cross-sections of vertical velocity field in the $x - y$ -plane for run 'weak'. From left to right: at $z = 0.1D$, at $z = 0.5D$, and at $z = 0.9D$.

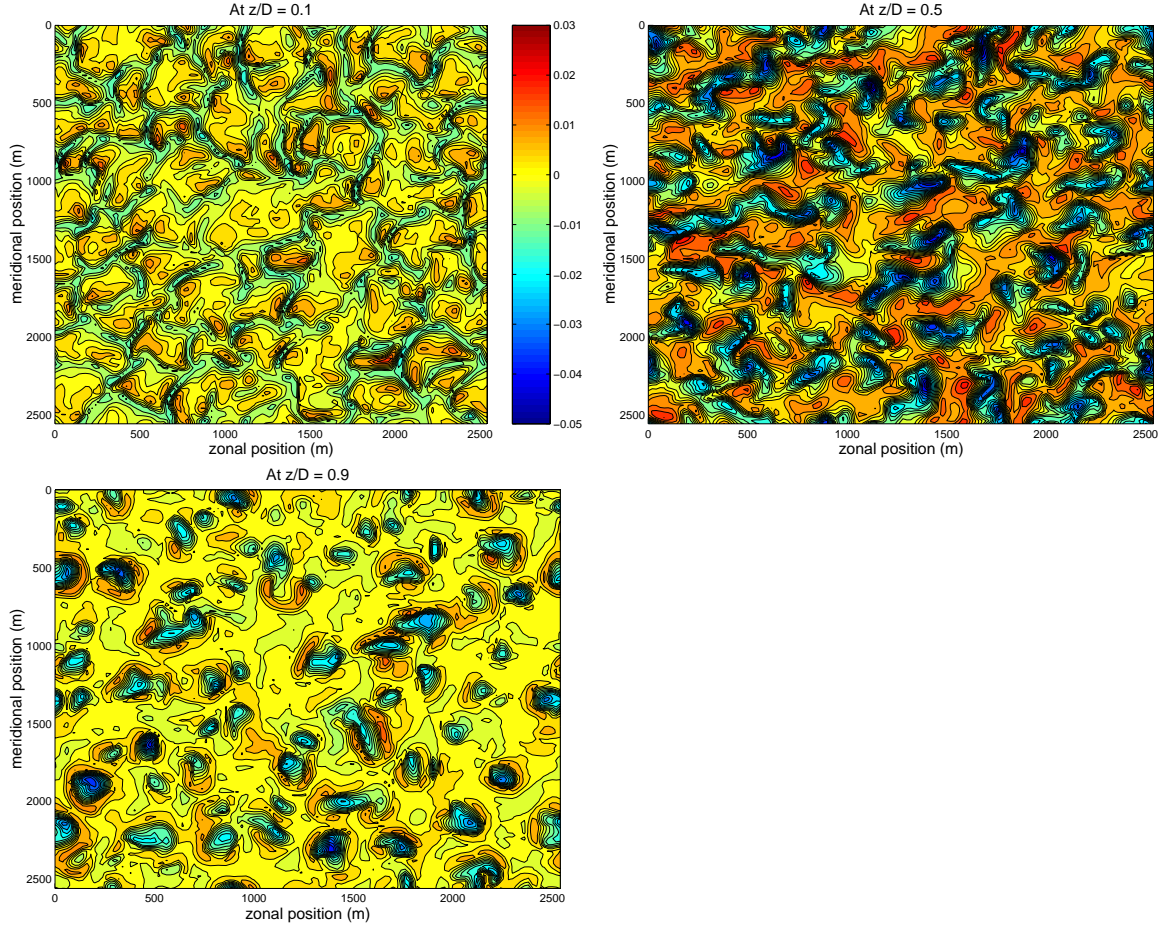


Figure 7.12: Cross-sections of vertical velocity field in the $x - y$ -plane for run 'moderate'. From left to right: at $z = 0.1D$, at $z = 0.5D$, and at $z = 0.9D$.

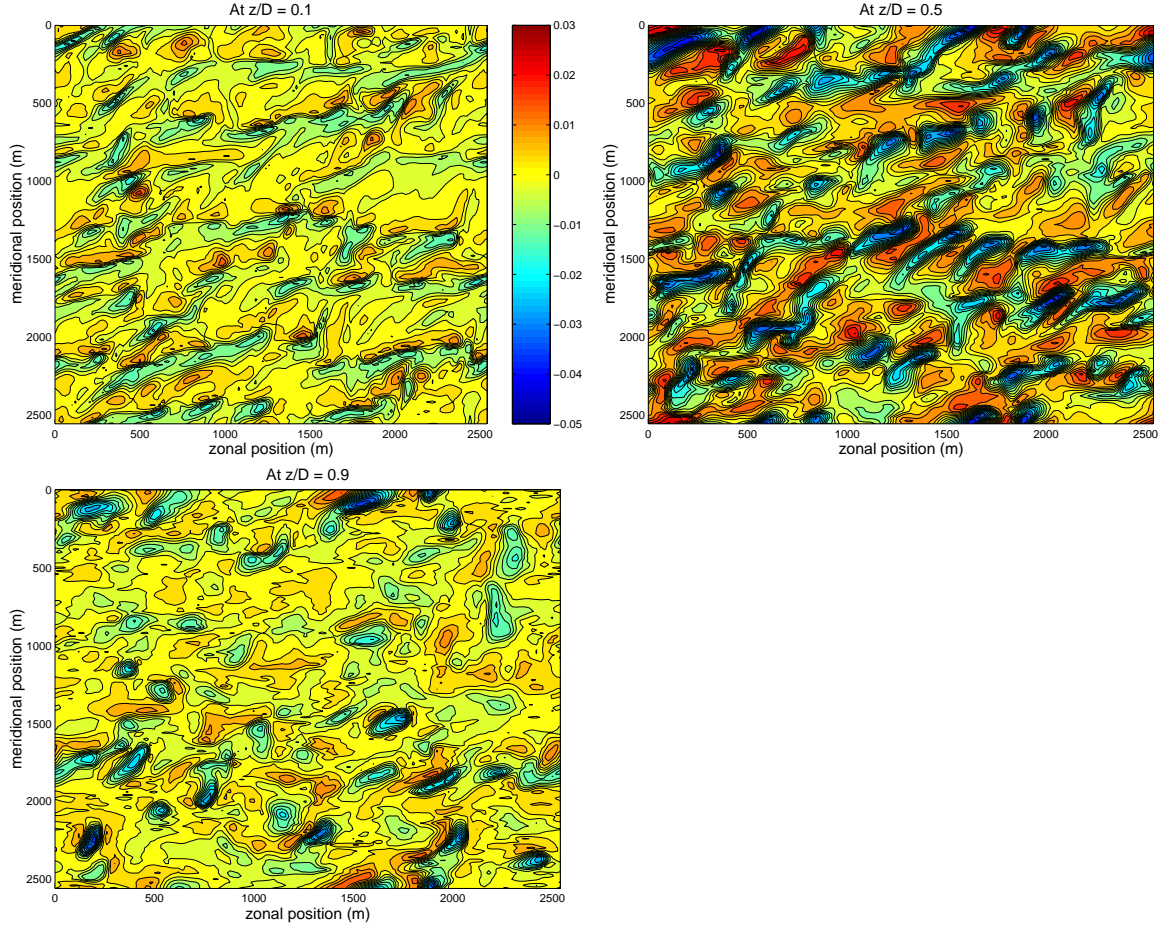


Figure 7.13: Cross-sections of vertical velocity field in the $x - y$ -plane for run 'strong'. From left to right: at $z = 0.1D$, at $z = 0.5D$, and at $z = 0.9D$.

large negative velocity.

For run 'moderate' (Fig 7.12), the near-surface values of vertical velocity are rather small as well and become stronger in the interior. The structures are more random than in run 'weak' near the surface but the differences become smaller in the bulk of the mixed layer. This is in consistency with the comparison of the figures 7.5 and 7.6. In the bulk of the mixed layer both flow fields are almost indistinguishable. At the outer edge of the mixed layer there are less convective structures left than in run 'weak'. This is probably due to small-scale mixing.

The mixing is even stronger at the mixed layer base of run 'strong' (Fig 7.13). However, run 'strong' exhibits a strong tendency to organize the convective structures in form of rolls. The angle between the roll structures and the wind direction is about 60° and is approximately constant throughout the mixed layer. This is a larger turning than expected from Ekman theory. Apparently, the turning angle represents an depth-averaged behaviour.

Although there is strong similarity between the instantaneous fields of vertical velocity and temperature fluctuations there are some striking differences. One is the fact that the vertical velocity vanishes at the surface and increases towards the middle of the mixed layer whereas the temperature fluctuations show their maximum at the very surface. Secondly, the vertical velocity field at the mixed layer base is relatively well-mixed in the runs 'moderate' and 'strong' compared to the field in run 'weak'. From Figure 7.2 it is recognized that in these two runs residues of the surface-induced velocity shear still shows up at the mixed layer base. As velocity shear enhances small-scale mixing it is obvious that shear is the mechanism by which the vertical velocity fields in the runs 'strong' and 'moderate' are smoother than in the run 'weak'. However, temperature fluctuations at the mixed layer base show a reversed picture: the stronger the shear the more pronounced are the footprints of the convective structures. One possible explanation is the presence of the counter-gradient flux which damps convective plumes since kinetic plumes energy is dissipated in order to erode the stable stratification underneath. From the instantaneous flow structures it is tempting to judge that the counter-gradient flux is largest for run 'weak'. This issue will be continued in the next section.

7.3 Mean variances and fluxes

For the following discussion the double prime denotes a deviation from the horizontal mean value written in brackets, e.g. $U'' = U - \langle U \rangle$ where U is the filtered (resolved) quantity. Later on, the filtered (resolved) quantity will be denoted \overline{U} and a distinction between U and \overline{U} will be required. However, in this section the former notation is sufficient.

The vertical profiles of the vertical heat flux $\langle W'' T'' \rangle = \langle \overline{W''} \overline{T''} \rangle + \langle \overline{w\theta} \rangle$

are plotted in Figure 7.14. The SGS contributions are represented by dashed lines whereas the solid lines represent the sum of resolved-scale and SGS contributions. The numerical data are to be compared with the schematic picture 5.1 which forms the foundation of mixed layer bulk modeling. The assumption of a linear decrease is well confirmed by Figure 7.14. The little kink at the very surface might indicate that the flow is not perfectly adjusted to the upper boundary condition. For further comparison, results from the water tank experiments by Deardorff and Willis (1985) are displayed in Figure 7.14. The open circles represent their data points while the solid line is a polynomial fitting curve. The linear decrease is found for the experimental heat flux as well.

As the resolved vertical velocity vanishes at the surface, the resolved-scale contributions of the heat flux at the surface vanish accordingly. The total heat flux at the surface is purely made of the SGS contribution $\overline{w\theta}$. The surface value of $\overline{w\theta}$ is prescribed as Q_0 . Therefore, in all the three runs, the profiles start at unity. The SGS contributions become smaller with increasing depth. Whether the flow has approximately reached a steady-state can be checked in the following way. Assuming that the temperature profile is mainly driven by vertical diffusion results in

$$\frac{\partial T}{\partial t} = -\frac{\partial Q}{\partial z}.$$

Taking the vertical derivative of this expression results in

$$\frac{\partial}{\partial t} \left(\frac{\partial T}{\partial z} \right) = -\frac{\partial}{\partial z} \left(\frac{\partial Q}{\partial z} \right),$$

where the order of t and z derivatives was changed. For stationarity, $\partial(\partial T/\partial z)/\partial t \sim 0$. This implies that the vertical heat flux is linear in z . The profiles in Figure 7.14 are close to linear indicating stationarity for all three runs. In the entrainment zone the profiles become negative due to the 'countergradient flux'. Since the thermocline acts like a (permeable) wall, one might expect the formation of some kind of boundary layer which might be broadened due to increasing shear. Unfortunately, the resolution is not fine enough to detect significant differences between the three runs. It is not clear whether the stratification is strong enough to show remarkable 'blocking' effects. In contrast, the entrainment zone in the experiments by Deardorff and Willis (1985) is significantly narrower than in the three model runs. This fact might be a hint that the entrainment zone in the runs is broadened due to numerical diffusion. This issue will be addressed in further detail in Section 7.6. According to Figure 5.1, one can find the entrainment buoyancy flux B_h from (5.2.2) as the linear extrapolation of the heat flux profile to the depth $z/D = 1$. The entrainment coefficient A introduced in equation (5.3.1) relates entrainment and surface buoyancy flux. For 'weak', $A \approx 0.23$ is found whereas for 'moderate' $A \approx 0.20$ and for the 'strong' case A is approximately 0.26. In contrast, the value of 0.2 is frequently reported in the literature (Zilitinkevich 1991). No clear trend with increasing shear can be

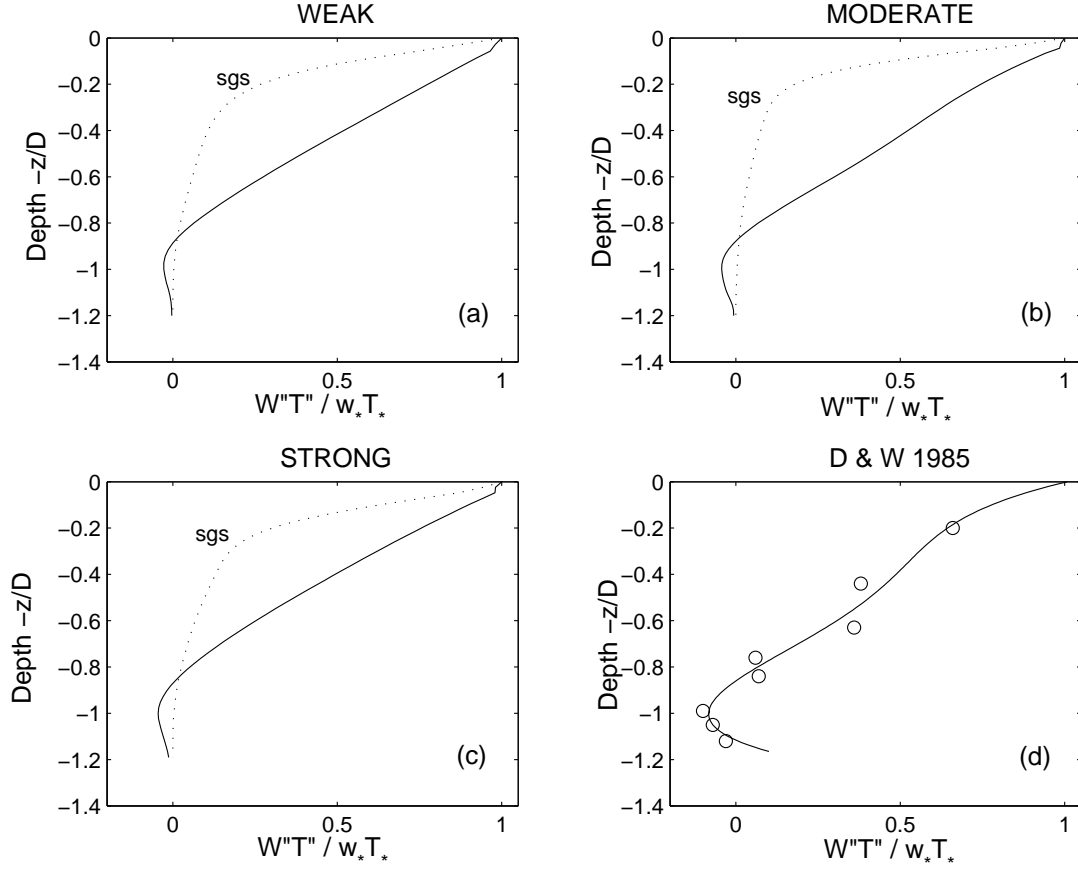


Figure 7.14: Vertical distributions of the vertical heat flux. The LES results for runs 'weak', 'moderate' and 'strong' are displayed, respectively. Dashed lines represent the SGS contribution while solid lines depict the sum of resolved-scale and SGS parts, respectively. For comparison, results from laboratory experiments by Deardorff and Willis (1985) (open circles) are shown. The solid line represents a polynomial fitting to the data points of Deardorff and Willis (1985).

Run	$D(m)$	$\Delta T(K)$	$Q_0(Kms^{-1})$	Nu	Ra
WEAK	220	$2.4 \cdot 10^{-2}$	$1.55 \cdot 10^{-4}$	$1.0 \cdot 10^7$	$4.5 \cdot 10^{14}$
MODERATE	225	$2.7 \cdot 10^{-2}$	$1.55 \cdot 10^{-4}$	$9.2 \cdot 10^6$	$5.4 \cdot 10^{14}$
STRONG	210	$3.6 \cdot 10^{-2}$	$1.55 \cdot 10^{-4}$	$6.5 \cdot 10^6$	$5.8 \cdot 10^{14}$

Table 7.3: Governing parameters for the three runs. Nu is the surface Nusselt number, Ra is the Rayleigh number.

deduced from these values.

The non-dimensional heat flux is described by the Nusselt number Nu which is the ratio of the actual heat transport to the purely diffusive flux due to molecular conduction,

$$Nu = \frac{Q_0}{\chi_{mol} \Delta T / D}$$

where χ_{mol} is the molecular diffusivity of water and ΔT is the temperature difference between the surface and the bulk of the mixed layer. The results are listed in table 7.3 along with the Rayleigh number

$$Ra = \frac{g \alpha \Delta T D^3}{\nu_{mol} \chi_{mol}}.$$

They indicate that the heat transfer is reduced with increasing shear. Apparently, small-scale mixing due to mean shear enhances turbulent heat conduction, thus reducing the efficiency of convection.

In summary, with the same heat flux given mean shear reduces the heat transport. No effect of the presence of mean shear on the entrainment efficiency is found which may be due to insufficient resolution. The vertical profile of the components of vertical momentum flux is displayed in Figure 7.15. The SGS contributions of $\langle V''W'' \rangle$ is represented by the dashed blue line whereas the solid blue line represents the sum of resolved-scale and SGS contribution. The SGS contribution of $\langle U''W'' \rangle$ is not shown here as it is two orders of magnitude smaller than the resolved portion. It is evident from all the three runs that this is in contrast to the meridional component $\langle V''W'' \rangle$ which is almost entirely made of its SGS portion. This fact can be explained by the upper boundary condition: The transfer of momentum from the atmosphere to the ocean is parameterised by turbulent diffusion, i.e. by SGS motion, as from $W = 0$ at the very surface it follows that the *resolved* momentum fluxes $\langle V''W'' \rangle_{res}, \langle U''W'' \rangle_{res}$ vanish accordingly. The wind stress vector $\vec{\tau}$ is given by $\vec{\tau} = (0, \tau_y)$ since the wind blows in meridional direction. Hence, at the very surface $\langle V''W'' \rangle_{SGS} = -u_*^2$ and $\langle U''W'' \rangle_{SGS} = 0$. It can be seen that the momentum flux enters the ocean by SGS diffusion through the meridional component and is then transferred to the zonal component. The LES results are contrasted with the initial momentum fluxes which are derived from the Ekman balance with constant eddy viscosity.

The Ekman solution for the momentum fluxes (see Chapter 2) reads

$$\begin{aligned}\langle U''W'' \rangle &= -\nu_t \frac{\partial U^{ek}}{\partial z} = \frac{\nu_t}{\delta} (V^{ek} - U^{ek}), \\ \langle V''W'' \rangle &= -\nu_t \frac{\partial V^{ek}}{\partial z} = -\frac{\nu_t}{\delta} (U^{ek} + V^{ek}).\end{aligned}$$

and is depicted in Figure 7.16. Only the upper part of the mixed layer is displayed in this figure since the dynamics is restricted to the Ekman layer. Differences between the final and the initial profiles are entirely due to the unstable heat flux. For the runs 'moderate' and 'strong' the momentum profiles have been distributed over the whole mixed layer instead of being restricted close to the surface. The profiles of both components have been broadened significantly. Additionally, the maximum value of the zonal component has approximately doubled during the simulation. Apparently, in the runs 'moderate' and 'strong' the dynamics is largely determined by the wind stress. In contrast, in run 'weak' the momentum profiles are not determined by the wind stress. Instead, the maximum value of the momentum flux is three times larger than the surface flux. This fact reveals that large momentum fluxes can be generated by convective motion itself.

In Figure 7.17 (a)- (c), the vertical velocity variances $\langle W''^2 \rangle = \langle \overline{W''^2} \rangle + \langle \overline{w^2} \rangle$ are shown against nondimensional depth. Figure 7.17 (d) displays results from the laboratory experiments by Deardorff and Willis (1985). Again, the open circles denote their data points and the solid line is a polynomial fitting curve. The dashed line in Figure 7.17 (d) represents an interpolation curve deduced from various atmospheric measurements by Lenschow et al. (1980) which reads $\langle W''^2 \rangle / w_*^2 = 1.8(z/D)^{2/3}(1 - 0.8z/D)^2$. Here the resolved parts are drawn by dashed lines since the SGS contribution $\overline{w^2}$ had to be estimated. This was done in the following way. In the interior where the unresolved scales are nearly isotropic, $\overline{w^2} \approx 2e/3$. In contrast, $\overline{w^2} = 0$ at the surface is prescribed. The SGS profile is interpolated linearly to match the surface and the interior estimation. The profiles are parabolic in shape with a peak at a depth of $z/D \approx 0.4$ for the runs 'weak' and 'moderate' while the 'strong' case has its peak at about $0.3 D$. The peak value of the resolved variance is almost the same of about $0.35 w_*^2$. Some differences are due to the SGS contribution which makes the variance in case 'strong' the largest one and the variance in case 'weak' the smallest one. Thus the SGS variances are influenced by shear. However, the difference is only about 10 percent. While the shape of the profiles and the positions of the peak value agree with the laboratory results of Deardorff and Willis (1985) the peak values are considerably larger. In contrast, the peak of the atmospheric measurements by Lenschow et al. (1980) is in closer agreement to the LES data. In addition, compared to the Deardorff and Willis (1985) results, the peak value of the Lenschow et al. (1980) data is closer to the surface which might indicate the presence of shear: the movement of the peak value towards the surface with increasing shear was e. g. reported by Moeng and Sullivan (1994) in their LES

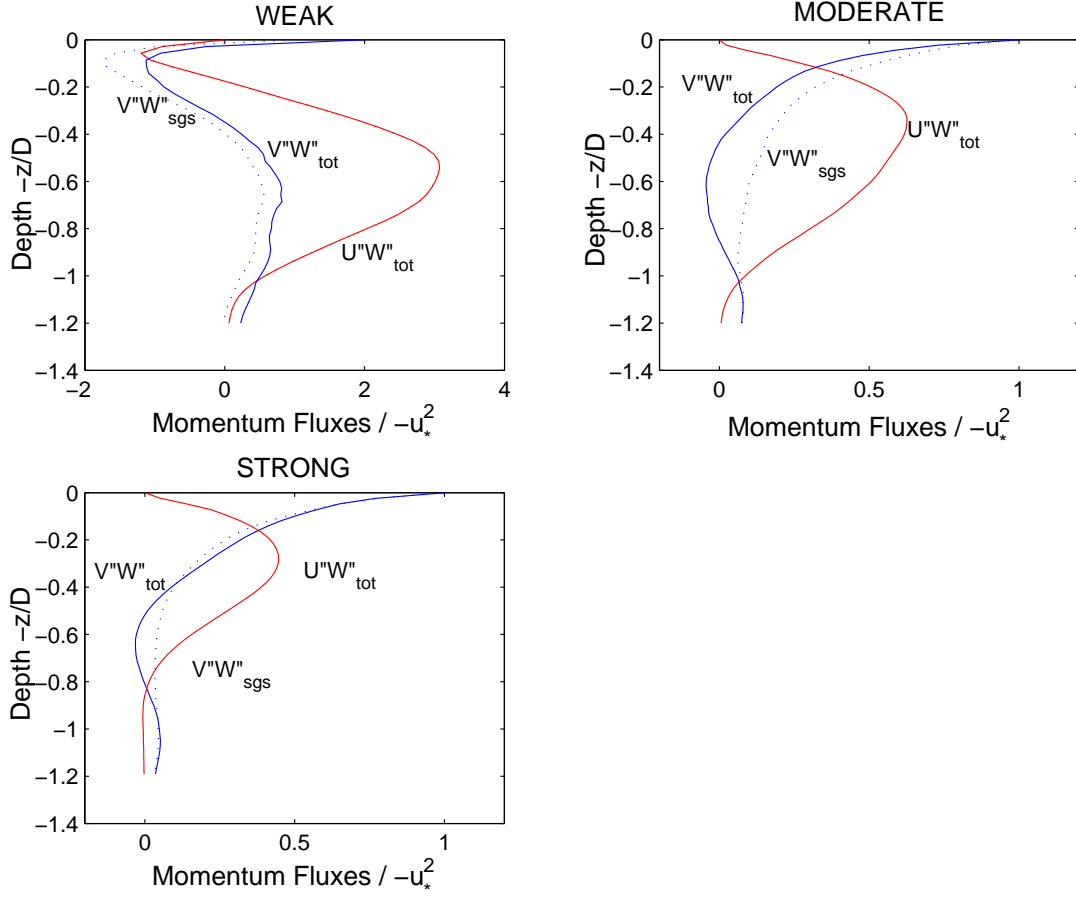


Figure 7.15: Vertical distributions of the vertical momentum flux. The LES results for runs 'weak', 'moderate' and 'strong' are displayed, respectively. Dashed blue lines represent the SGS contribution of $\langle V''W'' \rangle$ while solid blue lines depict the sum of resolved-scale and SGS parts, respectively. For the zonal component $\langle U''W'' \rangle$ only the sum is drawn (red lines) since the SGS contribution is much smaller.

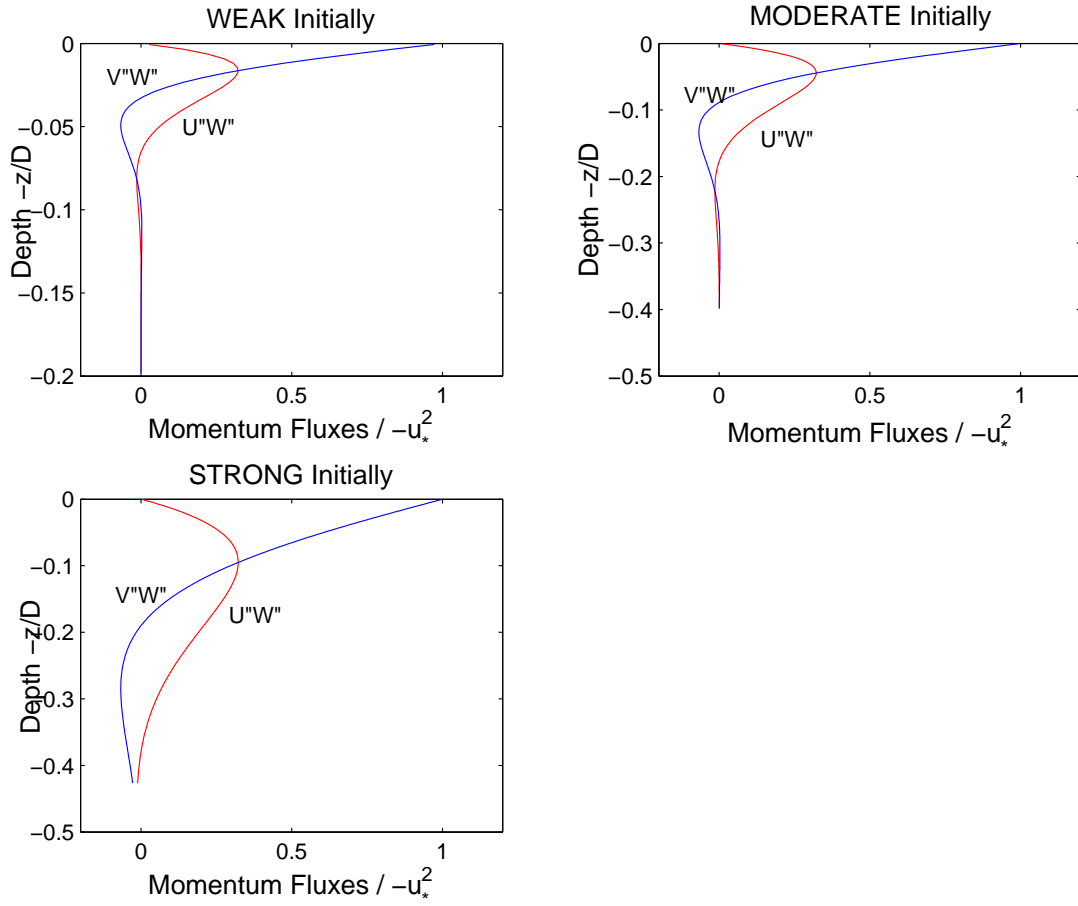


Figure 7.16: Vertical distributions of the vertical momentum flux for the initial flow fields. The analytic results from Ekman theory for runs 'weak', 'moderate' and 'strong' are displayed, respectively. Note the distinct range of the vertical axes.

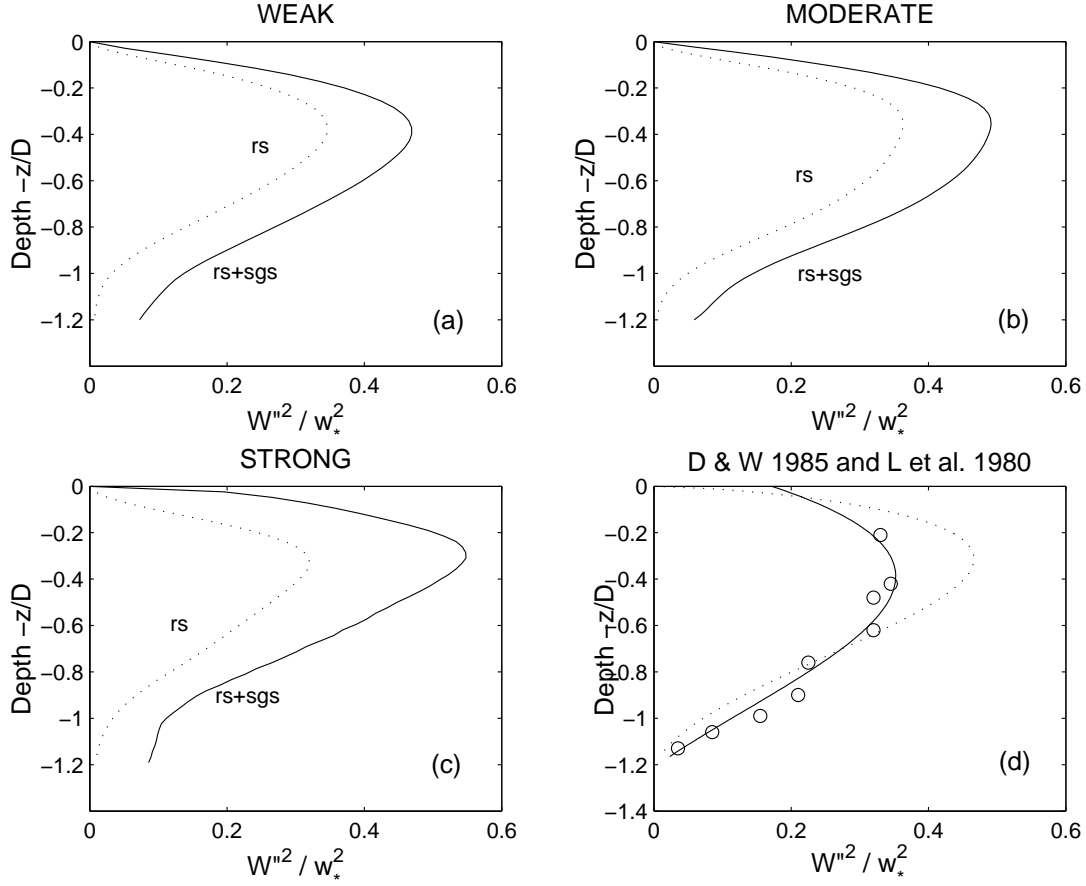


Figure 7.17: Vertical distributions of the vertical velocity variance. The LES results for runs 'weak', 'moderate' and 'strong' are displayed, respectively. Dotted lines represent the resolved-scale contribution while solid lines depict the sum of resolved-scale and SGS parts, respectively. For comparison, Figure (d) displays results from laboratory experiments by Deardorff and Willis (1985) (open circles) and from aircraft measurements by Lenschow et al. (1980). The dotted line represents the interpolation curve proposed by Lenschow et al. (1980). The solid line represents a polynomial fitting to the data points of Deardorff and Willis (1985).

data of convective shear flows and is confirmed by the present LES results. Below the mixed layer, the variance rapidly tends to zero.

The vertical profile of the temperature variance is shown in Figure 7.18. Temperature variance is produced by the interplay of heat flux and temperature gradient. It is visible that the SGS contributions clearly dominate over the resolved-scale variance (dotted lines). This undesirable behavior improves with increasing shear with acts to broaden the thermal boundary layer. Note that run 'moderate' gives higher values of temperature variance than run 'strong'. The agreement with the tank data of Deardorff and Willis (1985) which are displayed in (d) is not very well. However, the LES data agree much better with the interpolation curve which Kaimal et al. (1976) proposed for their atmospheric measurements of temperature variance, $\langle T''^2 \rangle / T_*^2 = 1.8(z/D)^{2/3}$. An explanation might be that at least slightly sheared conditions (as in the field measurements) enhance temperature variance. The second maximum in the entrainment zone is small for the LES data. This might again be related to unwarranted numerical diffusion. Higher values have been reported by Schmidt and Schumann (1989). Unfortunately, Moeng and Sullivan (1994) did not publish temperature variance for their LES of sheared convective flows. Third-order moments enter the budget equations for the second-order moments. In Figure 7.19, some of the third-order moments and how they alter with increasing shear are illustrated. The dashed-dotted line represents run 'weak' while dotted and solid lines represent runs 'moderate' and 'strong', respectively. Note that only the resolved-scale part of the third-order moments is available from the present LES model since the SGS third-order moments are neglected. From (7.5.2) it will be seen that the vertical derivatives of $\langle \overline{W}''^3 \rangle$ and $\langle \overline{W}'' \overline{U}''^2 \rangle$ enter the budget equation of turbulent kinetic energy via turbulent transport term (III). While $\langle \overline{W}''^3 \rangle$ can be viewed as the vertical flux of vertical velocity variance, $\langle \overline{W}'' \overline{U}''^2 \rangle$ represents the corresponding vertical flux of zonal velocity variance. Both fluxes are shown in (a) and (b), respectively. In run 'weak', $\langle \overline{W}''^3 \rangle$ exceeds $\langle \overline{W}'' \overline{U}''^2 \rangle$ by one order of magnitude. It increases linearly down to about $0.6D$, reaching a maximum of about $0.17 w_*^3$ in the bulk of the mixed layer. This is a well-known feature of free convection (e.g., Schmidt and Schumann 1989). It can be inferred from Figures 7.17 and 7.20 that with increasing shear the vertical fluctuations are slightly damped while the horizontal fluctuations are strongly enhanced. The corresponding vertical fluxes behave in the same manner: increasing shear damps the vertical fluctuations while enhancing the horizontal ones. Again, as for the vertical velocity variance the peak value is shifted towards the surface with increasing shear. In Figure (c) and (d), the vertical flux of heat flux $\langle \overline{W}''^2 \overline{T}'' \rangle$ and the vertical flux of temperature variance $\langle \overline{W}'' \overline{T}''^2 \rangle$ are shown. Figure (c) shows again that vertical motion is damped by increasing shear: $\langle \overline{W}''^2 \overline{T}'' \rangle$ and $\langle \overline{W}'' \overline{T}''^2 \rangle$ are largest for run 'weak'. However, the smallest peak value results for run 'moderate'. The vertical flux changes sign at the outer edge of the mixed

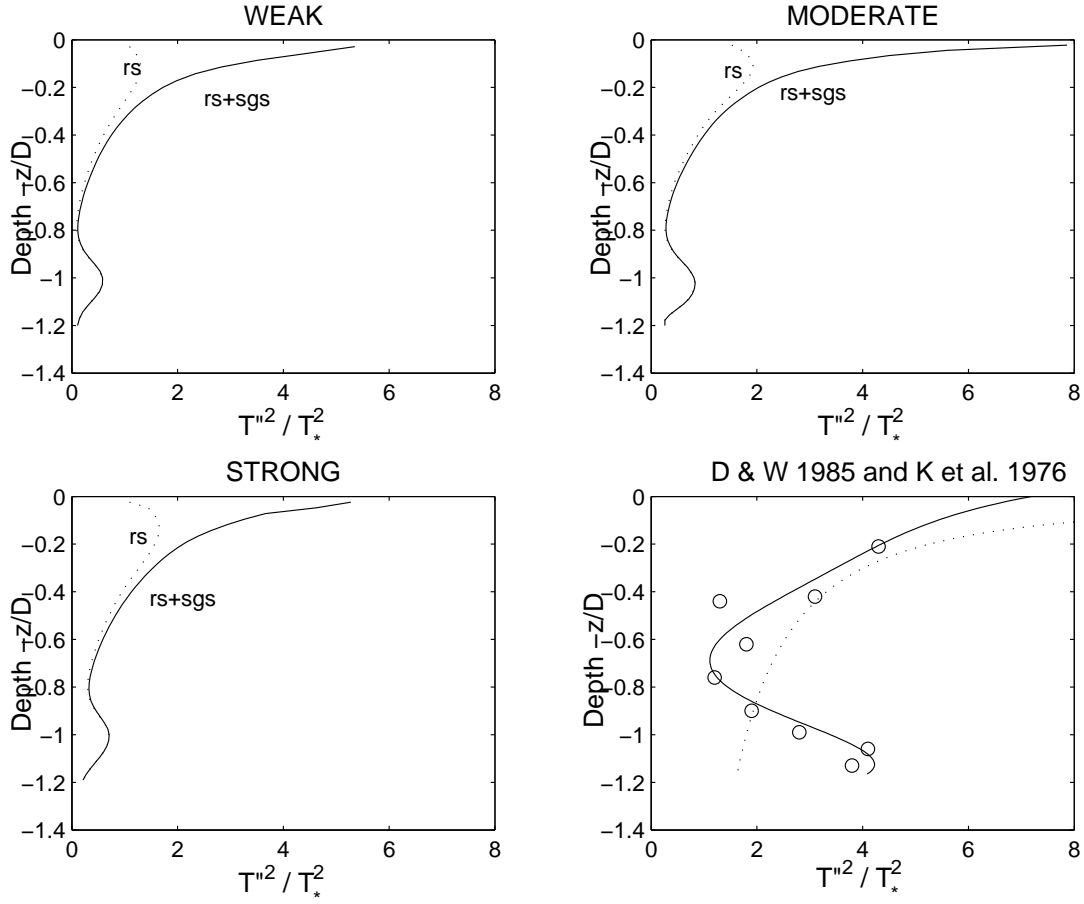


Figure 7.18: Vertical distributions of the temperature variance. The LES results for runs 'weak', 'moderate' and 'strong' are displayed in Figures (a), (b) and (c), respectively. Dotted lines represent the resolved-scale contribution while solid lines depict the sum of resolved-scale and SGS parts, respectively. For comparison, Figure (d) displays results from laboratory experiments by Deardorff and Willis (1985) (open circles) and from field measurements by Kaimal et al. (1976). The dotted line represents the interpolation curve proposed by Kaimal et al. (1976). The solid line represents a polynomial fitting to the data points of Deardorff and Willis (1985).

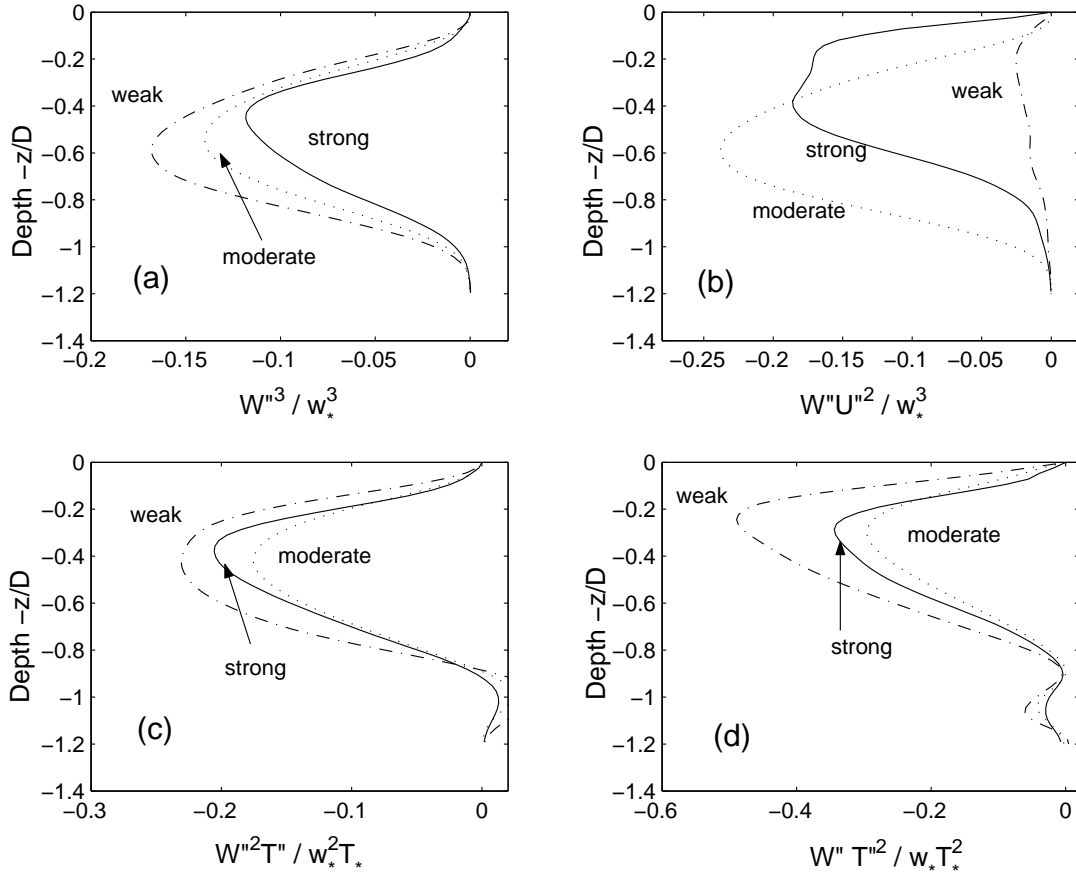


Figure 7.19: Vertical distributions of various third-order moments. The dashed-dotted, dotted and solid lines depict the runs 'weak', 'moderate' and 'strong', respectively. Only resolved-scale contributions are shown.

layer where the direction of transport is reversed ('counter-gradient flux'). In Figure 7.20, the variances of the horizontal components of velocity are displayed. In purely bouyant driven flows the horizontal components of velocity gain turbulent kinetic energy solely by pressure redistribution whereas the energy is directly fed into the vertical component. In bouyant shear flows there is another mechanism to drive the horizontal components, namely the shear. The highest values of horizontal velocity fluctuations are observed in the surface region where the turbulent kinetic energy is entirely distributed between the meridional and the zonal component since $\overline{w^2} = 0$. Here, turbulent kinetic energy is predominantly produced by shear. All the profiles are similar in the way that they exhibit more or less a four-layer 'S'-like structure: the surface region (which broadens with increasing shear), a mixed-layer region in which the gradient is small, an entrainment region with pronounced gradient, and finally a constant layer underneath. In the bulk of the mixed layer the velocities are very small due to effective mixing of the bouyant plumes. Although the laboratory results of Deardorff and Willis (1985) exhibit large scatter (Figure 7.20 (d)) there is satisfactory agreement for run 'weak'. Both horizontal components are similar for all the three runs. While near the surface this is expected from Ekman theory (as the wind blows in meridional direction), in the bulk of the mixed layer the components are well-mixed due to the convective plumes. Results from the LES of atmospheric sheared convection by Moeng and Sullivan (1994) are shown along with the Deardorff and Willis (1985) findings. The wind in this LES blows in meridional direction. This shows up in enhanced meridional variance (red asteriks) compared to zonal variance (blue asteriks). This contrasts findings from the runs 'moderate' and 'strong' which show approximate horizontal isotropy. Probably, the effect of Earth's rotation is strong enough to completely redistribute variance horizontally in the oceanic case whereas it fails to homogenize horizontal variance in the atmospheric case. However, note the strong disparity of the corresponding velocity axes for the three model runs. It reflects the fact that especially near the surface the Deardorff velocity w_* is not the appropriate velocity scale to make the three profiles self-similar.

7.4 Velocity Scales

It is obvious from Figure 7.20 that scaling with w_* cannot account for the shear generated turbulence which causes the large horizontal velocity variance. It might be tempting to use the friction velocity u_* as appropriate surface scale, instead. This analysis is illustrated in Figure 7.21 (a) and (c) for both the variances of vertical and of meridional velocity. Profiles of run 'weak' have been skipped from Figure 7.21 (a) and (c). Those profiles become very much larger than the ones of runs 'moderate' (dotted line) and 'strong' (solid line). Apparently, the velocity

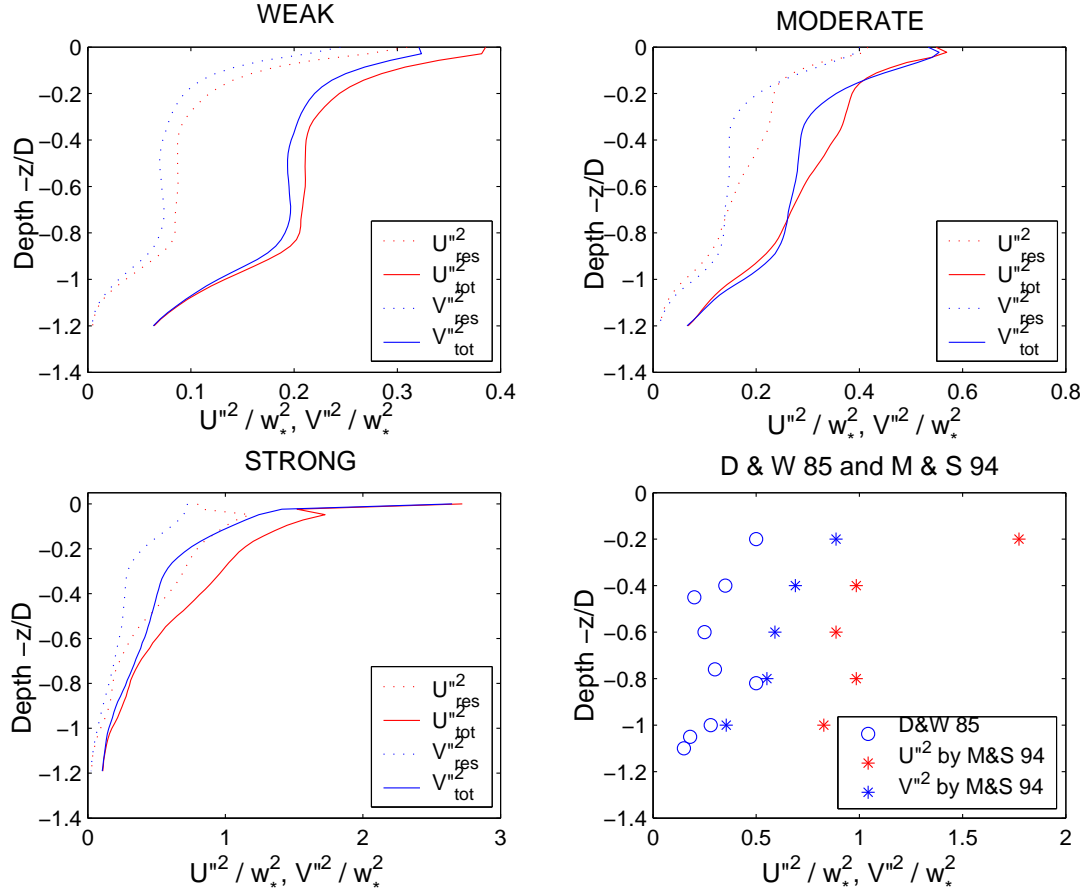


Figure 7.20: Vertical distributions of the horizontal velocity variances. The LES results for runs 'weak', 'moderate' and 'strong' are displayed in Figures (a), (b) and (c), respectively. Dotted lines represent the resolved contribution for the zonal (red lines) and the meridional components (blue lines) while solid lines depict the sum of resolved-scale and SGS parts, respectively. Note the distinct velocity axes. For comparison, Figure (d) displays results from laboratory experiments by Deardorff and Willis (1985) (open circles) and from LES by Moeng and Sullivan (1994) (asterisks). The blue and red asterisks denote their meridional and zonal components, respectively.

variances in run 'weak' do not scale with friction velocity at all. The problem of the appropriate velocity scale for sheared convective flow has been discussed in Moeng and Sullivan (1994). For their atmospheric LES results, the authors developed the velocity scale w_m which is a combination of Deardorff velocity w_* and surface friction velocity u_* . It is taken as

$$w_m^3 = w_*^3 + 5u_*^3. \quad (7.4.1)$$

Moeng and Sullivan (1994) could successfully scale the profiles of velocity variances with w_m . This means that the profiles of the sheared convective flows were found to lie between the profiles of their free convective and their neutral sheared flow.

The Moeng and Sullivan (1994) velocity scale has been tested for the present LES results. The profiles of velocity variances nondimensionalised by w_m are shown in Figure 7.21 (b) and (d). The results for scaling with u_* (in (a) and (c)) and with w_m (in (b) and (d)) are to be compared with the profiles from 7.17 and 7.20 which were scaled with the Deardorff velocity w_* . Hence, there are three velocity scales available; w_* which cannot account for shear effects by definition, u_* which cannot account for buoyancy effects by definition, and w_m which represents a combination of both. It can be inferred from Figures (a) and (b) that neither u_* nor w_m forms the appropriate velocity scale to make the profiles of vertical velocity variance self-similar. In contrast, the profiles from Figure 7.17 indicated that w_* is a better velocity scale. Figure 7.21 (c) reveals that u_* scales the near-surface flow of the meridional velocity variance in a correct manner, at least for the runs 'moderate' and 'strong'. Apparently, buoyancy plays a minor role here. This fact suggests that near the surface, the flows in 'moderate' and 'strong' resemble shear flow. However, in the interior, w_m orders the profiles in a proper manner, see (d). Here, the interaction of shear and buoyancy is apparently the dominant mechanism. In contrast, w_m fails to scale the near-surface flow.

It is obvious that none of the three velocities w_* , u_* , w_m is an unique velocity scale for sheared convective flow. The failure of w_m which was appropriate for the Moeng and Sullivan (1994) LES data of sheared convection suggests the following view. The velocity scale w_m constructed according to equation (7.4.1) is tailored for atmospheric results. The combination of w_* and u_* is chosen to be independent of height (or of depth), i.e., w_* was assumed to be the appropriate velocity scale for buoyant effects throughout the mixed layer while u_* was assumed to be the appropriate velocity scale for shear effects throughout the mixed layer. It seems likely that the first assumption will hold in the present study as well. In contrast, the second assumption might be erroneous. The effect of u_* only reaches a small portion of the mixed layer. Figure 7.15 shows that the momentum flux is determined by u_* only at the very surface and strongly decreases due to Earth's rotation. It is for this reason that the atmospheric similarity theory by Monin and Obukhov is of little use here: the Monin-Obukhov length only applies in the surface layer in which the fluxes are assumed to be constant. From Figure 7.15 it

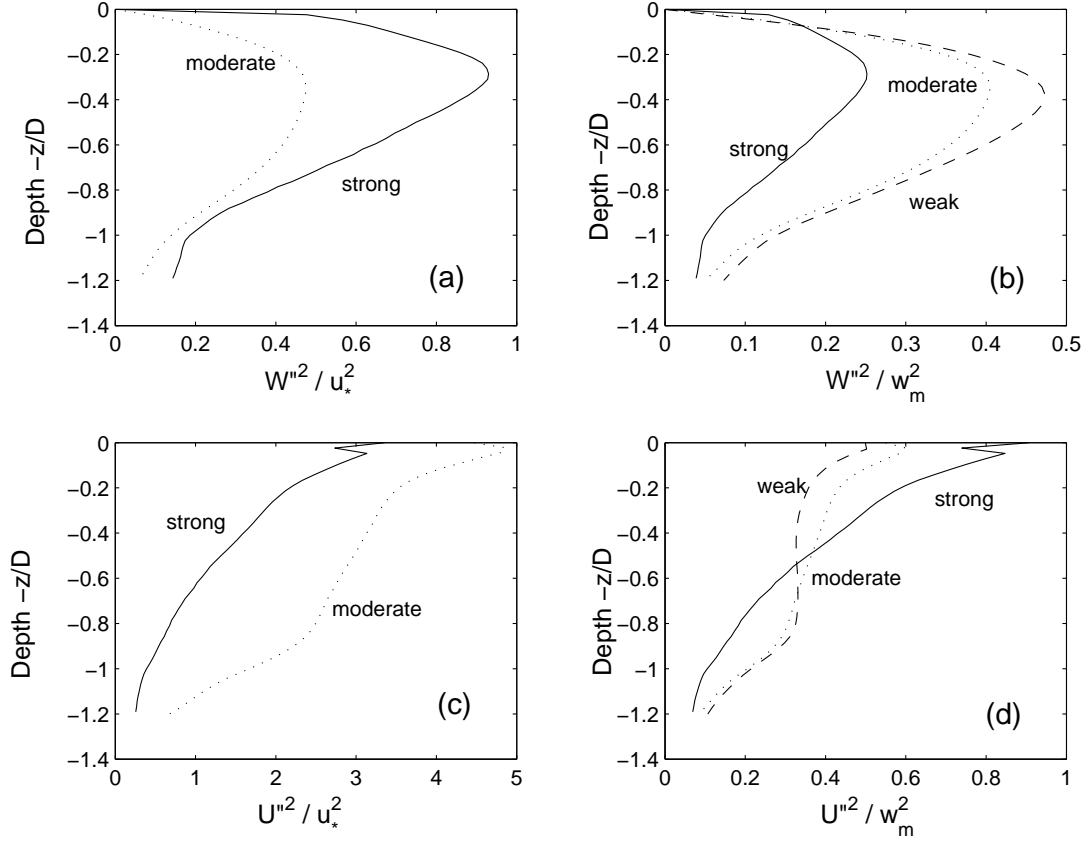


Figure 7.21: Different velocity scaling for the velocity variances. The dashed, dotted and solid lines depict results of the runs 'weak' (only (b) and (d)), 'moderate' and 'strong', respectively. In (a) and (c), the profiles are nondimensionalised by the corresponding friction velocity. Results from run 'weak' are not shown in (a) and (c). In (b) and (d), the profiles are nondimensionalised by the corresponding velocity scale according to (7.4.1), proposed by Moeng and Sullivan (1994).

is obvious that the momentum flux is not constant but rapidly decreasing away from the surface.¹

The correct velocity scaling should take into account that shear convective flows exhibit hybrid behaviour in that they behave similar to a shear flow close to the surface but like a free convective flow in the bulk of the mixed layer with some kind of transition inbetween. Hence, the velocity scale has to be depth-dependent taking into account the quasi-Ekman spiral. In future work, it will be attempted to define a depth-dependent velocity scale for shear effects and to combine this scale with w_* to hopefully give an appropriate velocity scale for sheared convective flows. In atmospheric research a promising approach has been started in the modified Monin-Obukhov similarity theory proposed by Zilitinkevich (1971) and Betchov and Yaglom (1971). According to this theory of 'directional dimensional analysis', within an unstable stratified boundary layer there are three distinct sublayers where turbulence structure is self-preserving and obeys rather simple power laws. This allows to separate horizontal and vertical motions. Further details can be found in the papers by Zilitinkevich (1973), Kader et al. (1989), Kader and Yaglom (1990) or Zilitinkevich (1994). However, it seems that at present there is no obvious way how to connect the three sublayers in a physical manner (Mironov, priv. commun.).

7.5 Turbulent kinetic energy

In order to gain insight into the driving mechanism of the sheared convective flow, the budget of the turbulent kinetic energy is analysed. Under horizontally homogeneous, quasi-steady conditions the budget of the ensemble averaged turbulent kinetic energy $\langle K \rangle$ is given by

$$\begin{aligned} \frac{\partial \langle K \rangle}{\partial t} = & \underbrace{- \langle U'_i W' \rangle \frac{\partial U_i}{\partial z}}_I + \underbrace{\lambda_3 \langle W' T' \rangle}_{II} \\ & - \underbrace{\frac{\partial}{\partial z} \langle W' K \rangle}_{III} - \underbrace{\frac{1}{\rho_0} \frac{\partial}{\partial z} \langle W' P' \rangle}_{IV} - \underbrace{\langle \varepsilon \rangle}_V \end{aligned} \quad (7.5.1)$$

where the brackets denote ensemble averaging and U'_i, W', T', P' are deviations from the ensemble-mean values $\langle U_i \rangle, \langle W \rangle, \langle T \rangle, \langle P \rangle$, respectively. The first two terms on the right-hand side represent the production terms due to shear (I) and buoyancy (II). The third and the fourth term are the turbulent transport (III) and the pressure transport (IV) term, respectively, and the last term represents the dissipation term (V). The time-rate-of-change term is close to zero

¹It must however be kept in mind that the Arakawa C grid is known to produce large errors associated with the numerical discretization of the Coriolis force.

provided the flow has reached a steady state.

With respect to the computation of the budgets, quantities like $U'_i = U_i - \langle U_i \rangle$ are required. However,

- instead of U_i , only the resolvable field $\overline{U}_i = U_i - u_i$ is available from LES,
- in the present non-stationary simulations, horizontal averaging is applied as an approximation to ensemble averaging. It approximates $\langle \overline{U}_i \rangle$, but not $\langle U_i \rangle$. The distinction shows up in terms like $\langle U'_i U'_j \rangle$ which contain both resolved and SGS contributions,

$$\langle U'_i U'_j \rangle = \langle \overline{U}_i \overline{U}_j \rangle - \langle \overline{U}_i \rangle \langle \overline{U}_j \rangle + \langle u_i u_j \rangle.$$

- From now on, the brackets will denote horizontal averaging as approximation to ensemble averaging and a double-prime the deviation thereof,

$$\overline{U}_i = \langle \overline{U}_i \rangle + \overline{U}_i''.$$

- It follows that

$$\langle U'_i U'_j \rangle = \langle \overline{U}_i'' \overline{U}_j'' \rangle + \langle u_i u_j \rangle.$$

For a comparison of LES results with ensemble-mean budgets as they are provided by field experiments, the subgrid-scale contributions have to be added. It will show up that estimations of the subgrid-scale contributions are not uniquely determined. Hence the relation between the LES results and ensemble-mean budgets is not straightforward. Presumably, the LES results approximate the ensemble-mean budgets progressively closer as the resolution is increased. The turbulent kinetic energy consists of a resolved part and the SGS turbulent kinetic energy e . The budget equation for the resolved-scale TKE is derived by subtracting from equation (3.4.1) its horizontal mean, multiplying the result by \overline{U}_i'' and averaging the resulting equation. To this equation, the horizontal averaged budget equation for the SGS TKE (for details of the averaging procedure, the reader may refer to Mironov et al. (2000)) is added. Finally, due to the periodic boundary conditions in the horizontal directions, only vertical gradients are retained. The resulting TKE budget equation reads

$$\begin{aligned} \frac{\partial}{\partial t} \left(\frac{1}{2} \langle \overline{U}_i''^2 \rangle + \langle e \rangle \right) = & \underbrace{- \left(\langle \overline{U}_i'' \overline{W}'' \rangle + \langle \overline{u}_i \overline{w} \rangle \right) \frac{\partial \langle \overline{U}_i \rangle}{\partial z}}_I + \underbrace{\lambda_3 \left(\langle \overline{W}'' \overline{T}'' \rangle + \langle \overline{w} \overline{\theta} \rangle \right)}_{II} \\ & - \underbrace{\frac{\partial}{\partial z} \left(\frac{1}{2} \langle \overline{W}'' \overline{U}_i''^2 \rangle + \langle \overline{W}'' e \rangle \right)}_{III} - \underbrace{\frac{1}{\varrho_0} \frac{\partial}{\partial z} \left(\langle \overline{W}'' \overline{P}'' \rangle \right)}_{IV} \\ & - \underbrace{\langle \varepsilon \rangle}_V - \underbrace{\frac{\partial}{\partial z} \left(\langle \overline{U}_i'' \overline{u}_i \overline{w} \rangle + \frac{2}{3} \langle \overline{W}'' e'' \rangle - \langle \nu_e \frac{\partial e}{\partial z} \rangle \right)}_{VI}. \quad (7.5.2) \end{aligned}$$

By comparison of (7.5.1) and (7.5.2), the contributions (I) - (V) of (7.5.1) can immediately be identified with their counterparts of (7.5.2). However, there is the 'remainder' (VI). Mironov et al. (2000) regard the term (VI) as 'budget imbalance'. Since in many LES the SGS turbulent kinetic energy e is not available from the data, e. g. when applying the Smagorinsky SGS formulation, the second and third part of (VI) (as well as the second part of (III)) would not be available accordingly.

Figure 7.22 displays the budget of turbulent kinetic energy (resolved plus SGS). Due to the large differences in the production mechanisms the horizontal axes show distinct ranges. All terms have been nondimensionalized by the surface buoyancy flux. It is remarkable that the runs 'weak' and 'moderate' show more similarity than the runs 'moderate' and 'strong'.

For run 'weak', the primary source over the entire mixed layer is buoyancy B while the shear contribution S rapidly decreases away from the surface. Buoyancy is a sink of turbulent kinetic energy in the entrainment region. The dissipation rate is a loss throughout. Apart from the surface region, it is nearly constant in depth. Qualitatively this finding agrees with tank experiments (Deardorff and Willis 1985), results from atmospheric measurements (Lenschow et al. 1980) and numerical studies (Schmidt and Schumann 1989). However, the amount of ε is overestimated by about a factor of three. This causes an imbalanced budget. From inertial subrange theory the relation $\varepsilon = e^{3/2}/l_\varepsilon$ can be inferred. It can be deduced that an error should be present either in the distribution of the SGS turbulent kinetic energy e or in the prescription for the dissipation length scale l_ε . No obvious error could be detected. It may only be speculated that (i) the SGS turbulent kinetic energy is erroneous due to the poorly resolved shear production term near the surface and that (ii) the effective grid size (proportional to the dissipation length scale) might be too small and contains aliasing effects. In contrast, the distributions of the two transport terms is correctly represented in Figure 7.22. It can be seen that the turbulent transport term T is responsible for the downward motion of turbulent kinetic energy from the upper half to the lower half of the mixed layer. The pressure transport term brings turbulent kinetic energy from the middle of the mixed layer to the depth and to the surface. Surprisingly, shear production grows again in the middle of the mixed layer. Figure (a) indicates that this contribution comes from the entrainment zone where one can find a sink of shear production. This process is not confirmed by the literature. At the worst, this is a footprint of internal waves reflection at the lower boundary. Hopefully, it represents non-local physical mechanisms in the entrainment zone acting back on the mixed layer (known in meteorology as 'top-down diffusion', Wyngaard and Brost 1984). Due to the relative coarse resolution, details of the entrainment process cannot be evaluated from the current simulations. The pressure transport term P shows wiggles in the middle of the mixed layer which may be another hint of spurious reflections. However, shear production at $z = D$ on the order of $0.05B_0$ is consistent with results from the literature

(Moeng and Sullivan 1994, Mironov et al. 2000). While shear production is increased for run 'moderate' in (b), the shear contribution is still limited to the near-surface region. The convective plumes induce effective mixing resulting in a rapid decrease of shear production with depth. Figure (b) does not exhibit the unexpected transport of shear production. The magnitude of the turbulent transport term T does not depend on mean shear.

For run 'weak' the transport term shows a minimum of about $0.35B_0$ at a depth of roughly $0.3D$ while the same minimum shows up at a depth of about $0.1D$ for run 'moderate'. It reverses sign in the middle of the mixed layer. The feature suggests that the transport term is mainly due to buoyant forcing. The pressure term is slightly larger than in run 'weak'. The terms in the entrainment zone are almost unchanged. The dissipation rate is now close to linear instead of being constant in the bulk of the mixed layer. Its value is still too large to obtain a balanced budget but the situation has improved compared to case 'weak'.

Run 'strong' shows the largest contribution of shear production. The shear term decreases slowly with depth and becomes zero only in the middle of the mixed layer. Accordingly, ε decreases slowly. The transport and the pressure term are not negligible compared with the buoyancy contribution but the main balance is between shear production and dissipation. This is a typical feature of shear flows but in run 'strong' the buoyancy influence is strong enough to provide effective mixing in the bulk of the layer. It is clearly visible that ε is overestimated for runs 'moderate' and 'strong' analogously to run 'weak'. This point requires further investigation.

The imbalance term (VI) from (7.5.2) is not considered here since the analysis revealed that it decreases rapidly away from the very surface.

In summary, the analysis of the budget of turbulent kinetic energy shed some light on the driving mechanisms. In free convection, all terms are of comparable size. The transport terms are by no means negligible but provide the transport of turbulent kinetic energy from its generation to its dissipation region. It is the non-local character which distinguishes convection from turbulent shear flow. With increasing shear, the dominant forcing is no longer buoyancy but shear production. The terms of turbulent and pressure transport term show unique dependence on increasing shear. The reason for the unrealistic large values of dissipation rate have to be explored in future work.

7.6 SGS contributions

7.6.1 Comparison with the original formulation

In order to evaluate the role of the SGS model, the present convection model is compared with the previous model in the original formulation by Backhaus 1995. The original model has been extended to three dimensions by Kämpf 1996 and

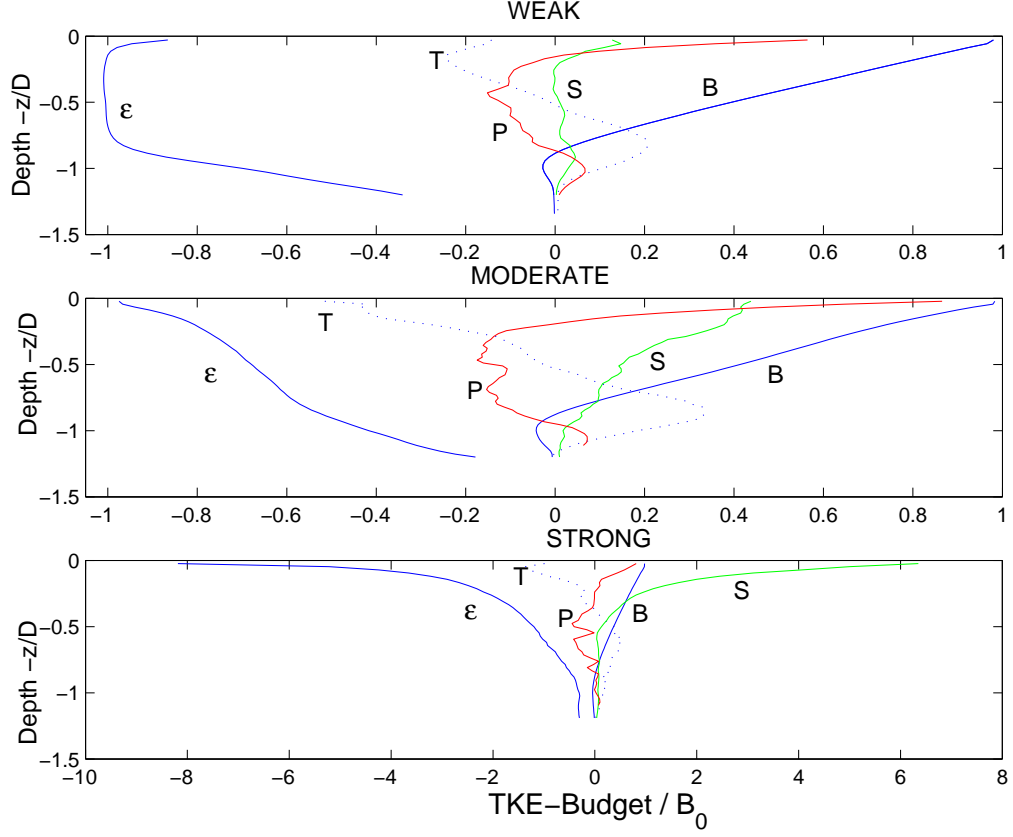


Figure 7.22: Vertical distributions of the terms in the budget equation for the total turbulent kinetic energy according to (7.5.2) for the runs 'weak', 'moderate', and 'strong', respectively. The solid blue line marked with a 'B' is the buoyancy production, the solid green line ('S') is the shear production, and the solid red line ('P') is the pressure transport term. The blue dotted line ('T') represents turbulent transport and the dissipation rate (ϵ) is denoted by a blue dashed line. Note the distinct range of the horizontal axes.

used in a number of numerical studies (Kämpf 1996, Kämpf and Backhaus 1998, Backhaus and Kämpf 1999, Kämpf and Backhaus 1999). However, it has to be stressed that in general the role of the SGS model cannot be discriminated from the role of numerical algorithms (Sagaut 2001). Additionally, boundary conditions, particularly the 'wall model', play a central role on the model performance. Therefore, a short description of the model in the formulation by Backhaus (1995) and Kämpf (1996) is given. Afterwards, some of the model predictions are compared with the present LES results. The SGS eddy viscosity is originally given by the Smagorinsky formulation with buoyancy correction (see (3.2.2)).

The implementation of the upper boundary condition of Backhaus (1995) and Kämpf (1996) for the momentum flux is very similar to the present approach. The authors also define a model layer outside the model domain (with vertical grid index $i = 0$, compare to Figure 4.4). However, there is an essential difference in the location of the eddy viscosity which Backhaus (1995) and Kämpf (1996) place in the middle of the cell on a ' P -point' (see Figure 4.3). During the computation of the vertical gradients at the upper boundary (compare 4.2.7),

$$\begin{aligned}\frac{\partial U}{\partial z} &= \frac{\tau_0^{(x)}}{\varrho_0 \nu_*} & \text{at } z = 0, \\ \frac{\partial V}{\partial z} &= \frac{\tau_0^{(y)}}{\varrho_0 \nu_*} & \text{at } z = 0,\end{aligned}$$

the authors have to make further assumptions about the actual value of ν_* . This introduces a value of large uncertainty. The Backhaus (1995) and Kämpf (1996) wall model for the temperature field reads

$$T_1^{n+1} = T_1^n - \frac{\Delta t}{\Delta z} Q_0,$$

which implies that during the integration over one time step the heat loss to the atmosphere is distributed over the first grid cell. Horizontal diffusion or any advection of temperature is ignored in this formulation. The advection of momentum, heat and salinity is originally discretized by the upstream method which is known to induce a large amount of numerical diffusion (Sagaut 2001). Additionally, there is no thermocline in the simulations of Kämpf (1996). Consequently, the mixed layer extends over the entire depth of the model domain.

Unfortunately, only resolved-scale parts of the second-order moments are available from the study by Kämpf (1996). Two runs from Kämpf (1996) will be considered for comparison. The first assumes the absence of a wind forcing and will therefore be denoted as the 'K-free' run. The second regards convection in the presence of steady wind conditions at 10 m s^{-1} and will therefore be referred to as the 'K-forced' run. Both runs are performed on a numerical grid with 200 points in the horizontal directions and 20 points in the vertical direction. The grid spacing is 10 m in each direction. The heat flux in the 'K-free' run

is 174.5 Wm^{-2} corresponding to a bouyancy flux of $-1.03 \cdot 10^{-8} \text{ m}^2 \text{ s}^{-3}$. The heat flux in the 'K-forced' run is 580 Wm^{-2} corresponding to a bouyancy flux of $-3.41 \cdot 10^{-8} \text{ m}^2 \text{ s}^{-3}$. Figure 7.23 compares predicted second-order moments from the present run 'weak' (solid lines) with the free convective flow 'K-free' in Kämpf (1996) (dotted lines). In Figure (a) the resolved part of the vertical heat flux is displayed. It is visible that in run 'free' the heat flux is overpredicted since it cannot exceed the surface value unity. Obviously, too little energy due to thermal instability has been dissipated from the resolved scales. The vertical velocity variance (Figure 7.23 (b)) is similar in shape in both simulations but the maximum value differs by almost fifty percent. The peak value of the run 'weak' is located slightly deeper than in the 'K-free' run. The horizontal velocity variance (sum of zonal and meridional contributions) in run 'K-free' is larger than in run 'weak' near the surface but becomes smaller in the bulk of the mixed layer. The large gradient at the mixed layer bottom is probably an artefact caused by the applied no-slip boundary condition.

In Figure 7.24, second-order moments from the present run 'strong' (solid lines) is compared with the sheared convective flow 'K-forced' in Kämpf (1996) (dotted lines). From Figure 7.24 (a) it can be seen that the resolved-scale part of the heat flux is overpredicted in run 'K-forced', analogously to what had shown up in 7.23 (a). The vertical velocity variance is shown in Figure 7.24 (b). Both simulations are in rough agreement. Figure 7.24 (c) shows the horizontal velocity variance. Near the surface the 'K-forced' run shows significantly higher values although the wind speed is smaller than in run 'strong'.

Exemplary one horizontal section from the 'K-forced' run of Kämpf (1996) is considered in Figure 7.25. The roll structure of the convective flow is readily visible. As the wind blows in meridional direction, the structures show a turning of about 45° to the right. The rolls are elongated and show a high degree of coherence. Comparison with the Figures 7.9 and 7.10 indicates that this high degree of coherence is probably due to the excessive damping of the Smagorinsky SGS scheme. Probably, the assumption of an isotropic SGS eddy viscosity directly induces the 45° -direction of the rolls. This means that the weakest part of the model (the SGS model) determines the major result of the simulation (the organization of the convective structures) which is clearly undesirable. The upstream advection scheme induces additional numerical diffusion. Both sources of false diffusion tend to convert the high-turbulent flow into a 'quasi-laminar' flow with overly smooth and coherent structures.

In summary, the introduction of physically more plausible upper boundary conditions and the turbulence closure at a higher level compared with the original formulation improved the results significantly and gave better agreement with available experimental and numerical data.

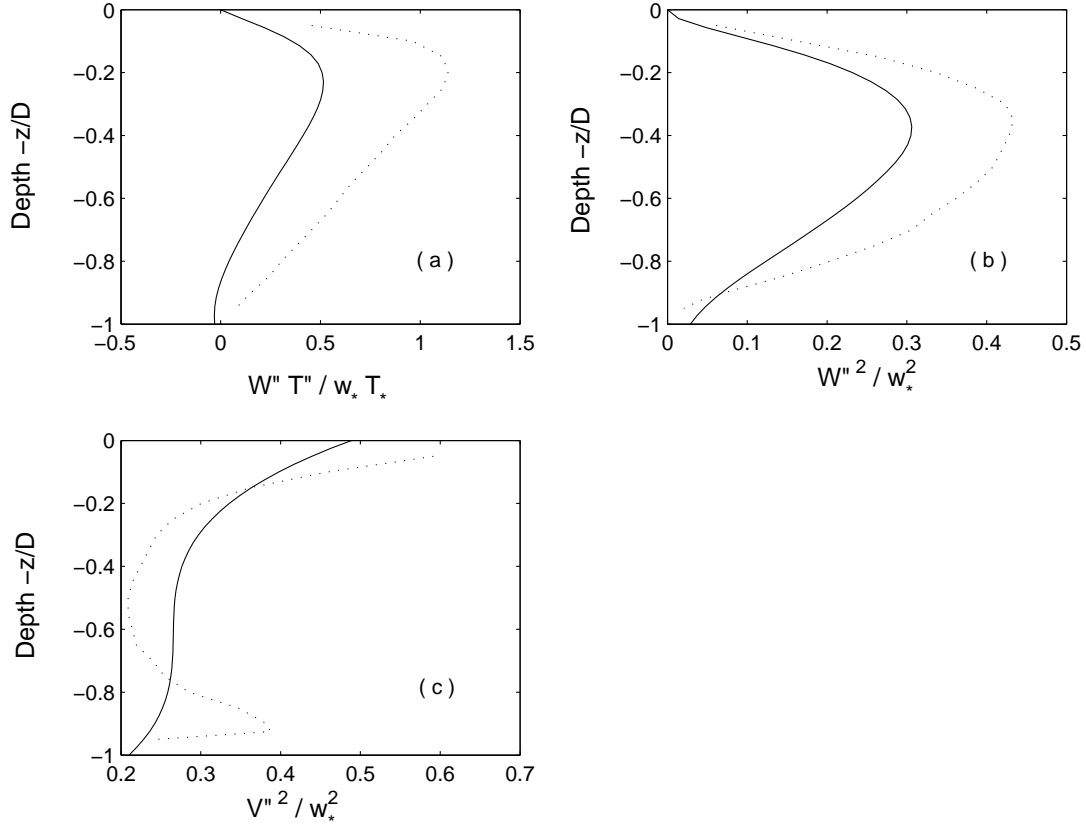


Figure 7.23: Vertical distributions of the vertical heat flux and the velocity variances. The LES results for run 'weak' are compared with results by Kämpf (1996) for free convective flow. This flow is referred to as 'K-free'. The solid lines display results from run 'weak' while the dotted line represent results taken from Kämpf (1996). Only resolved-scale parts are depicted.

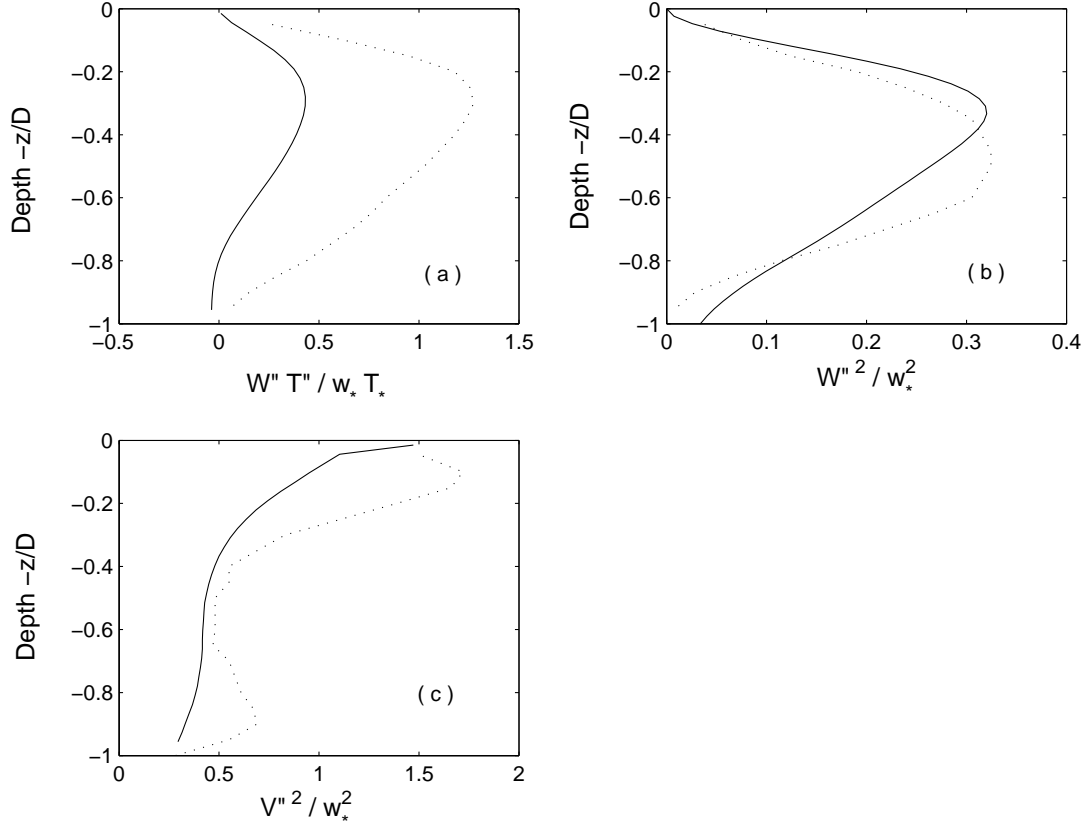


Figure 7.24: Vertical distributions of the vertical heat flux and the velocity variances. The LES results for run 'strong' are compared with results by Kämpf (1996) for sheared convective flow at a windspeed of 10 ms^{-1} . This flow is referred to as 'K-forced'. The solid lines display results from run 'strong' while the dotted line represents results taken from Kämpf (1996). Only resolved-scale parts are depicted.

7.6.2 Numerical and physical diffusion

Next the effect of numerical induced diffusion on the temperature field is illustrated exemplarily. In the appendix C it is shown that the numerical flux (equation(C.0.2)) is composed of upstream flux function and a flux correction. The flux correction is limited by the flux-limiter ϕ which can be seen from equation (C.0.10) to lie in the range between 0 and 2 depending on the ratio of consecutive gradients θ from equation (C.0.9). From LES data it is possible to infer the value of θ and thus of ϕ in each grid point where to any grid point there are three values of ϕ due to the three-dimensional flow field. For the sake of simplicity, only the *meridional* direction is considered in the following. The numerical diffusion coefficient $\nu_2^{(num)}$ can be approximated as the weighted sum of the numerical diffusion coefficient of the upstream method and the numerical diffusion coefficient of the Lax-Wendroff method. The weighting factor is the flux-limiter ϕ_j according to equation (C.0.2) where j denotes the grid index in meridional direction,

$$\nu_2^{(num)} = (1 - \phi_j) \cdot \nu_2^{(num, up)} + \phi_j \cdot \nu_2^{(num, LW)}.$$

Let the linear advection equation

$$\frac{\partial T}{\partial t} + V \frac{\partial T}{\partial y} = 0,$$

be discretized by the upstream method,

$$T^{n+1} = T^n - \frac{V \cdot \Delta t}{\Delta y} \begin{cases} T_j^n - T_{j-1}^n & \text{if } V > 0, \\ T_{j+1}^n - T_j^n & \text{if } V < 0. \end{cases}$$

It is possible to calculate the numerical diffusion coefficient of the upstream method analytically (e.g. LeVegue 1992). It is given by

$$\nu_2^{(num, up)} = \frac{V \cdot \Delta y}{2} \left(1 - \frac{|V| \cdot \Delta t}{\Delta y} \right).$$

For the LES data at $z/D = 0.1$ the horizontal mean value of the numerical diffusion coefficient is computed as $\nu_2^{(num, up)} \approx (7.26 \pm 11.41) \cdot 10^{-2} m^2 s^{-1}$. Analogously it can be calculated that the Lax-Wendroff scheme is free of numerical diffusion, hence

$$\nu_2^{(num, LW)} = 0.$$

The distribution of the flux-limiter ϕ_j is plotted in Figure 7.26 where the temperature field at $z/D = 0.1$ of the run 'moderate' is considered. There are three extreme cases visible:

- for $\phi_j = 0$ (shown in blue) the TVD scheme is reduced to the upstream scheme with high numerical diffusion,

- for $\phi_j = 1$ (shown in green) the TVD scheme is reduced to the Lax-Wendroff scheme with no numerical diffusion,
- for $\phi_j > 1$ the TVD scheme is reduced to a scheme which is composed of upstream scheme plus diffusion correction. This kind of scheme can only be applied locally since it is unstable in a global sense².

Since blue is the dominant color it is obvious that in the mean there is rather strong numerical diffusion present. The horizontal mean value of ϕ_j is 0.819 ± 0.562 which corresponds to a horizontal mean numerical diffusion coefficient in meridional direction of about $(9.6 \pm 69.6) \cdot 10^{-3} m^2 s^{-1}$ with maximum values of $0.456 m^2 s^{-1}$. Note the large variability of this quantity where the standard deviation exceeds the mean value by one order of magnitude. These values have to be compared with the eddy diffusivity from the SGS turbulence model. In Figure 7.27 there is the SGS eddy diffusivity displayed for comparison. It can be seen that the SGS eddy diffusivity is also a rapidly varying function of the flow. In general it is quite small but on the edges of intense convective motion it raises suddenly. For numerical stability reasons, the diffusivity is allowed to lie in the interval of $1 \cdot 10^{-5}$ and $2 m^2 s^{-1}$. Both values are somewhat arbitrary. Unfortunately, it can be seen from 7.27 that both the minimum and the maximum value of eddy diffusivity are often reached. This leads to the unwarranted result that the choice of these values directly affects the flow. The mean value of χ_2 from Figure 7.27 and its standard deviation is about $(0.275 \pm 0.514) m^2 s^{-1}$. Thus, the contribution of numerical diffusion can be regarded as rather small in a global sense. On average, numerical diffusion is only three percent of the actual physical diffusivity. It is however by no means negligible since in a local sense it can reach the same order of magnitude.

This is even more true with respect to the vertical diffusion. Figure 7.28 depicts a vertical section of the flux-limiter ϕ_k for vertical advection. The figure reveals that on average, $\phi_k = 0.9528 \pm 0.3587$ which is very close to the diffusion-free Lax-Wendroff algorithm for which $\phi = 1$. However, the amount of numerical diffusion (indicated by the blue regions) is large whenever there is a downward event. As the vertical numerical diffusion of the upwind scheme is on the order of $w_{max} \cdot \Delta x / 2 \approx 0.1 m^2 s^{-1}$, Figure 7.28 indicates that the entrainment process is accompanied by a large amount of numerical diffusion. Hence, numerical diffusion is of the same order of magnitude as physical SGS diffusion which is restricted to be smaller than $0.15 m^2 s^{-1}$ in the vertical direction. It is for this reason that entrainment processes at the edge of the mixed layer cannot be discriminated from pure numerical artefacts. Consequences of the unwarranted diffusion can be found in the overly smooth entrainment regions in the Figures 7.14 and 7.18, respectively.

²For $\phi_j = 2$ it can be shown to approach the downstream scheme for small velocity V .

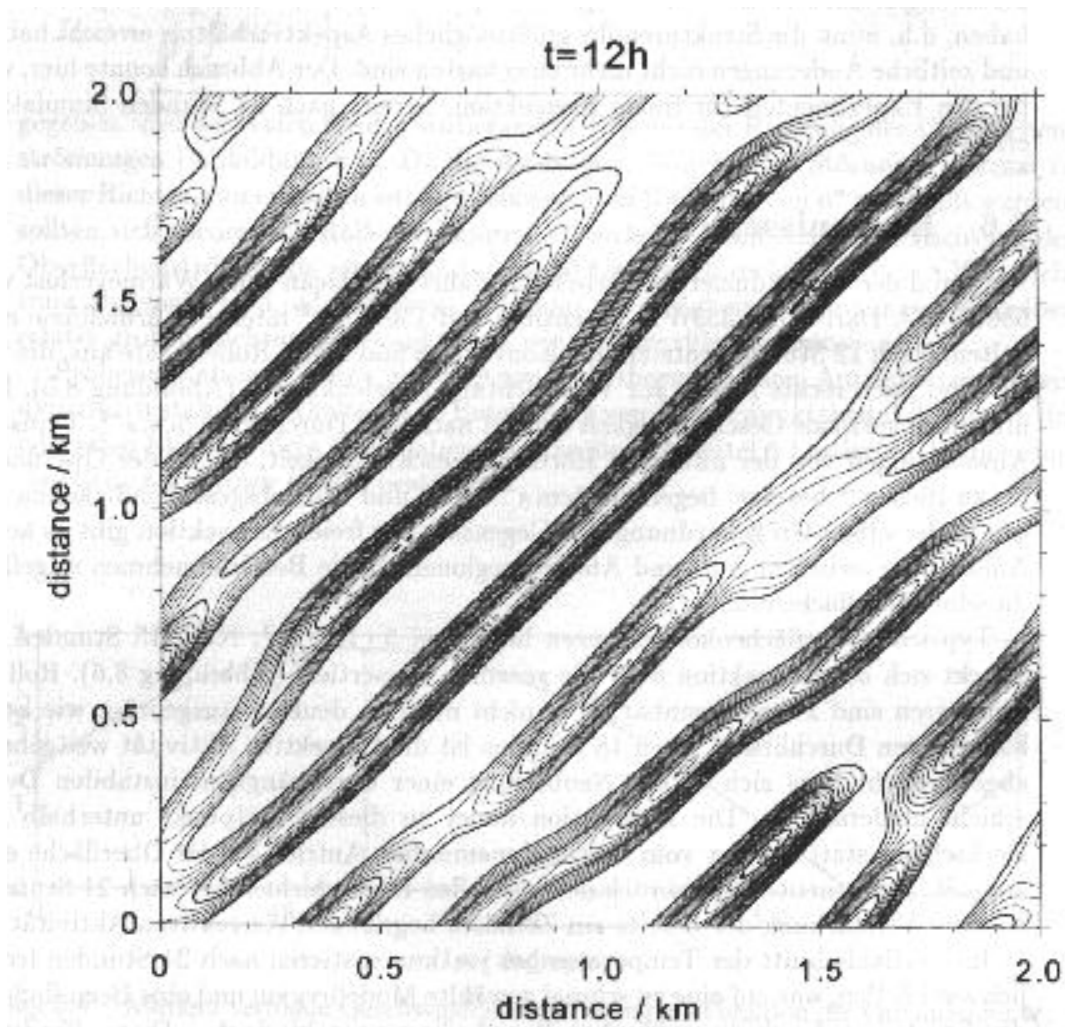


Figure 7.25: Horizontal cross-section of the near-surface temperature field. The figure is taken from Kämpf (1996). The figure displays a forced convective flow which is referred to as 'K-forced'. The black regions are convergent downward regions while the divergent upward regions are white. The winds blows in meridional direction at 10 m s^{-1} .

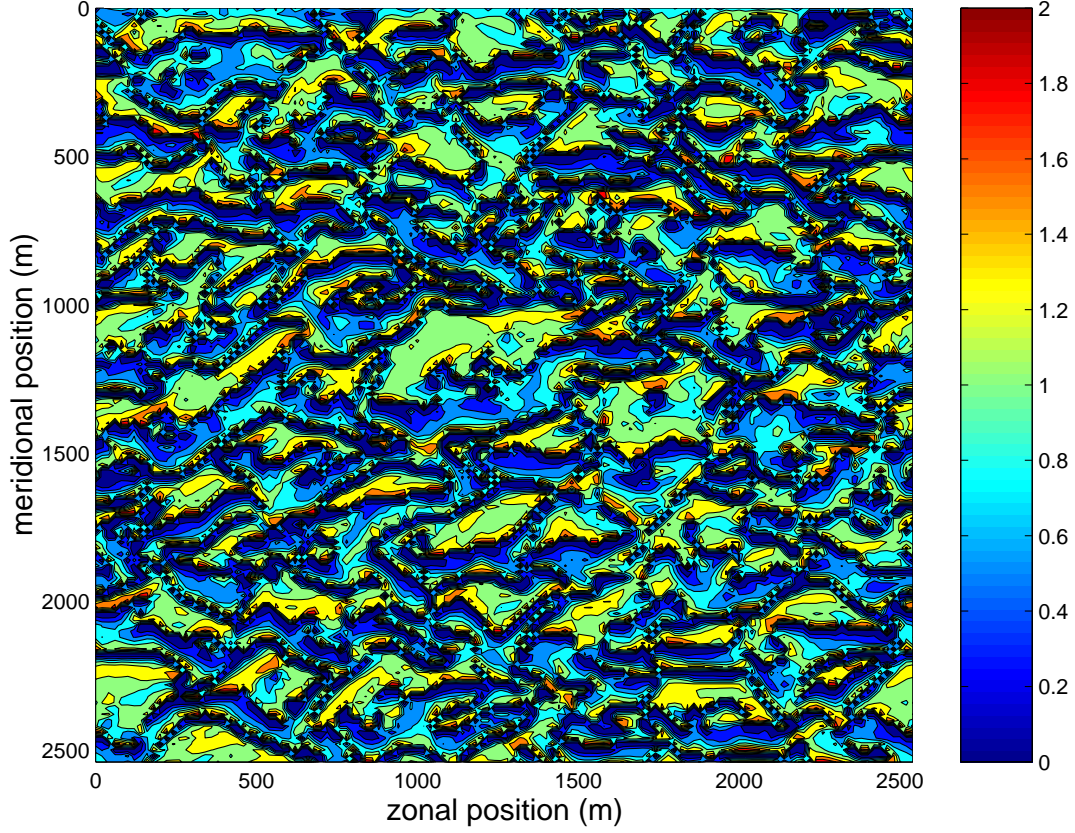


Figure 7.26: Horizontal cross-section of the near-surface field of the numerical flux-limiter function in meridional direction, ϕ_j . The figure shows results at $0.1 D$ for the run 'moderate'. The flux limiter is constructed to lie between 0 and 2. The blue regions are regions of high numerical diffusion corresponding to $\phi_j \ll 1$. The green regions are regions of low numerical diffusion corresponding to $\phi_j \approx 1$. In yellow to red regions numerical diffusion is extracted from the temperature field ('numerical antidiffusion'). This corresponds to $\phi_j > 1$.

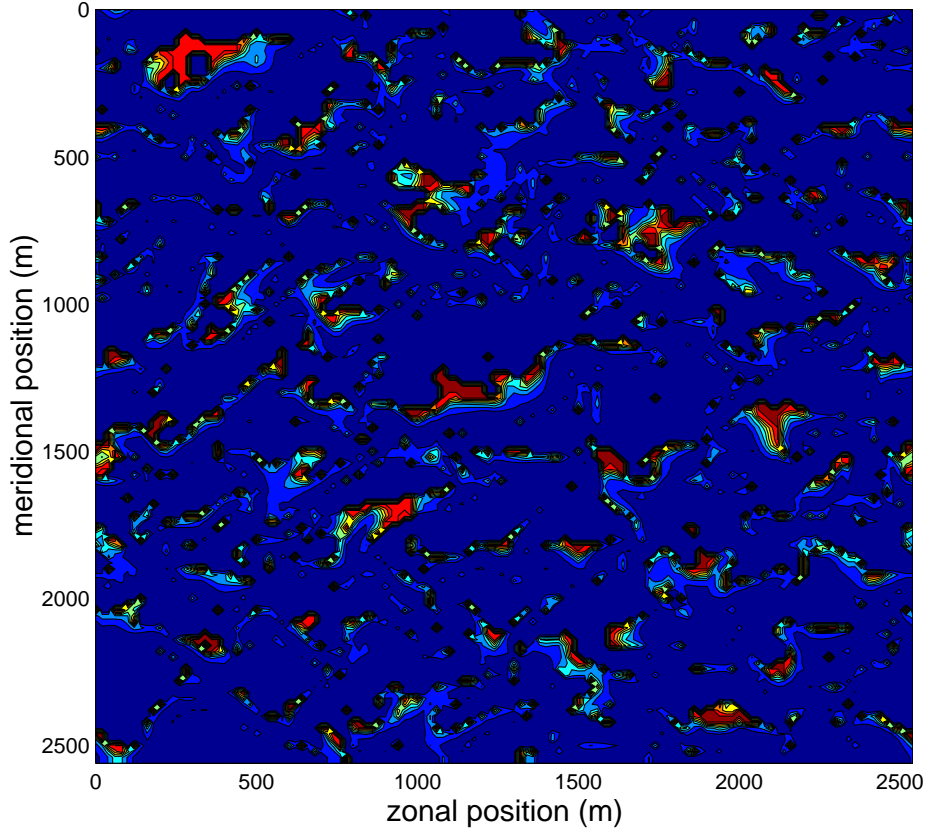


Figure 7.27: Horizontal cross-section of the near-surface field of the SGS eddy diffusivity component in meridional direction, χ_2 . The figure shows results at $0.1 D$ for the run 'moderate'. Note that the figure displays the diffusivity in units $m^2 s^{-1}$. The minimum and maximum values are $1 \cdot 10^{-5}$ and $2 m^2 s^{-1}$, respectively.

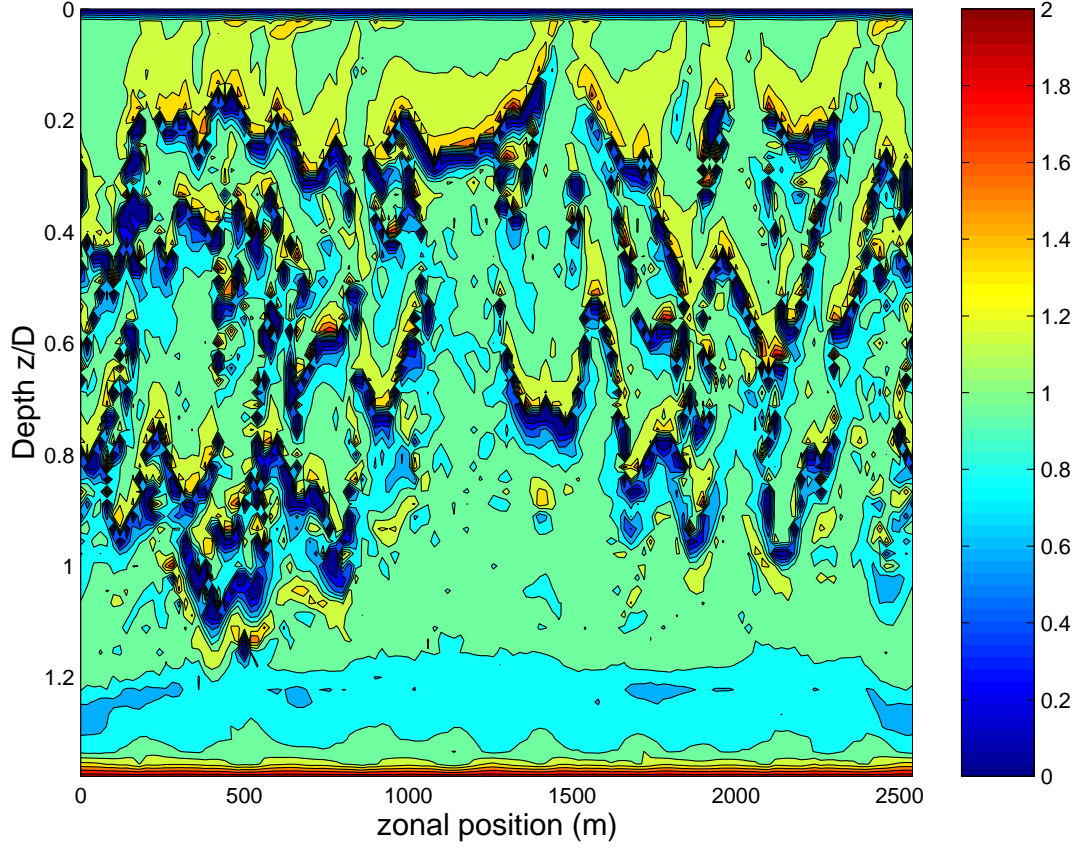


Figure 7.28: Vertical cross-section of the numerical flux-limiter function in vertical direction, ϕ_k . The figure shows results for the run 'moderate'. The flux limiter is constructed to lie between 0 and 2. The blue regions are regions of high numerical diffusion corresponding to $\phi_j \ll 1$. The green regions are regions of low numerical diffusion corresponding to $\phi_j \approx 1$. In yellow to red regions numerical diffusion is extracted from the temperature field ('numerical antidiffusion'). This corresponds to $\phi_j > 1$.

Chapter 8

Summary and Outlook

The interaction between shear and unstable stratification in the oceanographic context has been studied by performing numerical simulations.

Oceanic convection is mostly accompanied by strong winds so that it differs significantly from the classical Rayleigh-Bénard experiment. The wind-induced effect on thermal convection is stronger in the Greenland Sea than it is in the Labrador Sea. This can be dedicated to a comparatively weaker buoyancy forcing in the Greenland Sea. Hence, the effect of wind-induced shear is expected to become more pronounced in the Greenland Sea. The role of mechanically and thermally generated turbulence can be expressed in terms of velocity scales, namely the surface friction velocity u_* and the Deardorff velocity scale w_* , respectively. The ratio of both is used in boundary-layer meteorology in order to describe the regime of convective shear flows. An analogous approach has been attempted in the present work for the oceanic case.

The structure of instantaneous flow fields and turbulence statistics in shallow convection affected by wind-induced shear has been analysed using a data set derived from large-eddy simulations (LES). Three different scenarios were considered: one is the reference case of a nearly shear-free convective mixed layer penetrating into a stably stratified layer (case 'weak'). The other two are convective mixed layers affected by moderate and strong wind-induced shear, respectively (cases 'moderate' and 'strong'). The buoyant forcing was held constant in the three runs.

LES explicitly computes the large energy-containing eddies and parameterises the small eddies (subgrid-scale) which are not captured by the numerical grid. The parameterisation of the small eddies has been formulated as an iterative algebraic second-order moment approach. This approach avoids the common assumption that subgrid-scale stress tensor and strain-rate tensor are aligned. The class of recently proposed non-linear eddy viscosity models has been demonstrated to be a special case of the present second-order moment approach. A correction function for the dissipation of turbulent kinetic energy in stable stratification has been taken from literature and incorporated in the numerical model. The rigid-lid approximation was applied to filter surface gravity waves. Flux-limited

advection schemes have been implemented in the equations of momentum and heat transport. Their amount of numerical diffusion is commonly less than the amount of diffusion due to the subgrid-scale turbulence model. Time integration is performed using the second-order predictor-corrector scheme. For the construction of the numerical grid, the extension of the mixed layer has to be estimated. The mixed layer extension is the relevant integral length scale for the large-scale plumes which are the dominant feature in convective flows. The vertical and horizontal dimensions of the numerical grid have to be related to this quantity. The vertical dimension has been chosen to be sufficiently in order to reduce internal gravity wave reflection at the bottom boundary. In horizontal directions, cyclic boundary conditions are applied. Hence, horizontal dimensions have been chosen sufficiently large in order to accomodate several large-scale plumes. From bulk layer modeling an analytic approximation to the mixed layer growth is derived which is in turn applied to estimate the expected mixed layer depth at the end of the simulation. The agreement between the simple theoretical prediction and the numerical findings was rather striking. For the determination of the grid size, spectral energy arguments were applied. The grid is capable of resolving structures whose spectral energy is by a factor of fifty smaller than the spectral energy of the most energetic structures. This procedure ensures to separate the large from the small eddies in a well-defined manner.

From the simulations it is found that the heat transfer, i.e. the heat loss to the atmosphere, decreases slowly with increasing shear. This result does not confirm the atmospheric measurements presented in Monin and Yaglom (1979) who found increasing heat transfer with increasing shear. However, it agrees with the direct numerical simulations of Domaradzki and Metcalfe (1988) who found decreasing heat transfer with increasing shear.

Mean profiles of temperature and velocity show the ability of convection to homogenize the water column. Momentum transport calculations for the run 'moderate' and the run 'strong' indicate that the presence of an unstable bouyancy flux alters the Ekman dynamics considerably. Run 'moderate' revealed a damping of the magnitude of the momentum transport associated with the mean flow by more than 50 percent but the resulting transport angle was close to its neutral value of 90° . In contrast, the mean momentum transport in run 'strong' was found to be enlarged compared to the neutral case. The transport angle was found to be -58° . Apparently, the interaction of bouyancy flux and mean shear is a highly nonlinear process with a kind of 'phase transition' somewhere between the cases 'moderate' and 'strong'.

The visualisation of instantaneous flow pattern reveals that strong shear is required in order to organize the convective structures in the form of convective rolls. The lower shear runs instead resulted in convective cells which were by no means hexagonal (as in laboratory experiments) but approximately isotropic. Convective instabilities were found to grow with increasing shear. A detailed inspection of entrainment was not possible due to the relatively coarse resolution.

However, it was found that while the vertical velocity at the mixed layer base is well-mixed for the runs with larger mean shear, the opposite is true for temperature fluctuations which are the more significant the larger the mean shear. This is possibly linked to the presence of the counter-gradient flux.

Profiles of mean variances and fluxes were found to be in good agreement with existing data sets of experimental and numerical studies. They revealed the tendency of shear to slightly suppress vertical and to strongly enhance horizontal motion. The linear profiles of the vertical heat flux indicate that all runs had reached a quasi-stationary state. The entrainment coefficient was found to be largest for the run 'moderate' and to lie in a range of 0.2 to 0.3 similar to values from the literature. The profiles indicate that the grid resolution is still too coarse to capture entrainment processes.

The budget equation of the total turbulent kinetic energy was analysed and the main production and transport mechanisms were identified. With increasing shear the role of bouyant production becomes smaller and the flow approaches an approximate balance of shear production and dissipation of turbulent kinetic energy. This is a typical feature of turbulent shear flows. However, the LES data report very large values of dissipation which cause an imbalance of the budget of turbulent kinetic energy. The imbalance decreases for incereasing shear suggesting that the imbalance might at least partially be attributed to poorly resolved shear production terms.

It is difficult to evaluate the performance of the new subgrid-scale model due to the complexity of sheared convection. The surface flow exhibits less coherent structures which indicates that the excessive damping of the Smagorinsky model and the upstream advection scheme has been reduced. Any effect of the correction function for the dissipation rate could not be detected. Unfortunately, the simulations appear to be sensitive to minimum and maximum values of the turbulent diffusion coefficients for which one has no other guide than experience. Despite of the relatively expensive TVD advection scheme the model still suffers from severe numerical diffusion. The effect showed up in the profiles of vertical heat flux and temperature variance. Those profiles appear to be too smooth. For future work, it is desirable to replace the TVD Lax-Wendroff scheme with an algorithm which is, if not better, at least faster. With regard to numerical diffusion it might appear doubtful to apply sophisticated SGS turbulence models. It must be emphasized that this is not true for the near-surface flow where numerical diffusion in vertical direction is small.

It is surprising to see that in many respects the similarity between the runs 'weak' and 'moderate' were more striking than between the runs 'moderate' and 'strong'. This shows up not only in the mean temperature profile but also in instantaneous flow pattern and the budget of turbulent kinetic energy. Since in both 'weak' and 'moderate', the flow was organized in convective cells whereas it was organized in convective rolls in the run 'strong', there appears to be a fundamental difference in the properties of convective shear flow related to the dominating coherent

structures.

A composed velocity scale proposed for atmospheric sheared convection by Moeng and Sullivan (1994) was tested with the present LES data. It showed up that the scaling is inappropriate for oceanic application. It is probably the influence of Earth's rotation which inhibits to simply adopt atmospheric approaches to the ocean. This is suggested by the profiles of the vertical momentum flux and the variances of horizontal momentum. Both show distinct behaviour from atmospheric findings which suggests a more pronounced effect of the coriolis force.

It is the obvious task for future work to provide higher numerical accuracy. The present simulations demonstrate that the spatial resolution has to be increased. This is true for the near-surface region and the entrainment region. Whereas it is known that LES performs poorly in the vicinity of solid walls the shallow oceanic Ekman layer is another requirement for higher resolution. Higher resolution in turn requires more grid points and more computing time. The available computing resources did not only limit the spatial resolution but also the vertical dimension of the flow since deeper mixed layers require longer time-integration. As one is preliminary interested in the stationary state of the convective flow, it might appear tempting to use implicit time-integration schemes. However, the time step was mainly limited by fast-travelling internal waves. Hence, it might be more reasonable to improve the method which solves the poisson equation for the pressure. Some investigation has already been done in this direction.

The success of LES for oceanic applications is related to the key issue of realistic surface modeling. The applied rigid-lid approximation does not account for the range of wave-associated phenomena which are found in reality. In engineering and atmospheric turbulent research the limitations of numerical simulations are mainly due to the shallowness of viscous and molecular boundary layers. While these are 'only' technical problems in terms of computational time the issue of the oceanic surface boundary conditions is more fundamental. A lot more research will be required at this point.

Appendix A

Rotational effect on dissipation

The correction function $g(Ro)$ introduced in equation (3.3.14), accounts for the suppression of the turbulent energy cascade caused by the Earth's rotation. However, the formulation of $g(Ro)$ is simplified compared to the original derivation by Canuto and Dubovikov (1997). Their function (labelled ' cd ') reads as

$$g_{cd} = 1 + \frac{a_{cd}Ro_{cd}}{1 + b_{cd}Ro_{cd}}, \quad (\text{A.0.1})$$

where $a_{cd} = 0.25$, $b_{cd} = 0.12$ and Ro_{cd} is a Rossby number which is based on the dissipation rate itself, $Ro_{cd} = (\Omega_3 e / \varepsilon)^2$. As ε is not stored in the present model but computed diagnostically, it is not available for the Rossby number based equation (A.0.1).

Instead, ε is computed using the linearised form of (A.0.1), $g'_{cd} = 1 + a_{cd}Ro_{cd}$, via

$$\varepsilon = \frac{e^{3/2}}{l_\varepsilon g'_{cd}}, \quad (\text{A.0.2})$$

which is equivalent to equation (3.3.12) and the dissipation length scale l_ε already includes the stratification correction function $f(N, S)$ according to equation (3.3.20). The resulting second-order algebraic relation is solved by

$$\varepsilon = \frac{e^{3/2}}{2l_\varepsilon} + \frac{e^{3/2}}{2l_\varepsilon} \cdot \sqrt{1 - Ro^2}, \quad (\text{A.0.3})$$

where the Rossby number $Ro = \Omega_3 l_\varepsilon / e^{1/2}$ is now based on available quantities, in contrast to Ro_{cd} . From (A.0.3) it can be seen that $g(Ro)$ is given by

$$g(Ro) = \frac{2}{1 + \sqrt{1 - Ro^2}}. \quad (\text{A.0.4})$$

which is the same as (3.3.14).

Appendix B

Second-order moments in Cartesian form

The traceless tensors Σ_{ij} , Z_{ij} introduced in equation (3.3.6) describe anisotropic turbulence production by interaction of mean flow (represented by S_{ij} and ω_{ij}) with turbulence (represented by b_{ij}). As their computation is relatively expensive it might be reasonable to attempt an order-of-magnitude estimation of their individual components and to retain only the largest contribution. This is planned for future work.

The tensors b_{ij} and S_{ij} are symmetric, i.e. $b_{ij} = b_{ji}$ while ω_{ij} is antisymmetric and all have zero trace. Therefore only six of the tensor components have to be considered. The tensor Z_{ij} is not in its general form with arbitrary external rotation but already includes the earth's rotation rate ($\vec{\Omega} = (0, \Omega_2, \Omega_3)$). During computation, as first approximation all terms containing the zonal Coriolis component Ω_2 are neglected since Ω_3 exceeds Ω_2 by one order of magnitude in high-latitude. In cartesian form the tensor components are given by ($P_s = -b_{ij}S_{ij}$ is the shear production)

$$\begin{aligned}
\Sigma_{11} &= 2(S_{11}b_{11} + S_{12}b_{12} + S_{13}b_{13}) + \frac{2}{3}P_s, \\
\Sigma_{22} &= 2(S_{12}b_{12} + S_{22}b_{22} + S_{23}b_{23}) + \frac{2}{3}P_s, \\
\Sigma_{33} &= 2(S_{13}b_{13} + S_{23}b_{23} + S_{33}b_{33}) + \frac{2}{3}P_s, \\
\Sigma_{12} &= (S_{11} + S_{22})b_{12} + S_{12}(b_{11} + b_{22}) + S_{13}b_{23} + S_{23}b_{13}, \\
\Sigma_{13} &= (S_{11} + S_{33})b_{13} + S_{13}(b_{11} + b_{33}) + S_{12}b_{23} + S_{23}b_{12}, \\
\Sigma_{23} &= (S_{22} + S_{33})b_{23} + S_{23}(b_{22} + b_{33}) + S_{12}b_{13} + S_{13}b_{12}, \\
Z_{11} &= 2b_{12}(\omega_{12} + c_9\Omega_3) + 2b_{13}(\omega_{13} - c_9\Omega_2), \\
Z_{22} &= 2b_{23}\omega_{23} - 2b_{12}(\omega_{12} + c_9\Omega_3), \\
Z_{33} &= -2b_{13}(\omega_{13} + c_9\Omega_2) + 2b_{23}\omega_{23},
\end{aligned}$$

$$\begin{aligned}
Z_{12} &= (b_{22} - b_{11})(\omega_{12} - c_9\Omega_3) + b_{13}\omega_{23} + b_{23}(\omega_{13} - c_9\Omega_2), \\
Z_{13} &= (b_{33} - b_{11})(\omega_{13} - c_9\Omega_2) - b_{12}\omega_{23} + b_{23}(\omega_{13} + c_9\Omega_3), \\
Z_{23} &= (b_{33} - b_{22})\omega_{23} - b_{13}(\omega_{12} + c_9\Omega_3) - b_{12}(\omega_{13} - c_9\Omega_2).
\end{aligned}$$

Appendix C

TVD Advection Schemes

Monotone advection approximations (e.g. the upstream method) converge in a nonoscillatory manner to the unique entropy solution (LeVeque 1992). However, they are at most first order accurate because of the large amount of numerical diffusion. Diffusion-free approximations (e.g. the Lax-Wendroff method) are at least second order accurate on smooth solutions but tend to create local extrema. Thus, first-order schemes smear out gradients, while second-order schemes produce oscillations. The reason is the leading order truncation error: in the former schemes it contains second derivatives responsible for diffusion, in the latter it involves third-order derivatives responsible for dispersion.

In the framework of flux-corrective transport (FCT) schemes (Boris and Book 1973, Zalesak 1979), the diffusive low order and the dispersive high order schemes are combined in a nonlinear way. This can be done in different ways, one of which is the method of flux-limitation. For example, regarding the Lax-Wendroff flux F^{L-W} of the temperature T_k at a place k as consisting of the upstream flux F^{up} plus a correction gives

$$F^{L-W}(T_k) = F^{up}(T_k) + [F^{L-W}(T_k) - F^{up}(T_k)]. \quad (\text{C.0.1})$$

In a flux-limiter method the correction is limited depending on the local behaviour of the temperature field, ending up in

$$F^{L-W,TVD}(T_k) = F^{up}(T_k) + \phi(T_k)[F^{L-W}(T_k) - F^{up}(T_k)], \quad (\text{C.0.2})$$

where $\phi(T_k)$ is the limiter driving the portions of the two fluxes. One possibility of choosing the flux-limiter is ensuring the TVD (Total Variation Diminishing) property (Sweby 1984). The importance of the TVD property lies in the fact that TVD schemes are monotonicity preserving, thus creating no new under- or overshoots. Defining the total variation as

$$TV(T^n) = \sum_k |T_{k+1}^n - T_k^n| \quad (\text{C.0.3})$$

the TVD constraints are satisfied if

$$TV(T^{n+1}) \leq TV(T^n). \quad (\text{C.0.4})$$

Consider a general method of the form

$$T_k^{n+1} = T_k^n + A_{k+1/2}(T_{k+1}^n - T_k^n) - B_{k-1/2}(T_k^n - T_{k-1}^n), \quad (\text{C.0.5})$$

then the sufficient condition in order for the method to be TVD is

$$A_{k+1/2} \geq 0, \quad (\text{C.0.6})$$

$$B_{k-1/2} \geq 0, \quad (\text{C.0.7})$$

$$A_{k+1/2} + B_{k+1/2} \leq 1. \quad (\text{C.0.8})$$

The TVD constraint is achieved by making the flux-limiter ϕ a function of the ratio of consecutive gradients of the temperature field, θ^1 ,

$$\theta_{k+1/2} = \frac{T_{k'+1}^n - T_{k'}^n}{T_{k+1}^n - T_k^n}, \quad (\text{C.0.9})$$

where $k' = k - \text{sgn}(c)$ depends on the flow direction. As limiter function, a smooth function suggested by van Leer (1974) is used:

$$\phi(\theta) = \frac{|\theta| + \theta}{1 + |\theta|}. \quad (\text{C.0.10})$$

¹which is not to be confused with the temperature fluctuations θ .

Appendix D

List of symbols

Quantity	Units	
A	-	entrainment coefficient
\mathcal{A}	-	similarity function
B	$m^2 s^{-3}$	bouyancy flux
B_0	$m^2 s^{-3}$	bouyancy flux at the surface
B_h	$m^2 s^{-3}$	bouyancy flux at the mixed layer base
B_{ij}	$m^2 s^{-3}$	Tensor representing the anisotropic interaction of b_{ij} and $\overline{u_i \theta}$
\mathcal{B}	-	similarity function
Ba	-	Batchelor constant
C_D	-	drag coefficient

Quantity	Units	
C_S	-	Smagorinsky constant
D	m	mixed layer depth (in Chapter 4 dissipation rate of turbulent kinetic energy)
\mathcal{D}	m	vertically averaged dissipation rate in the mixed layer
D_{ek}	m	Ekman layer depth
D_f	(<i>distinct</i>)	(SGS) third-order transport terms due to turbulent and pressure fluctuations
E	-	entrainment rate
F	$m^3 s^{-3}$	vertical flux of turbulent kinetic energy
$F_{j,k}, G_{j,k}$	$m^2 s^{-2}$	numerical approximations to $f(u), g(u, v)$
F_{ext}	ms^{-2}	external force
Fr	-	Froude number
G	-	ratio of production and dissipation of SGS turbulent kinetic energy
H_{sens}	Wm^{-2}	Sensible heat flux
H_{lat}	Wm^{-2}	Latent heat flux
\mathcal{H}_0	Wm^{-2}	dynamic heat flux at the surface
K	$m^2 s^{-2}$	horizontally averaged turbulent kinetic energy
\mathcal{K}	m	vertically averaged turbulent kinetic energy in the mixed layer
Ko	-	Kolmogorov constant
L	m	Monin-Obukhov length
L_{vap}	Jkg^{-1}	latent heat of vaporisation
\mathcal{L}	m	characteristic size of the biggest eddies in a turbulent flow
M, M_*	-	number of degrees of freedom
N	s^{-1}	Brunt-Väisällä frequency
P	$kgm^{-1}s^{-2}$	dynamic pressure
P_*	$kgm^{-1}s^{-2}$	dyn. pressure including diagonal elements of the SGS stress tensor
P_S	$m^2 s^{-3}$	production rate of (SGS) turbulent kinetic energy due to mean shear
$Q_{j,k}$	$m^2 s^{-2}$	numerical approximation to source term $q(u)$
Re, Re_*	-	Reynolds numbers
R_f	-	flux Richardson number
R_f^{cr}	-	critical flux Richardson number
Ri, Ri_1, Ri_2	-	Richardson numbers
Ro	-	Rossby number
S	s^{-1}	mean shear
S_{ij}	s^{-1}	rate-of-strain tensor
T	K	ocean Temperature
T_{air}	K	air Temperature
T_{sea}	K	sea surface Temperature
U_i	ms^{-1}	velocity components
\mathcal{U}, \mathcal{V}	ms^{-1}	vertically averaged velocities in the mixed layer
W_{10}	ms^{-1}	wind vector at $10 ms^{-1}$ height
Z_{ij}	$m^2 s^{-3}$	Tensor representing the anisotropic interaction of b_{ij} and ω_{ij}

Quantity	Units	
a_{ij}	$m^2 s^{-2}$	dimensionless anisotropic part of the SGS stress tensor
b	ms^{-2}	bouyancy
\bar{b}	ms^{-2}	vertically averaged bouyancy
b_{ij}	$m^2 s^{-2}$	anisotropic part of the SGS stress tensor
c_P, c_P^{air}	$Jkg^{-1}K^{-1}$	specific heat of water and air at constant pressure
e	$m^2 s^{-2}$	SGS turbulent kinetic energy
f_h, f_z	s^{-1}	horizontal and vertical Coriolis parameter
$f(N, S)$	-	correction function for l_ϵ due to bouyancy and shear
$f(u), g(u, v)$	$m^2 s^{-2}$	flux functions
g	ms^{-2}	Earth's gravity
$g(Ro)$	-	correction function for l_ϵ due to rotation
h	m	mixed layer depth (in Chapter 4)
i, j, k	-	grid indices
k	m^{-1}	wave number
l_c	m	filter scale
l_ϵ	m	dissipation length scale
l_ϵ^{wall}	m	dissipation length scale near the surface
l_ϵ^{rot}	m	dissipation length scale in the presence of rotation
$q(u)$	$m^2 s^{-2}$	source term
q_0	-	specific background constant humidity
q_{air}	-	specific humidity close to the sea surface
r_f	-	Ratio of critical and actual Richardson number
u_i	ms^{-1}	SGS turbulent velocity fluctuations
u_*	ms^{-1}	oceanic friction velocity
$u_*^{(h)}$	ms^{-1}	oc. friction velocity based on velocity jump at the mixed layer base
$u_i \theta$	Kms^{-1}	components of the SGS heat flux tensor
$\overline{uw}, \overline{vw}$	$m^2 s^{-2}$	components of (SGS) Reynold stress tensor
w_*	ms^{-1}	Deardorff velocity
w_e	ms^{-1}	entrainment velocity
z'	m	distance from the surface
z^+	-	non-dimensional distance from the surface
z_0	m	roughness length
α	K^{-1}	thermal expansion coefficient
$\beta_{lat}, \beta_{sens}$	-	turbulent exchange coefficients for latent and sensible heat
γ	-	isotropy factor in the Sullivan et al. (1994) model
δ	m	length scale in Ekman theory=Ekman depth $\cdot \pi^{-1}$
Δ	m	mean grid size
Δb	ms^{-2}	bouyancy jump at the mixed layer base
ΔH_{LW}	Wm^{-2}	difference of in- and outgoing long-wave radiation
Δh	m	extent of entrainment region
$\Delta x, \Delta y, \Delta z$	m	grid size in x -, y -, z -direction

Quantity	Units	
δ_h	m	molecular heat conduction layer
δ_{ij}	-	Kronecker symbol
ε	$m^2 s^{-3}$	dissipation rate of (SGS) turbulent kinetic energy
ε_{air}	-	transmission coefficient of long-wave radiation
ε_{ij}	$m^2 s^{-3}$	dissipation rate tensor of (SGS) turbulent kinetic energy
ε_θ	$K^2 s^{-1}$	half the dissipation rate of SGS temperature variance
ϵ_{ijk}	-	antisymmetric tensor
η	m	Kolmogorov scale
θ	K	SGS turbulent temperature fluctuations
$\overline{\theta^2}$	K^2	SGS temperature variance
κ	-	von Karman's constant
λ	m	SGS mixing length scale
λ_k	$ms^{-2}K^{-1}$	bouyancy parameter
μ	-	Monin-Kazanski parameter (based on mixed layer depth)
ν	$m^2 s^{-1}$	(SGS) eddy viscosity
ν_{damp}	$m^2 s^{-1}$	SGS eddy viscosity in damping layer
ν_e	$m^2 s^{-1}$	vertical eddy viscosity of SGS turbulent kinetic energy
ν_{mol}	$m^2 s^{-1}$	molecular viscosity of water
ν_{Sm}	$m^2 s^{-1}$	Smagorinsky SGS eddy viscosity
ν_T	$m^2 s^{-1}$	horizontal mean SGS eddy viscosity in the Sullivan et al. (1994) model
ν_t	$m^2 s^{-1}$	local SGS eddy viscosity
ν_*	$m^2 s^{-1}$	SGS surface eddy viscosity
Π_{ij}	$m^2 s^{-3}$	pressure-strain correlation tensor
Π_i^θ	Kms^{-2}	pressure-temperature gradient correlation tensor
ϱ_0	kgm^{-3}	reference density
ϱ_{air}	kgm^{-3}	mean density of air
Σ_{ij}	$m^2 s^{-3}$	Tensor representing the anisotropic interaction of b_{ij} and S_{ij}
σ	-	turbulent SGS Prandtl number
σ_0	-	turbulent SGS Prandtl number at neutral conditions
σ_{SB}	-	Stefan-Boltzmann constant
τ	s	SGS turbulent time scale
τ_θ	s	time scale of SGS temperature fluctuations
τ_*	s	large eddy-turnover time
τ_{ij}	$m^2 s^{-2}$	SGS stress tensor
χ	$m^2 s^{-1}$	(SGS) eddy diffusivity
χ_{mol}	$m^2 s^{-1}$	molecular diffusivity of water
χ_{Sm}	$m^2 s^{-1}$	Smagorinsky SGS eddy diffusivity
χ_*	$m^2 s^{-1}$	SGS surface eddy diffusivity
Ω_j	s^{-1}	Earth's rotation vector
ω_{ij}	s^{-1}	vorticity tensor

Appendix E

Bibliography

- Aagaard, K., and E. C. Carmack, *The role of sea ice and other fresh water in the Arctic circulation*, J. Geophys. Res., 94, 14,485-14,498, 1989.
- Anis, A., and J. N. Moum, *Prescriptions for Heat Flux and Entrainment Rates in the Upper Ocean during Convection*, J. Phys. Ocean., 25, 2142-2155, 1994.
- Asai, T., *Three-dimensional features of thermal convection in a plane Couette flow*, J. Meteor. Soc. Japan, 48, 18-29, 1970.
- Backhaus, J. O., *Prozeßstudien zur Ozeanischen Konvektion*, Habilitation thesis, Institute for Oceanography, University of Hamburg, 1995.
- Backhaus, J. O., and J. Kämpf, *Simulations of sub-mesoscale Oceanic Convection and Ice-Ocean Interactions in the Greenland Sea*, Deep-Sea Research II, 46, 1427 - 1455, 1999.
- Backhaus, J. O., H. Wehde, E. Nost Hegseth, and J. Kämpf, *'Phyto-Convection' - On the Role of Oceanic Convection in Primary Production -*, Marine Ecology Progress Series, 189, 77-92, 1999.
- Baggett, J. S., J. Jiminez, and A. G. Kravchenko, *Resolution requirements in large-eddy simulations of shear flows*, Annual Research Briefs 1997, Center for Turbulence Research, Stanford, 267-277, 1997.
- Barcilon, V. K., J. Atmos. Sci., 24, 3-5, 1967.
- Betchov, R., and A. M. Yaglom, *Comments on the theory of similarity as applied to turbulence in an unstable stratified fluid*, Izv. Akad. Nauk SSR, Ser. Fiz. Atmosf. i. Okeana, 7, 829-832 (in English transl.), 1971.
- Betts, A. K., *Non-precipitating cumulus convection and its parametrization*, Quart. J. Roy. Meteorol. Soc., 99, 178-196, 1973.

- Boris, J. P., and D. L. Book, *Flux Corrected Transport I, SHASTA, a fluid transport algorithm that works*, J. Comput. Phys., 11, 38-69, 1973.
- Bradshaw, P., *Turbulent Flow Near a solid Surface*. In: P. Bradshaw (ed.), *Turbulence*, Vol. 12 of *Topics in Applied Physics*, Springer, Berlin, Heidelberg, New York, 1976.
- Broeckner, W. S., *The great ocean conveyor*, Oceanography, 4, 79-89, 1991.
- Brown, R. A., *On the inflection point instability of a stratified Ekman boundary layer*, J. Atmos. Sci., 29, 850-859, 1972.
- Brümmer, B., *Structure, Dynamics and Energetics of Boundary Layer Rolls from KonTur Aircraft Observations*, Beitr. Phys. Atmosph., 58, 237-254, 1985.
- Burchard, H., *Applied Turbulence Modelling in Marine Waters*, Vol. 100 of *Lecture Notes in Earth Sciences*, Springer, Berlin, Heidelberg, New York, 2002.
- Burchard, H., and H. Baumert, *On the performance of a mixed-layer model based on the $k - \varepsilon$ -turbulence closure*, J. Geophys. Res., 100, 8523-8540, 1995.
- Burchard, H., and K. Bolding, *Comparative Analysis of four second-order turbulence closure models for the oceanic mixed layer*, J. Phys. Ocean., 31, 1943-1968, 2001.
- Canuto, V. M., *Large eddy simulation of turbulence: a subgrid model including shear, vorticity, rotation and buoyancy*, Journal of Astrophysics, 428, 729-752, 1994.
- Canuto, V. M., F. Minotti, C. Ronchi, M. Ypma, and O. Zeman, *Second-order closure PBL model with new third-order moments: comparison with LES Data*, J. Atmos. Sci., 51, 1605-1618, 1994.
- Canuto, V. M., and Y. Cheng, *Determination of the Smagorinsky-Lilly constant C_S* , Phys. Fluids, 9(5), 1368-1378, 1997.
- Canuto, V. M., and M. S. Dubovikov, *A dynamical model for turbulence: V The effect of rotation*, Phys. Fluids, 9, 2132-2140, 1997.
- Canuto, V. M., A. Howard, Y. Cheng, and M. S. Dubovikov, *Ocean turbulence I: one-point closure model. Momentum and heat vertical diffusivities*, J. Phys. Ocean., 31, 1413-1426, 2001.

- Carmack, E. C., *Large-Scale Oceanography of Polar Oceans*. In: W. O. Smith jr. (ed.), *Polar Oceanography, Part A.*, Academic Press, San Diego, 1990.
- Champagne, F. H., V. E. Harris, and S. Corrsin, *Experiments on nearly homogeneous shear flow*, J. Fluid Mech., 41, 81-139, 1970.
- Cheng, Y., and V. M. Canuto, *Stable stratified turbulence: a new model for the energy dissipation length scale*, J. Atmos. Sci., 51, 2384-2396, 1994.
- Chlond, A., *Grobstruktursimulation - Eine Methode zur Berechnung turbulenter atmosphärischer Strömungen*, Habilitation thesis, Department of Geophysics, University of Hamburg, 1998.
- Clark, R. A., J. H. Ferziger, and W. C. Reynolds, *Evaluation of subgrid scale turbulence models using a fully simulated turbulent flow*, J. Fluid Mech., 91, 92-106, 1979.
- Clarke, R. A., *Water mass transformation in the Nordic seas: The ICES Deep-Water Project*, Deep Sea Res., 37, 1990.
- Clever, R. M., and F. H. Busse, *Three-dimensional convection in a horizontal fluid layer subjected to a constant shear*, J. Fluid Mech., 234, 511-527, 1992.
- Craig, P. D., *Velocity profiles and surface roughness under breaking waves*, J. Geophys. Res., 101, 1265-1277, 1996.
- Craig, P. D., and M. L. Banner, *Modelling wave-enhanced turbulence in the ocean surface layer*, J. Phys. Ocean., 24, 2546-2559, 1994.
- Craik, A. D. D., and S. Leibovich, *A rational model for Langmuir circulation*, J. Fluid Mech., 73, 401-426, 1976.
- Crow, S. C., *Viscoelastic properties of fine-grained incompressible turbulence*, J. Fluid Mech., 33, 1-20, 1968.
- Deardorff, J. W., *A numerical study of three-dimensional channel flow at high Reynolds numbers*, J. Fluid Mech., 41, 453-480, 1970.
- Deardorff, J. W., *Numerical Investigation of Neutral and Unstable Planetary Boundary Layers*, J. Atmos. Sci., 29, 91-115, 1972.
- Deardorff, J. W., *Stratocumulus-capped mixed layers derived from a three-dimensional model*, Bound. Lay. Meteor., 18, 495-527, 1980.
- Deardorff, J. W., *Three-dimensional numerical study of turbulence in an entraining mixed layer*, Bound. Lay. Meteor., 7, 199-226, 1974.

- Deardorff, J. W., G. E. Willis, and B. H. Stockton, *Laboratory studies of the entrainment zone of a convectively mixed layer*, J. Fluid Mech., 100, 41-64, 1980.
- Domaradzki, J. A., and R. W. Metcalfe, *Direct numerical simulations of the effects of shear on turbulent Rayleigh-Benard convection*, J. Fluid Mech., 193, 499-531, 1988.
- Durbin, P. A., and C. G. Speziale, *Local anisotropy in strained turbulence at high Reynolds numbers*, ASME J. Fluids. Eng., 113, 707-531, 1991.
- Ekman, V. W., *On the influence of the earth's rotation on ocean currents*, Ark. Mat. Astron. Syst., 2, 1-52, 1905.
- Etling, D., and R. A. Brown, *Roll Vortices in the Planetary Boundary Layer: A Review*, Bound. Lay. Meteor., 65, 215-248, 1993.
- Fedorovich, E. E., and D. V. Mironov, *A Model for a Shear-Free Convective Boundary Layer with Parameterized Capping Inversion Structure*, J. Atmos. Sci., 52, 1995.
- Ferziger, J. H., *Large eddy simulation*. In: M. Y. Hussaini, T. B. Gatski, and J. L. Lumley (eds.), *Simulation and Modelling of Turbulent Flows*, Cambridge Univ. Press, New York, 1996.
- Gaspar, P., *Modeling the Seasonal Cycle of the Upper Ocean*, J. Phys. Ocean., 18, 1988.
- Gatski, T. B., and C. G. Speziale, *On explicit algebraic stress models for complex turbulent flows*, J. Fluid Mech., 254, 59-78, 1993.
- Germano, M., U. Piomelli, P. Moin, and W. H. Cabot, *A dynamic subgrid-scale eddy viscosity model*, Phys. Fluids A3, 1760-1765, 1991.
- Gibson, M. M., and B. E. Launder, *Ground effect on pressure fluctuations in the atmospheric boundary layer*, J. Fluid Mech., 86, 491-511, 1978.
- Gill, A. E., *Atmosphere Ocean Dynamics*, Vol. 30 of *International Geophysics Series*, Academic Press, San Diego, 1982.
- Greenspan, H. P., *The Theory of Rotating Fluids*, Cambridge University Press, New York, 1968.
- Grossman, R. L., *An Analysis of Vertical Velocity Spectra Obtained in the BOMEX Fair-Weather, Trade-Wind Boundary Layer*, Bound. Lay. Meteor., 23, 323-357, 1982.

- Harms, I. H., *Numerische Modellstudie zur winterlichen Wassermassentransformation in der Barentssee*, Ph. D. thesis, University of Hamburg, 1994.
- Hathaway, D. A., and R. C. J. Sommerville, *Nonlinear interactions between convection, rotation and flows with vertical shear*, J. Fluid. Mech., 164, 91-105, 1986.
- Hossain, M. S., *Mathematische Modellierung von turbulenten Auftriebsströmungen*, Ph. D. thesis, University of Karlsruhe, 1980.
- Huang, N. E., *On surface drift currents in the ocean*, J. Fluid. Mech., 91, 191-208, 1979.
- Ingersoll, A. P., *Thermal convection with shear at high Rayleigh number*, J. Fluid Mech., 25, 209-228, 1966.
- Jansen, E., and V. Opheim, *Overview and summary of scientific achievements*. In: E. Jansen, and V. Opheim (eds.), *ESOP-2 European Subpolar Ocean Programme - Scientific Report*, Bergen, 1999.
- Kader, B. A., A. M. Yaglom, and S. L. Zubkovskii, *Spatial correlation functions of surface layer atmospheric turbulence at neutral stratification*, Bound. Lay. Meteor., 47, 233-249, 1989.
- Kader, B. A., and A. M. Yaglom, *Mean fields and fluctuation moments in unstable stratified turbulent boundary layers*, J. Fluid. Mech., 212, 637-662, 1990.
- Kämpf, J., *Thermohaline Konvektion in Polynien arktischer Schelfmeere - numerische Prozeßstudien -*, Ph. D. thesis, University of Hamburg, 1996.
- Kämpf, J., and J. O. Backhaus, *Shallow, brine-driven free convection in polar oceans: Nonhydrostatic numerical process studies*, J. Geophys. Res., 103 (C3), 5577-5593, 1998.
- Kämpf, J., and J. O. Backhaus, *Ice-ocean interactions during shallow convection under conditions of steady winds: three-dimensional numerical studies*, Deep-Sea Research II, 46, 1335-1355, 1999.
- Kaimal, J. C., J. C. Wyngaard, D. A. Hansen, O. R. Coté, Y. Izumi, S. J. Caughey, and C. J. Readings, *Turbulence Structure in the Convective Boundary Layer*, J. Atmos. Sci., 33, 2151-2169, 1976.
- Kantha, L. H., and C. A. Clayson, *An improved mixed layer model for geophysical applications*, J. Geophys. Res., 99, 25235-25266, 1994.

- Kantha, L. H., and C. A. Clayson, *Small-scale processes in geophysical fluid flows*, Vol. 67 of *International Geophysics Series*, Academic Press, San Diego, 2000.
- Khanna, S., and J. G. Brasseur, *Three-dimensional buoyancy- and shear-induced local structure of the atmospheric boundary layer*, J. Atmos. Sci., 55, 710-743, 1998.
- Killworth, P. D., *The mixing and spreading phases of MEDOC*, J. Phys. Ocean., 7, 59-90, 1976.
- Kolmogorov, A. N., *Local structure of turbulence in an incompressible fluid at very high Reynolds number*, Doklady AN SSR, 30, 299-303, 1941.
- Kosovic, B., *Subgrid-scale modelling for the large-eddy simulation of high-Reynolds-number boundary layers*, J. Fluid Mech., 237, 261-299, 1997.
- Kraus, E. D., and J. A. Businger, *Atmosphere-ocean interaction*, Oxford Press, New York, 1994.
- Kraus, E. B., and J. S. Turner, *A one-dimensional model of the seasonal thermocline: The general theory and its consequences*, Tellus, 19, 98-106, 1967.
- Kuettner, J. P., *Cloud bands in the earth's atmosphere: Observations and theory*, Tellus, 23, 404-425, 1973.
- Launder, B. E., *Heat and Mass Transport*. In: P. Bradshaw (ed.), *Turbulence*, Vol. 12 of *Topics in Applied Physics*, Springer, Berlin, Heidelberg, New York, 1976.
- Launder, B. E., G. J. Reece, and W. Rodi, *Progress in the development of a Reynolds-stress turbulence closure*, J. Fluid Mech., 68, 537-566, 1975.
- Lenschow, D. H., J. C. Wyngaard, and W. T. Pennell, *Mean-field and second-moment budgets in a baroclinic, convective boundary layer*, J. Atmos. Sci., 37, 1313-1326, 1980.
- Lenschow, D. H., and P. J. Stephens, *The role of thermals in the convective boundary layer*, Bound. Lay. Meteor., 19, 509-532, 1986.
- Leonard, A., *Energy cascade in large-eddy simulations of turbulent fluid flows*, Adv. Geophys., 18 A, 237-248, 1974.
- LeVegue, R. J., *Numerical methods for conservation laws*, Birkhäuser, Basel, Boston, Berlin, 1992.
- Lewellen, W. S., *Use of invariant modeling*, In: W. Frost and T. H. Moulden (eds.), *Handbook of Turbulence*, Plenum Publ. Corp., New York, 1977.

- Lilly, D. K., *The representation of small-scale turbulence in numerical simulation experiments*, In: *Proceedings of the tenth IBM scientific computing symposium on environmental sciences*, Thomas J. Watson Research Center, Yorktown Heights, 1967.
- Lilly, D. K., *Models of cloud-topped mixed layers under a strong inversion*, Quart. J. Roy. Meteorol. Soc., 94, 292-309, 1968.
- Lund, T. S., and E. A. Novikov, *Parameterization of subgrid-scale stresses by the velocity gradient tensor*, Annual Research Briefs 1992, Center for Turbulence Research, Stanford, 1992.
- Lumley, J. L., O. Zeman, and J. Siess, *The influence of buoyancy on turbulent transport*, J. Fluid Mech., 84, 581-597, 1978.
- MacCormack, R. W., *The effects of viscosity in hypervelocity impact cratering*, AIAA Paper, 69-354, 1969.
- Marshall, J., and F. Schott, *Open ocean convection: Observations, theory and models*, Rev. Geophys., 37, 1999.
- Martin, S., and P. Kaufmann, *A field and laboratory study of wave damping by grease ice*, J. Glaciol., 27, 283-313, 1981.
- Maykut, G. A., *The Surface Heat and Mass Balance*, In: N. Understeiner (ed.), *Geophysics of Sea Ice*, Plenum Press, New-York, 1986.
- Mason, P. J., *Large-eddy simulation: A critical review of the technique*, Quart. J. Roy. Meteorolog. Society, 120, 1-26, 1994.
- Mason, P. J., and D. J. Thomson, *Stochastic backscatter in large-eddy simulations of boundary layers*, J. Fluid Mech., 239, 51-78, 1992.
- Maxworthy, T., and S. Narimousa, *Unsteady, turbulent convection into a homogeneous, rotating fluid, with oceanographic application*, J. Phys. Ocean., 24, 865-887, 1992.
- McWilliams, J. C., P. P. Sullivan, and C.-H. Moeng, *Langmuir turbulence in the ocean*, J. Fluid Mech., 334, 1-30, 1997.
- McWilliams, J. C., C.-H. Moeng, and P. P. Sullivan, *Turbulent Fluxes and Coherent Structures in Marine Boundary Layers: Investigations by Large-Eddy Simulation*. In: G. L. Geernaert (ed.), *Air-Sea Exchange: Physics, Chemistry and Dynamics*, Kluwer, Amsterdam, 1999.
- Meneveau, C., C. Higgins, and M. B. Parlange, *Geometric Alignments of Vorticity, Strain-Rate, Subgrid-Scale Stresses and SGS Heat Flux in the ABL*, Conference of the EGS, Nice, 2001.

- Meister, A., *Numerik linearer Gleichungssysteme*, Vieweg, Braunschweig, Wiesbaden, 1999.
- Mellor, G. L., and T. Yamada, *Development of a turbulence closure model for geophysical fluid dynamics*, Rev. Geophys., 20, 851-875, 1982.
- Melville, W. K., *Energy dissipation of breaking waves*, J. Phys. Ocean., 24, 2041-2049, 1994.
- Mertens, C., *Open-ocean convection in the Labrador and Greenland Seas: Plume scales and interannual variability*, Ph. D. thesis, Institut für Meereskunde, Kiel, 2000.
- Mesinger, F., and A. Arakawa (1976) *Numerical methods used in atmospheric models*, GARP Publ. Series, 17, Vol. I.
- Mironov, D. V., V. M. Gryanik, C.-H. Moeng, D. J. Olbers, and T. H. Warnke, *Vertical turbulence structure and second-moment budgets in convection with rotation: A Large-Eddy Simulation study*, Quarter. J. Roy. Meteorol. Soc., 126, 477-515, 2000.
- Moeng, C.-H., and P. P. Sullivan, *A comparison of shear- and buoyancy-driven planetary boundary layer flows*, J. Atmos. Sci., 51, 999-1022, 1994.
- Monin, A. S., and A. M. Obukhov, *Basic laws of turbulent mixing in atmospheric surface layer*, Trudy Geofiz. Inst. Akad. Nauk SSR, 24, 163-187, 1954.
- Monin, A. S., and A. M. Yaglom, *Statistical Fluid Mechanics*, Vol. 1, MIT Press, Cambridge, 1979.
- Oberhuber, J. M., *Simulation of the Atlantic Circulation with a Coupled Sea-Ice-Mixed Layer-Isopycnal General Circulation Model. Part I: Model Description*, J. Phys. Ocean., 23, 808-823, 1993.
- Overland, J. E., and H. Pease, *Modeling ice dynamics of coastal seas*, J. Geophys. Res., 93, 15619-15637, 1988.
- Patankar, S. V., *Numerical Heat Transfer and Fluid Flow*, Mc-Graw-Hill, New-York, 1980.
- Pope, S. B., *A more general effective-viscosity hypothesis*, J. Fluid Mech., 72, 331-340, 1975.
- Rivlin, R. S., and J. L. Ericksen, *Stress-deformation relationships for isotropic materials*, Rat. Mech. Anal., 4, 323-425, 1955.
- Rodi, W., *A new algebraic relation for calculating the Reynolds stresses*, Z. Angew. Math. Mech., 56, T219-T221, 1976.

- Rodi, W., *Turbulence models and their application in hydraulics*, Tech. Rep. Int. Assoc. for Hydraul. Res., Delft, 1980.
- Rudels, B., *Haline Convection in the Greenland Sea*, Deep Sea Res., 37, 1990, 435-450.
- Rudels, B., and D. R. Quadfasel, *Convection and deep water formation in the Artic Ocean - Greenland Sea System*, J. Mar. Syst., 2, 1991
- Sagaut, P., *Large Eddy Simulation for Incompressible Flows*, Springer, Berlin, Heidelberg, New York, 2001.
- Schmidt, H., and U. Schumann, *Coherent structure of the convective boundary layer deduced from large-eddy simulation*, J. Fluid Mech., 200, 511-562, 1989.
- Schott, F., M. Visbeck, and J. Fischer, *Observations of vertical currents and convection in the central Greenland Sea during the winter of 1988/1989*, J. Geophys. Res., 98, 14402-14421, 1993.
- Schumann, U., *Subgrid-scale model for finite difference simulations of turbulent flows in plane channels and annuli*, J. Comput. Phys., 18, 376-404, 1975.
- Schumann, U., *Stochastic backscatter of turbulence energy and scalar variance by random subgrid-scale fluxes*, Proc. Roy. Society London, A 451, 293-318, 1995.
- Scotti, A., C. Meneveau, and D. K. Lilly, *Generalized Smagorinsky model for anisotropic grids*, Phys. Fluids, 9, 1856-58., 1993
- Shay, T. J., and M. C. Gregg, *Convectively driven turbulent mixing in the upper ocean*, J. Phys. Ocean., 16, 1777-1798, 1986.
- Shih, T. S., and A. Shabbir, *Advances in modeling the pressure corelation terms in the second moment equations*, In: T. B. Gatski, S. Sarkar, and C. G. Speziale (eds.), *Studies in Turbulence*, Springer, Berlin, Heidelberg, New York, 1992.
- Skyllingstad, E.D., and D. W. Denbo, *An ocean large-eddy simulation of Langmuir circulation and convection in the surface mixed layer*, J. Geophys. Res., 100, 8501-8522, 1995.
- Smagorinsky, J., *General circulation experiments with the primitive equations. Part I: The basic experiment*, Mon. Wea. Review, 91, 99-164, 1963.
- Smith, S. D., *Coefficients for sea surface wind stress, heat flux and wind profiles as a function of wind speed and temperature*, J. Geophys. Res., 93 (C12), 15,467-15,472, 1988.

- Smith, D. C., R. D. Muench, and C. H. Pease, *Polynyas and Leads: An Overview of Physical Processes and Environment*, J. Geophys. Res., 95, C6, 9461-9479, 1990.
- Speziale, C. G., *Reynolds-stress closures*, Annu. Rev. Fluid Mech., 23, 107-157, 1991.
- Speziale, C. G., S. Sarkar, and T. B. Gatski, *Modelling the pressure-strain correlation of turbulence: an invariant dynamical systems approach*, J. Fluid Mech., 227, 245-272, 1991.
- Stull, R. B., *The energetics of entrainment across a density interface*, J. Atmos. Sci., 33, 1260-1267, 1976.
- Stull, R. B., *An introduction to boundary layer Meteorology*, Kluwer Academic Publishers, Dordrecht, Boston, London, 1988.
- Sweby, P. K., *High resolution schemes using flux limiters for hyperbolic conservation laws*, SIAM J. Num. Anal., 21, 995-1011, 1984.
- Sullivan, P. P., J. McWilliams, and C.-H. Moeng, *A subgrid-scale model for large-eddy simulation of planetary boundary-layer flows*, Boundary-Layer Meteorology, 71, 247-276, 1994.
- Sullivan, P. P., C.-H. Moeng, B. Stevens, D. H. Lenschow, and S. D. Mayor, *Structure of the entrainment zone capping the convective atmospheric boundary layer*, J. Atmos. Sci., 55, 3042-3064, 1998.
- Svensson, U., *The structure of the turbulent Ekman layer*, Tellus, 31, 340-350, 1979.
- Taulbee, D. B., *An improved algebraic Reynolds stress model and corresponding non-linear model*, Phys. Fluids, 4, 2555-2567, 1992.
- Tennekes, H., *A model of the dynamics of the inversion above a convective boundary layer*, J. Atmos. Sci., 30, 558-567, 1973.
- Tennekes, H., and J. L. Lumley, *A First Course in Turbulence*, MIT Press, Cambridge, 1982.
- Tritton, D. J., *Physical Fluid Dynamics*, Oxford University Press, Oxford, New York, 1988.
- UNESCO, *The Practical Salinity Scale 1978 and the International equation of State of Seawater 1980*, UNESCO Technical Papers in Marine Sciences, No. 36, UNESCO, Paris, 1981.

- van Atta, C. W., *Local isotropy of the smallest scales of turbulent scalar and velocity fields*, Proc. Roy. Soc. London, A 434, 139-146, 1991.
- van Leer, B., *Towards the ultimative conservative difference scheme II. Monotonicity and conservation combined in a second order scheme*, J. Comput. Phys., 14, 361-370, 1974.
- Walter, B. A., and J. E. Overland, *Observations of zonal rolls in a Near Neutral Atmosphere*, Mon. Wea. Rev., 112, 200-208, 1984.
- Webster, C. A. G., *An experimental study of turbulence in a density stratified shear flow*, J. Fluid Mech., 19, 221-245, 1964.
- Wehde, H., and J. O. Backhaus, *The fate of Lagrangian tracers in oceanic convective conditions: on the influence of oceanic convection in primary production*, Nonlinear Analysis: Real World Applications I, 3-21, 2000.
- Wehde, H., J. O. Backhaus, and E. Nost Hegseth, *The influence of oceanic convection in primary production*, Ecological Modelling, Vol. 138/1-3, 115-126, 2001.
- Weinstock, J., *On the Theory of Turbulence in the buoyancy Subrange of Stable Stratified Flows*, J. Atmos. Sci., 35, 634-649, 1978.
- Wilczak, J. M., and J. E. Tillman, *The three-dimensional structure of convection in the atmospheric surface layer*, J. Atmos. Sci., 37, 2424-2443, 1980.
- Wyngaard, J. C., O. R. Coté, and Y. Izumi, *Local Free Convection, Similarity, and the Budgets of Shear Stress and Heat Flux*, J. Atmos. Sci., 28, 1171-1182, 1971.
- Wyngaard, J. C., and O. R. Coté, *The evolution of a convective planetary boundary layer- A higher-order-closure model study*, Bound. Lay. Meteor., 7, 289-308, 1974.
- Wyngaard, J. C., and R. A. Brost, *Top-down and bottom-up diffusion of a scalar in the convective boundary layer*, J. Atmos. Sci., 41, 102-112, 1984.
- Yamada, T., *On the similarity functions A, B and C of the planetary boundary layer*, J. Atmos. Sci., 33, 781-793, 1976.
- Zalesak, S. T., *Fully multidimensional flux-corrected transport algorithms for fluids*, J. Comput. Phys., 31, 335-362, 1979.
- Zeman, O., and H. Tennekes, *A Self-Contained Model for the Pressure Terms in the Turbulent Stress Equations of the Neutral Atmospheric Boundary Layer*, J. Atmos. Sci., 32, 1808-1813, 1975.

- Zilitinkevich, S. S., *On the turbulence and diffusion under free convection*, Izv. Akad. Nauk SSR, Ser. Fiz. Atmosf. i. Okeana, 7, 822-828 (in English transl.), 1971
- Zilitinkevich, S. S., *Shear convection*, Bound. Lay. Meteor., 3, 416-423, 1973.
- Zilitinkevich, S. S., *Turbulent Entrainment in convective shear flows*, Sonderforschungsbereich 210 *Strömungsmechanische Bemessungsgrundlagen für Bauwerke*, Universität Karlsruhe, SFB 210/T/68, 1990.
- Zilitinkevich, S. S., *Turbulent penetrative convection*, Avebury Technical, Aldershot, Brookfield, Hong Kong, Singapore, Sydney, 1991.
- Zilitinkevich, S. S., *A generalized scaling for convective shear flows*, Bound. Lay. Meteor., 70, 51-78, 1994.

Acknowledgements

This work was guided by Prof. Dr. Jan O. Backhaus, who provided not only valuable advice but also patience and encouragement, which is gratefully appreciated.

Thanks also to my colleagues from the Institut für Meereskunde in Hamburg. Discussions with Kai Logemann, Kerstin Hatten and Dr. Henning Wehde were very useful. I am especially grateful to Prof. Dr. Hans Burchard for countless discussions on marine turbulence, his interest in my work and useful hints. Some valuable hints related to LES and dimensional analysis were provided by Dr. Dmitrii Mironov which is also gratefully appreciated.

I am indepted to Dr. Andreas Meister, Dr. Henning Wehde, Silke Günzel and to Kerstin Ronneberger for critical reading and helpful comments on draft versions.

This work was supported by the *Deutsche Forschungsgemeinschaft* through Graduiertenkolleg 431 *Erhaltungsprinzipien in der Modellierung und Simulation mariner, atmosphärischer und technischer Systeme* at the University of Hamburg.